PROCESS MODELING AND TECHNO-ECONOMIC ANALYSIS OF ZEOLITE MEMBRANE SEPARATION PROCESSES

A DISSERTATION
SUBMITTED TO THE FACULTY OF THE GRADUATE SCHOOL
OF THE UNIVERSITY OF MINNESOTA
BY

Nitish Mittal

IN PARTIAL FULFILLMENT OF THE REQUIREMENTS
FOR THE DEGREE OF
DOCTOR OF PHILOSOPHY

Advised by:
Michael Tsapatsis
Prodromos Daoutidis

April, 2018

Acknowledgements

I would like to thank my advisors Professor Michael Tsapatsis and Professor Prodromos Daoutidis for giving me the opportunity to work on a wide variety of projects and applications. They have always been approachable and patient especially during tough times. Their guidance and support throughout my graduate studies has been instrumental in preparation of this thesis and to my general academic progress.

I would also like to thank Professor J. Ilja Siepmann with whose group I have extensively collaborated to obtain transport and thermodynamic properties using molecular simulations.

I would like to acknowledge both the group members who have been generous with their time and always willingly participated in helpful discussions over the years.

A sincere thanks to all my friends who have made my stay at Minnesota worthwhile and provided me with wonderful and lifelong memories of the amazing time we spent together.

Most importantly, I would like to thank my family who have always believed in me and supported me in every decision, and I would like to dedicate my work to them.

To my family

Abstract

Zeolite membrane separation is considered to be a promising alternative to the traditional energy-intensive industrial separation techniques such as distillation. Currently, zeolite membranes are implemented in industry only for solvent dehydration applications. However, good separation performance is obtained at laboratory scale for various applications such as bioethanol enrichment, hydrogen recovery, natural gas purification, butane isomer separation, xylene isomer separation, etc. This progress should pave the way for the industrial implementation for other applications. Although significant progress has been made in preparation, characterization and commercialization of zeolite membranes, rigorous models, which can predict the membrane performance in industrial settings, are not available in the literature. Mathematical and process modeling plays an important role in the implementation and evaluation of any new technology or application. Thus, specific objectives of this thesis are to (i) design and develop a detailed mathematical model of a zeolite membrane separation process for accurate performance prediction under a wide variety of operating conditions, and (ii) develop and optimize a conceptual process design approach and perform a techno-economic evaluation for several significant application specific flowsheets.

In this thesis, complex challenges both at the chemical engineering fundamentals and the process scale have been addressed. A detailed mathematical model of a zeolite membrane separation based on adsorption-diffusion phenomenon is formulated using Maxwell-Stefan equations. In addition to the adsorption and diffusion based transport through zeolite layer, factors such as mass transfer through the porous support, the use of a sweep gas, concentration polarization phenomenon and presence of defects are also discussed. The adsorption-diffusion model (including external resistances) is then integrated with the process-scale governing equations to assess the industrial potential of zeolite membranes. Further, conceptual process designs have been modeled and techno-economic evaluation has been performed to evaluate the scope of zeolite membrane separation for several applications in chemical and bio-based refineries, including butane isomer separation, bioethanol enrichment and propylene-propane separation. Both the stand-alone membrane systems and hybrid membrane-distillation systems have been considered. A hybrid membrane-distillation process is found to be energy efficient and economically attractive over stand-alone membrane systems. Finally, a net present value of the system is analyzed to generate a set of performance targets in term of the permeance and the membrane cost.

Contents

List of tables

List of figures

Chapter 1: Introduction

The ability to separate a chemical mixture into its individual components is essential in the chemical industry. Presently, most separations are accomplished using distillation. Although distillation is a well-established technology due to its high flexibility and low operational risk, it is energy-intensive with a thermodynamic efficiency of ~10% [1]. A U.S. Department of Energy report states that > 40,000 distillation units are in operation in the U.S., and consume much more energy than all other separation processes combined [1]. Alternatively, membrane separation is an energy efficient process and has a great potential to either replace or supplement the existing distillation columns, and thus reduce energy use and associated pollutant emissions.

Currently, polymeric membranes are dominant in the membrane industry. However, zeolites (a class of inorganic crystalline materials) offer significant advantages over polymers because of their excellent mechanical, thermal and chemical stability. In addition, a uniform pore structure with a pore size ranging from 3 Å to 10 Å makes zeolites even more effective for a wide variety of separations. However, despite significant investments in research and development on zeolite membranes, only limited industrial implementation has occurred [2]. A U.S. Department of Energy report (2005) suggested the development of (i) defect-free thin films and (ii) predictive membrane performance models as the key areas of future research [3]. In recent years, although significant progress has been made in preparation and characterization of zeolite membranes, rigorous models which can predict the membrane performance in industrial settings are still lacking.

The permeation through a zeolite membrane is a complex process and is usually represented in terms of permeance and selectivity [4,5]. Permeance (ease of mobility) is the rate of flow per unit area per unit driving force while selectivity (ability to separate) is

the ratio of permeance of the two species being separated. A zeolite membrane consists of a thin zeolite film over a porous support. Molecular transport should be governed by the selective zeolite film, where permeance and selectivity depend on the adsorption (adhesion of a molecule on the membrane surface) and diffusion (movement of a molecule from a region of high concentration to low concentration) properties of the mixture components. However, other resistances to transport (i.e. from the porous support and/or the boundary layer) can also affect performance. Though the support layer has larger pores, it is relatively thicker and may provide a comparable resistance. Furthermore, formation of a boundary layer in the fluid adjacent to the membrane surface also deteriorates the performance. The presence of defects formed during synthesis also affects the permeance and selectivity.

Zeolite membranes have shown good separation at laboratory scale for various applications such as bioethanol enrichment, hydrogen recovery, natural gas purification, butane isomer separation, xylene isomer separation, etc. Currently, zeolite membranes are implemented in industry only for solvent dehydration applications but the recent progress should pave the way for the industrial implementation for other applications [2]. Mathematical and process modeling plays an important role in the implementation and evaluation of any new technology or application. However, no rigorous models exists for zeolite membranes, which set the aim of this PhD research, i.e., to develop such enabling tools that can assess the potential of zeolite membranes in industry. The specific objectives are to (i) design and develop a detailed mathematical model of a zeolite membrane separation process for accurate performance prediction under wide range of operating conditions, and (ii) develop and optimize a conceptual process design approach and perform a techno-economic evaluation for several significant application specific flowsheets.

Chapter 2 focuses on developing a framework for membrane modeling. First, a fundamental understanding of transport phenomena underlying the zeolite membrane operation is developed, and models that can quantitatively describe these phenomena are reviewed. Permeation through zeolite film is described through adsorption-diffusion phenomenon; both single-component and mixtures are considered. Further, several non-idealities and their effect on modeling is also considered. In addition to the adsorption and diffusion based transport through zeolite layer, factors such as mass transfer through the porous support, the use of a sweep gas, concentration polarization phenomenon and presence of defects are also discussed. The adsorption-diffusion model (including external resistances) is then integrated with the process-scale governing equations to assess the industrial potential of zeolite membranes; both the stand alone and hybrid membrane-distillation processes are considered. This chapter is adapted from N. Rangnekar, N. Mittal, et al., Chem. Soc. Rev. 44 (2015) 7128–7154.

Chapter 3 focuses on the application of the model for butane isomer separation. The application was selected because the availability of both (i) molecular level transport properties and (ii) industrial scale distillation data allows for a rigorous mathematical description of membrane performance and its detailed comparison with the current industrial practice. Moreover, butanes offer a great opportunity for implementation of novel separation technologies since they are used as a fuel and as a feedstock to make plastics and their global market is growing at an annual rate of 2.46% [6]. A key issue addressed in this chapter is that the adsorption and diffusion parameters shall be carefully reviewed and selected. While adsorption properties determined using different measurement techniques are in good agreement, the diffusivities can vary up to three orders of magnitude based on how these coefficients are determined [7]. The detailed analysis on adsorption and diffusion studies combined with external resistances not only improves the

understanding of discrepancies between the results obtained by experiments and modeling, but also determines the scope of improvement in the current state-of-the-art membranes. Finally, a techno-economic analysis using a process-scale model is also performed to generate a set of performance targets in term of the permeance and the membrane cost. This chapter is adapted from Mittal et al., J. Memb. Sci. 520 (2016) 434–449.

Chapter 4 focuses on the application for bioethanol enrichment, and discusses the role of hydrophilic and hydrophobic zeolite membranes. This extends the scope of modeling to bio-refineries related application. An important issue addressed, here, is the presence of non-idealities and defects which leads to failure of ideal models for determining the mixture adsorption and diffusion properties. Thus, atomistic-level simulations are carried out to obtain a consistent set of mixture adsorption and diffusion properties incorporating the effects of hydrogen bonding. The results obtained from membrane modeling are further incorporated in design studies illustrating how the atomistic-level properties can be used in process-level simulation. Another key issue addressed here is that membrane separation is not necessarily energy-efficient. For applications including pervaporation (as for most of the bio-refinery related applications) where the feed is liquid while the permeate is vaporized, the energy for this vaporization should be supplied and can make the process energy-intensive. Both the above-mentioned issues are incorporated in modeling ethanol-water separation. Further, several conceptual designs are considered and a techno-economic analysis is performed to determine the optimum combination of distillation and membrane separation. This chapter is adapted from Mittal et al., J. Memb. Sci. 540 (2017) 464–476.

Chapter 5 focuses on comparing the membrane performance with heat-integrated distillation, and is illustrated for propylene-propane separation. While conventional distillation is usually-intensive, heat-integration within the column can significantly reduce

the energy consumption. If these energy savings can be realized in practice, there is little room left for membrane technology [8]. However, such designs are not routinely employed due to operational and control challenges [9]. Instead heat-integration can be implemented through other parts of the plant generating extra amount of low-grade heat, such as, quench water. Therefore, a range of possible scenaria for the level of heat integration is examined with thermally non-integrated and fully-integrated distillation columns as the upper and lower boundaries of energy requirement. The debottlenecking of existing distillation columns, i.e., implementing membranes in hybrid configuration with existing distillation column to increase the overall capacity, is also considered. This chapter is adapted from X. Ma, P. Kumar, N. Mittal, et al. which is currently submitted for publication.

Chapter 2: Zeolite membrane modeling review and advancements

2.1 Introduction

Zeolite membranes offer an attractive alternative to conventional energy intensive separation processes [10–14]. Their chemical and thermal stability, and well-defined pore structure with pore sizes ranging from 0.3-1.0 nm allow for high-selectivity separations at a wide range of operating conditions. Although zeolite membranes have shown remarkable progress at laboratory scale [2,15–22] and promising results have been obtained for various industrially relevant applications such as alcohol dehydration [15,23–26], butane isomer separation [20,27–31], xylene isomer separation [28–31] and natural gas purification [32–35] , only hydrophilic membranes used in the dehydration of industrial solvents have been commercialized to date [2,13]. To explore the commercialization potential of zeolite membranes, rigorous models and process designs which can predict the currently achieved performance and set targets for membrane cost and performance improvements are essential. These rather complicated models should be further validated by comparison with experiments and included in the process models that describe permeation through membranes at a wide range of operating conditions as encountered by membranes in industrial use.

A schematic of the membrane structure in a typical laboratory setting is shown in **Figure 2.1a**. The membrane structure consists of a zeolite layer on a porous support. The feed stream is passed across the retentate side facing the zeolite film, and the permeating species are collected by flowing a sweep gas across the permeate side. Compartments on both sides of the membrane i.e., the retentate side and the permeate side are usually well-

mixed in a lab experiment. In the following sections, the transport mechanism and model development for permeation through zeolite membrane is described.

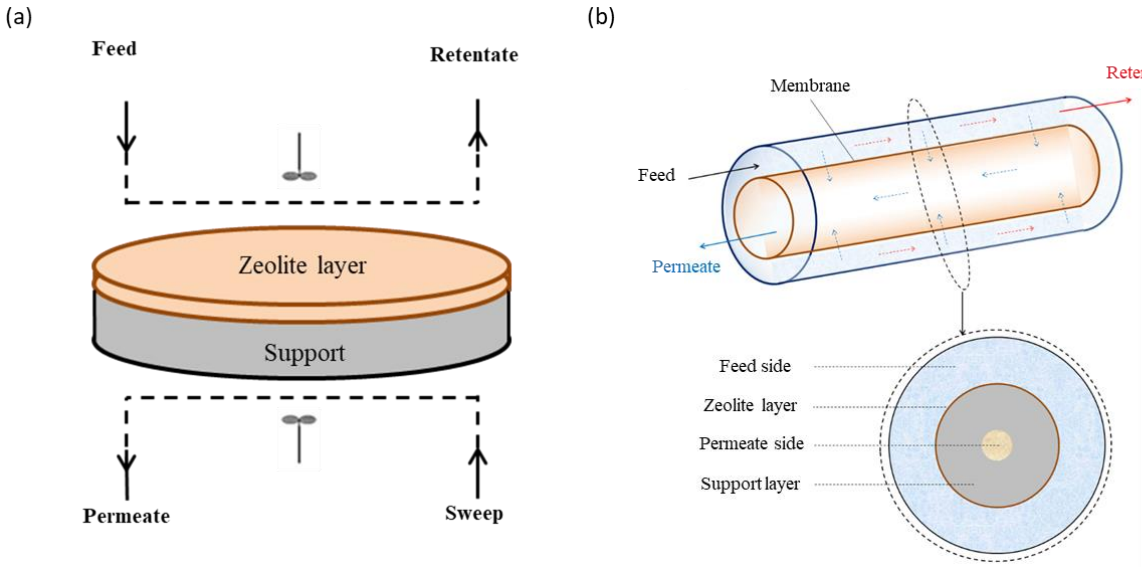

Figure 2.1: Schematic of **(a)** a zeolite membrane in a typical laboratory setting. **(b)** a tubular zeolite membrane at a process scale.

2.2 Transport model for zeolite layer

To determine the permeation through zeolite layer, a fundamental understanding of transport phenomena underlying the membrane operation, and models that can quantitatively describe these phenomena, are necessary. When the size of the molecules permeating through the zeolite pores is comparable to the pore diameter, which is often the case for selective separation, molecules permeate at a regime commonly known as intracrystalline or configurational diffusion. Permeation in this regime is a complex process that depends on both the adsorption and diffusion properties of the permeating species in the mixture [16,23,36–41]. The adsorption and diffusion properties at this microscopic level are obtained using experimental and simulation techniques, fitted to adsorption and diffusion models, and then finally used in continuum models to determine the flux through the zeolite membranes. While most modeling studies employ simple ideal theories based

on single-component adsorption and diffusion properties [42–47], the intermolecular interactions can be far from ideal and may lead to the failure of these theories [48–54].

Krishna and co-workers [4,5,55–58] have extended the Maxwell–Stefan approach, which provides a fundamental description of multi-component diffusion, to formulate the generalized Maxwell–Stefan model for permeation through a zeolite membrane:

$$-\rho\frac{\theta_i}{RT}\nabla\mu_i = -\rho\sum_{j=1}^{n}\Gamma_{ij}\nabla\theta_j = \sum_{j=1,j\neq i}^{n}\frac{q_j N_i - q_i N_j}{q_i^{sat} q_j^{sat} Đ_{ij}} + \frac{N_i}{q_i^{sat} Đ_i} \qquad i = 1,2....,n \qquad (2.1)$$

where ρ is the zeolite density, θ is the fractional loading, R is the universal gas constant, T is the absolute temperature, μ is the chemical potential, Γ is the thermodynamic factor, q is the loading, q^{sat} is the saturation loading, N is the flux, $Đ_i$ is the Maxwell–Stefan diffusivity and $Đ_{ij}$'s are the exchange coefficients. The equation can be regarded as a force balance with the left-hand-side term representing the driving force due to a chemical potential gradient and the right-hand-side terms representing the friction forces due to molecule-molecule interactions and molecule-zeolite pore wall interactions. The influence of adsorption is taken into account through the fractional loading at the surface and the thermodynamic factors while the mobility is determined by the two kinds of diffusion coefficients – the corrected diffusivity which is also known as Maxwell–Stefan diffusivity and the exchange coefficients

2.2.1 Adsorption modeling

The single component adsorption isotherm is most commonly modeled using the dual site Langmuir model [59,60]:

$$q_i = \frac{q_{i,a}^{sat} k_{i,a} P}{1 + k_{i,a} P} + \frac{q_{i,b}^{sat} k_{i,b} P}{1 + k_{i,b} P} \qquad (2.2)$$

where q is the loading, q^{sat} is the saturation loading, *k's* are the Langmuir constants, P is the pressure and 'a' and 'b' represent the two sites, has been used to model the adsorption

isotherm. Other forms of the isotherm e.g. Toth, Langmuir–Sip, Langmuir–Freundlich. have also been used [50,61]. The single component adsorption are well studied as they can be measured with good accuracy and thus can be validated experimentally. However multi-component adsorption experiments are challenging, and is discussed next.

The multi-component adsorption is usually determined by models based on the information gained by single-component isotherm. However, these results are difficult to validate experimentally, and thus are usually validated by molecular simulations. Various models have been suggested for multi-component adsorption. The mixture isotherm can be predicted, from the single component isotherm, by implementing appropriate mixture rules based on dual-site Langmuir isotherm [62]

$$q_1 = q_{1A,sat}\frac{k_{1A}P_1}{1 + k_{1A}P_1 + k_{2A}P_2} + q_{1B,sat}\frac{k_{1B}P_1}{1 + k_{1B}P_1 + k_{2B}P_2} \tag{2.3}$$

where q is the loading, q^{sat} is the saturation loading, *k's* are the Langmuir constants, P is the pressure, and 'A' and 'B' represent the two sites and '1' and '2' represents the two components, has been used to model the adsorption isotherm. However, the use of mixture rules is only moderately successful and a thermodynamically consistent model, known as Ideal Adsorption Solution (IAS) theory [63]:

$$\begin{aligned} Py_i &= P_i^{\,o}(\pi)x_i \\ {\pi A}/{RT} &= \int_0^{P_1^0} q_i(p)\, d\, lnp \\ \frac{1}{q_t} &= \sum_i \frac{x_i}{q_i(P_i^{\,o})} \end{aligned} \tag{2.4}$$

is widely used for predicting mixture isotherms from single component data. This theory is analogous to Raoult's Law vapor-liquid equilibrium model with added equations accounting for the adsorbed phase. **Figure 2.2a** shows that the prediction of IAS theory for

a mixture of alkanes is in excellent agreement with simulation results [64]. One of the drawbacks of IAS theory is the assumption that the system behaves like an ideal solution and therefore, it is inadequate to describe multicomponent adsorption for non-ideal mixtures. The presence of non-idealities, such as hydrogen bonding effects, in the mixture, thus, leads to failure of IAS theory as shown in **Figure 2.2b** for water–ethanol mixture in MFI zeolite [52].

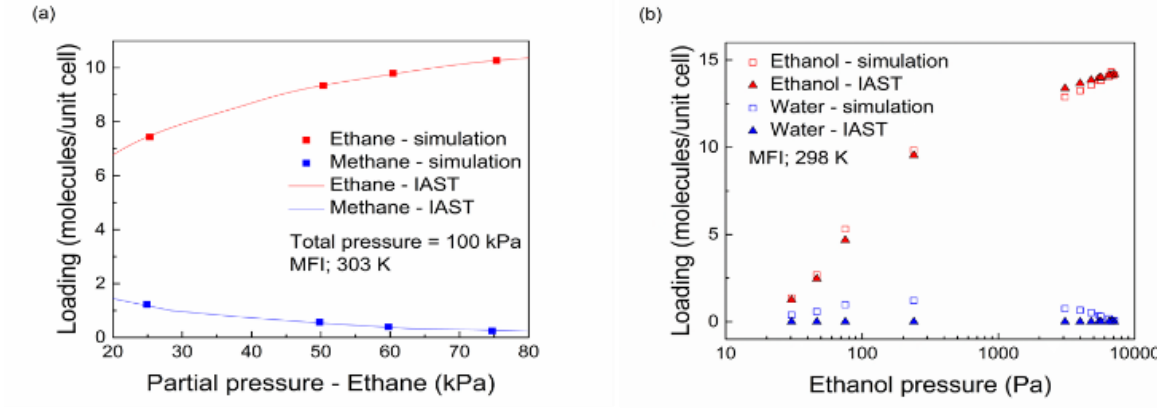

Figure 2.2: Molecular simulation results and IAST prediction for multicomponent adsorption on MFI crystals: **(a)** success of IAST for methane-ethane mixture [2], **(b)** failure of IAST for water-ethanol mixture [2].

The existence of non-idealities in the mixture is either due to energetic or surface heterogeneity or due to a non-ideal mixture itself. Energetic heterogeneity arises due to varying heat of adsorption for different sites while surface heterogeneity is caused due to different surface area (sites) available for adsorption of different species. Various extensions of IAS theory have been described to account for these non-idealities. Heterogeneous IAS theory has been used to account for energetic heterogeneity [65] and surface area corrected IAS (SAC-IAS) theory has been used to account for surface heterogeneity [53]. However, these models can only be used for limited operating conditions, and various versions of these models are used depending on the mixture in

consideration. Thus a more general model, known as real adsorption solution (RAS) theory:

$$\begin{aligned} Py_{\mathrm{i}} &= P_{\mathrm{i}}^{\mathrm{o}}(\pi)\gamma_{\mathrm{i}}x_{\mathrm{i}} \\ \frac{\pi A}{RT} &= \int_0^{P_{\mathrm{i}}^{o}} q_{\mathrm{i}}(p)d\ln p \\ \frac{1}{q_{\mathrm{t}}} &= \sum_{\mathrm{i}} \frac{x_{\mathrm{i}}}{q_{\mathrm{i}}\left(P_{\mathrm{i}}^{\mathrm{o}}\right)} \end{aligned} \tag{2.5}$$

has been proposed for mixture adsorption isotherm [63]. The RAS theory is a more general form of IAS theory, and makes use of the activity coefficients to account for non-ideal deviations. An analogy can be drawn to the vapor-liquid equilibrium curves where the activity coefficients accounts for the non-idealites and are functions of temperature and composition. The activity coefficients, in RAST, are functions of temperature, composition and spreading pressure. The addition of an extra intensive variable, spreading pressure, is due to the adsorbent being present in the system as an additional component. Although Talu and Zwiebel [66] have developed a thermodynamically consistent model to calculate the activity coefficients, the spreading pressure dependency of the activity coefficients makes such models extremely complicated. Thus the activity coefficient models used to describe vapor–liquid equilibrium such as UNIQUAC, NRTL and Wilson, are often applied with good accuracy to the mixture adsorption as well [67–71]. The parameters are usually obtained by fitting the mixture simulation data.

2.2.2 Diffusion modeling

Diffusion is described in terms of corrected diffusivity and exchange coefficients. The corrected diffusion coefficient accounts for sorbate–sorbent interactions and exhibits loading dependency. Various models have been used to describe this loading dependency.

The most commonly used are the weak confinement scenario and the strong confinement scenario[43]:

$$Đ_i = Đ_i(1-\theta) \ \textit{(strong confinement)}$$
$$Đ_i = Đ_i \ \textit{(weak confinement)} \tag{2.6}$$

where $Đ_i$ is the Maxwell–Stefan diffusivity, θ is the fractional loading and 'i' refers to the component, which are based upon the vacancy factor and the repulsion factor [43]. The vacancy factor accounts for the probability of the adjacent adsorbing site being vacant and decreases with loading while the repulsion factor accounts for inter-molecular repulsion and increases with loading. However, these are the ideal scenarios and the actual dependency varies between the two scenarios. Another model, based upon the quasi-chemical approach of Reed and Ehrlich, also accounts for the reduction of the energy barrier for diffusion with increased loading and is also widely used [72,73]. Since the corrected diffusivity is interpreted in terms of hopping from one adsorbed site to another, the loading dependence is strongly influenced by adsorption thermodynamics. It has been shown that the corrected diffusivity is inversely proportional to the thermodynamic factor which signifies the change in fractional loading with respect to a change in fugacity and can be calculated from the adsorption isotherm [74–76]. The corrected diffusion coefficient of a species in a mixture is usually taken equal to that of the single component at the same total loading.

The exchange coefficients account for sorbate–sorbate interactions and capture the effect that a faster moving molecule is slowed down in the presence of slower moving species and vice versa [77]. The incorporation of the exchange coefficients into the Maxwell–Stefan equations leads to computational difficulties and thus these coefficients are often neglected; this scenario is known as the facile exchange [5,43]. However, these

effects have been shown to be significant and various models have been proposed for their incorporation [51]. The two most commonly used models are, (i) Vignes correlation:

$$Đ_{ij} = Đ_i^{\frac{q_i}{q_i+q_j}} Đ_j^{\frac{q_j}{q_i+q_j}} \tag{2.7}$$

where $Đ_i$ is the Maxwell–Stefan diffusivity, q is the loading and 'i' refers to the component, for species with similar loading and (ii) the correlation developed by Sholl [43]:

$$\theta_{j,sat} Đ_{ij} = \left(\theta_{j,sat} Đ_i\right)^{\frac{q_i}{q_i+q_j}} \left(\theta_{i,sat} Đ_j\right)^{\frac{q_j}{q_i+q_j}} \tag{2.8}$$

where $Đ_i$ is the Maxwell–Stefan diffusivity, θ is the fractional loading, q is the loading and 'i' refers to the component for species with variable loading. Since the exchange coefficients capture the sorbate–sorbate interactions, it has also been found that there is a dependence of the exchange coefficients on the corresponding fluid phase diffusivity; the proportionality factor depends upon the degree of confinement and the correlation effect increases with the degree of confinement [78]. The factor is often linearly dependent upon the degree of confinement, however, other expressions such as Darken-type interpolation and Vignes-type interpolation have also been proposed [78].

Although several have models have been developed and used to describe the diffusion in zeolites, there exists scenarios where the Maxwell–Stefan model has failed to provide quantitative agreement with the experimental results. One of the examples is the xylene isomer separation using MFI zeolite membranes. The diffusion characteristics of p-xylene and o-xylene in MFI crystals have been extensively studied [79–81]. Though the permeance of p-xylene has been observed to be of the same magnitude, the Maxwell–Stefan model predicts much higher o-xylene permeance as compared to the experiments. Although this discrepancy is widely recognized, the reason behind this phenomenon is not developed. The discrepancy may be attributed to surface resistances in zeolite crystals or

to the changes in crystal structure on adsorption of p-xylene [82]. It can also be due to the fact that the diffusion coefficient used in the Maxwell–Stefan equations was measured for a flexible zeolite crystal while an intergrown supported membrane is constrained by a support and does not permit flexibility, as in the case of a free crystal.

Another phenomenon where the Maxwell–Stefan approach fails is the intersection blocking [83]. It is usually observed when branched or cyclic hydrocarbons are present in the mixture along with linear hydrocarbons in MFI. The branched hydrocarbon preferentially adsorbs at the intersection of MFI membranes which causes blocking of the pore and severely reduces the diffusivity of the normal alkane [60]. In general, the tardy species slows down the fast moving species and the effects are captured by the exchange coefficients but this effect is more severe and can cause the diffusivity of n-alkane to reduce nearly to zero. The effect of intersection blocking for methane in the presence of i-butane is shown in **Figure 2.3a**. The reduction in diffusivity is more severe as compared to the methane–n-butane mixture, which does not have intersection blocking [83]. The corrected diffusivities for water-methanol mixture are also decreased due to the presence of hydrogen bonding (**Figure 2.3b**). Thus, using the single component data to predict the separation performance often leads to higher predicted flux and higher separation factors than experimentally feasible [84–86]. Further, the loading dependency shall be studied and modeled for specific mixture in consideration.

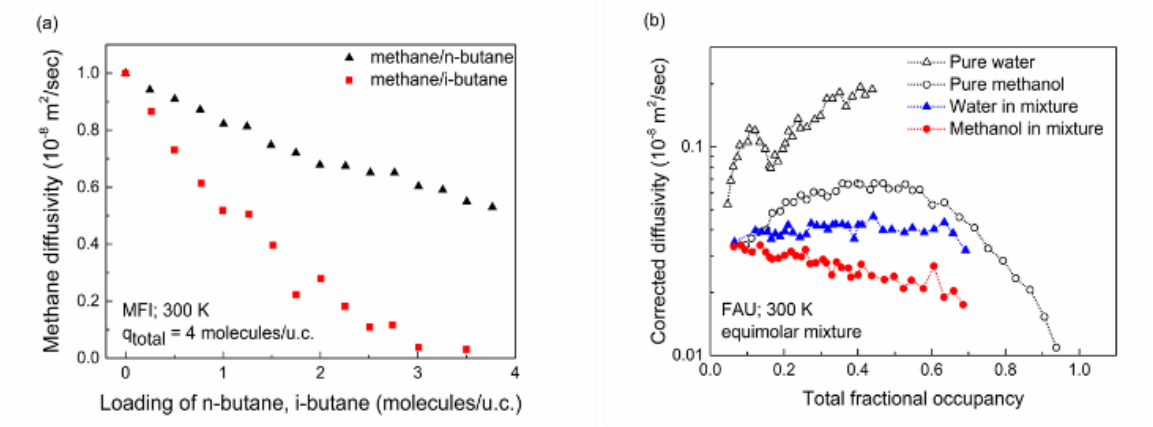

Figure 2.3: (a) Effect of intersection blocking: diffusivity of methane (linear alkane) decreases more steeply in presence of i-butane (branched alkane) as compared to n-butane (linear alkane) in MFI [2], **(b)** Corrected diffusivity of water-methanol mixture in FAU at 300 K obtained through MD simulations [2].

2.3 Transport model for external resistances

In addition to the adsorption and diffusion based transport through zeolite layer, factors such as mass transfer through the porous support, the use of a sweep gas, concentration polarization phenomenon and presence of defects can also play a significant role [2]. The support is particularly important for membranes with thin zeolite films as the resistance of the support layer can dominate the transport through the membrane [24,44,87,88]. The use of sweep gas increases the driving force for permeation by carrying away permeating species. However, there is also an adverse effect on permeation due to the counter flux of sweep gas [89]. The concentration polarization can occur because different species in a feed mixture permeate at different rates through the membrane, which may result in accumulation of the non-preferentially permeating species and depletion of the selectively permeating species in a thin layer (boundary layer) adjacent to the membrane surface. This phenomenon changes the concentration gradient through the membrane in an unfavorable manner and deteriorates the membrane separation performance [23,90–92]. The presence of defects further introduces more complexities and should be incorporated based on the specific system in consideration. Thus, mathematical models which can describe the

support layer, permeation of sweep gas, concentration polarization and defects should also be incorporated in the design of zeolite membrane systems.

2.3.1 Model for the support

The zeolite membranes are grown on a porous support. The support layer is usually neglected in most of the modeling studies. However, it has been shown that the support can play a significant role especially in thin or high-flux membranes [44,88]. The significant mass transfer resistance in the support adversely affects the separation performance of MFI and FAU membranes for ethanol/water separation [35]. The effect is more prominent for strongly adsorbing species as shown for H2/CO2 separation where the pressure drop for CO2 over the support was quite large and influenced the separation performance [93]. Thus, flux and selectivity for high flux membranes can be increased by preparing less resistive supports. It is essential to incorporate transport resistance effects due to the support layer in permeation models. The models proposed in the literature are well established and incorporate flux through the Knudsen and molecular diffusion and viscous flow [59,94,95]. The Knudsen diffusivity (D_i^k), which accounts for molecule-wall interactions, has been derived from the kinetic theory of gases and is given by:

$$D_i^{\,k} = \frac{\varepsilon}{\tau}\frac{d_{pore}}{3}\left(\frac{8RT}{\pi MW_i}\right)^{1/2} \tag{2.9}$$

where ε is the support porosity, τ is the support tortuosity, d_{pore} is the support pore size and MW is the molecular weight of the permeating species. The molecular diffusivity (D_{ij}), which accounts for molecule-molecule interactions, is estimated using the Fuller-Schettler-Giddings equation [96]:

$$D_{ij} = \frac{\varepsilon}{\tau}\frac{T^{1.75}\left(1/MW_i + 1/MW_j\right)^{1/2}}{P\left(\left(\sum_i v_a\right)^{1/3} + \left(\sum_j v_a\right)^{1/3}\right)^2} \tag{2.10}$$

where P is the total pressure and v_a is the atomic volume. The partial pressure gradient due to these interactions is additive and is given by:

$$-\frac{1}{RT}\frac{dp_i}{dz} = \frac{N_i}{D_i^k} + \sum_{j=1, j\neq i}^{n} \frac{x_j N_i - x_i N_j}{D_{ij}} \qquad i = 1,2....,n \qquad (2.11)$$

In addition to Knudsen and molecular diffusion, a finite total pressure gradient across the support also gives rise to viscous flux:

$$N_{v,i} = -\frac{\varepsilon}{\tau}\frac{p_i}{RT}\frac{\beta}{\mu}\frac{dP}{dz} \qquad \beta = d_{pore}^{\,2}/32 \qquad i = 1,2....,n \qquad (2.12)$$

where μ is the mixture viscosity. The total flux is obtained by the summation of the viscous flux and the flux obtained in Eq. 4.

To solve the coupled partial differential equations for the zeolite and the support layer, boundary conditions are required at the retentate side, the permeate side, and also at the zeolite-support interface. In the absence of any external resistance (the effects of external resistance are discussed in the next section), the loading at the feed side is calculated assuming equilibrium between feed partial pressure and loading at the zeolite layer. At the zeolite-support interface, the boundary conditions are obtained by assuming that no accumulation occurs at the interface i.e. the flux of a component leaving the zeolite layer is equal to the flux entering the support layer. Equilibrium is also assumed between the loading at the zeolite layer and the partial pressure in the support layer at the interface. At the permeate side, the total pressure is usually fixed and known, and the mole fractions are calculated iteratively from the steady state flux of the components:

$$x_i = \frac{N_i}{\sum_i N_i} \qquad (2.13)$$

2.3.2 Model for the sweep gas

Thus, the effects of the sweep gas are twofold. While it increases the driving force by carrying away the permeating species and reducing their partial pressure on the permeate side, it also introduces a counter flux (against the permeating direction) that can have an adverse effect on permeation [89]. The use of sweep gas has been shown to improve the separation performance for methane/ethane separation. However, a higher pressure of helium on the permeate side increases its counter flux and thus decreases the permeance of ethane [89]. This counter flux affects the permeation only through the support layer because permeation of adsorbed species through the zeolite layer is not affected by non-adsorbing sweep gas. Thus, for a fixed total pressure on both sides (the retentate side and the permeate side) of the membrane, the use of sweep gas decreases the resistance through the zeolite layer by increasing the driving force, and increases the resistance through the support layer by introducing a counter-flux. Usually, the increase in driving force dominates the effect due to counter-flow, and membranes operated with a sweep gas result in higher flux and separation factor as compared to the membranes operated without sweep. However, this improvement by the introduction of a sweep is effective only if the transport in the membrane is governed by the zeolite layer.

The effects due to the use of sweep gas (helium is considered here) are also incorporated into the model. Since, helium has been shown to be non-adsorbing on MFI zeolites [73] and that its density inside the zeolite is lower than that in the gas phase, its permeation through the zeolite layer is modeled using Knudsen diffusion and viscous flow. The effective pore diameter is calculated by subtracting the diameter of the helium atom from the zeolite pore size. As steady-state permeation of adsorbed species through the zeolite layer has been shown to be unaffected by non-adsorbed species [97], it is assumed that helium permeates only through the pores unoccupied by the adsorbed species. As a

result, the helium flux through the zeolite layer is further reduced by a factor equal to fractional vacancy, given by $(1-\sum\theta_i)$. Similar to other components, permeation of sweep gas through the support is modeled considering contributions from Knudsen and molecular diffusion, and viscous flow.

2.3.3 Model for the concentration polarization

The concentration polarization (**Figure 2.4a**) increases the concentration of the non-preferentially permeating species and decreases the concentration of the selectively permeating species at the membrane surface as compared to that in the bulk feed. In most of the modeling studies, this change in concentration is neglected and the loading at the zeolite layer is assumed to be in equilibrium with the bulk feed concentration. However, concentration polarization can significantly affect the separation performance and appropriate models that can describe this behavior are essential [92,98]. It has been shown that the CO2/CH4 selectivity increased by 180% and CO2 flux by 80% when measures were taken to reduce the external boundary layer resistance for a SAPO-34 membrane [92], as shown in **Figure 2.4b**. Various models have been proposed in the literature to include its effect by introducing a mass transfer coefficient, [93,99,100] or solving the full concentration profile in the boundary layer [101,102]. In other studies, a simple resistance-in-series model is used to describe the effects of concentration polarization, however this approach applies only to the preferentially permeating component and does not account for accumulation of non-preferentially permeating species.

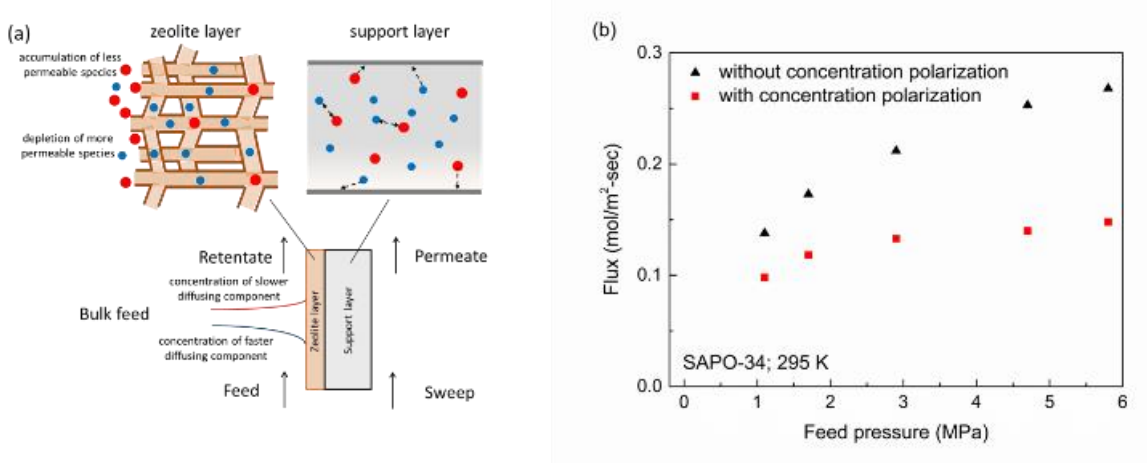

Figure 2.4: (a) Schematic of concentration polarization for permeation through a zeolite membrane, (b) Effect of concentration polarization: CO_2 flux through a SAPO-34 membrane for an equimolar mixture of CO_2/CH_4 at 295 K [2].

As solving for the velocity and concentration profile in the boundary layer is challenging, an alternative approach based on mass transport equations is used in this research [103]. In this approach, the effect of concentration polarization is determined through a parameter, known as concentration polarization index, which is defined as the ratio of mole fraction of the preferentially permeating component in the bulk feed to that at the membrane surface. This index determines the severity of the concentration polarization and is strengthened with increase in membrane enrichment and/or membrane permeability, or with decrease in the external mass transfer coefficient (in the boundary layer). An expression to calculate the concentration polarization index has been modeled using this approach [103] and given by;

$$\frac{X_s}{X_f} = \frac{1}{\alpha - (\alpha - 1)\exp(-v/k)}; \alpha = \frac{X_p}{X_s} \tag{2.14}$$

where α is the enrichment factor, v is the molar average velocity through the membrane which represents the membrane permeability, k is the external mass transfer coefficient of the more permeable component and 'f', 's' and 'p' denote the bulk feed, membrane surface and permeate, respectively. While membrane permeability and enrichment are intrinsic

properties of the membranes, the mass transfer coefficient depends on the module geometry and flow conditions, and is generally represented in terms of the Sherwood number (*Sh*) [104,105].

2.3.4 Model for the defects

Another common assumption in modeling zeolite membranes is that they are defect free. However, it has been illustrated that the defects can significantly affect the separation performance in H2/CO2 separation, [93] xylene isomer separation [106], etc. It has also been shown that defects can be induced and shrunk or expanded during adsorption and affect the permeation [82]. Permporometry, flux of molecules larger than zeolite pores and the ratio of single gas permeance, and other methods have been used to characterize defects [16,107–109]. These effects have been incorporated in some of the modeling studies by determining the permeation through the defects as a combination of Knudsen diffusion and Poiseuille flow [110,111]. A general pore network model has also been developed to account for the flux through intercrystalline pores [112]. However, the defects majorly depends upon the method of preparation of the membranes and the results can vary widely across the various experiments. Thus, the defects are usually incorporated by modifying the equations based on the system in consideration.

2.4 Process model for zeolite membranes

In the model developed above to describe the permeation at lab-scale, the retentate and the permeate compartments are assumed to be well-mixed. Such designs assume that the operating conditions do not change along the module length, resulting in fixed permeance and selectivity. However, simulation of a membrane process requires the use of models that account for changes in operating conditions along the membrane length. Thus, the detailed mathematical model for permeation through zeolite membrane is integrated with

process models to develop a process-scale model of the zeolite membrane, and described next.

2.4.1 Stand-alone membrane process

A tubular membrane design (single tube cartridge or tubes packed together in small bundle) is considered, and a schematic of a single circular tube with feed on the shell side is shown in **Figure 2.1b.** The feed can flow on either side, depending upon the position of the zeolite layer.

A plug flow model is used on the retentate and the permeate sides. The governing mass balance equations for each component are as follows:

$$-\frac{dF_{\mathrm{i}}}{dx} = \pm 2\pi r N J_{\mathrm{i}} \tag{2.15}$$

where the +ve sign refers to the retentate side while the -sign refers to the permeate side, F is the flow rate along the membrane, J is the flux through the membrane, r is the external radius of the tube and N is the total number of tubes in a bundle. As it may be difficult to maintain turbulence in sub-cm radius tubes, only laminar flow is considered, and the pressure drop on the retentate side along the membrane length is modeled using the Hagen-Poiseuille equation:

$$-\frac{dP}{dx} = \frac{8\mu\rho F}{\pi r^4 N} \tag{2.16}$$

where P refers to the total pressure [105]. The physical properties, i.e. mixture density (ρ), and viscosity (μ) are obtained using Soave-Redlich-Kwong (SRK) method [113] and SuperTRAPP method [114], respectively, and are incorporated into gPROMS [115] as a Multiflash file by using the physical properties foreign object tool. The flux through the membrane is obtained using the detailed Maxwell-Stefan model developed in the previous

sections. Accordingly, the partial pressure (p) on both the retentate and the permeate side across the membrane are obtained as follows:

$$p_{\mathrm{i}} = \frac{F_{\mathrm{i}}}{\sum_{\mathrm{j}} F_{\mathrm{j}}} P \tag{2.17}$$

This complete model, i.e., the flow model along the membrane length combined with the Maxwell-Stefan model for membrane transport is solved using gPROMS [115].

2.4.2 Hybrid membrane/distillation process

A membrane process can also be used in combination with other separation techniques, such as, distillation. The resulting hybrid membrane-distillation which exploits the advantages of both processes while minimizing the negative aspects, has shown promising potential. Various studies have shown that the hybrid membrane/distillation process is energy efficient and economically beneficial for mixtures which are otherwise impossible or difficult to separate using conventional distillation [116–119]. Such mixtures are characterized by either formation of an azeotrope (ethanol-water), or the presence of tangent pitch (water-acetic acid), or low relative volatilities (olefin-paraffin) [119]. The most common hybrid configurations containing a single distillation column and a single membrane process are shown in the **Figure 2.5** [117,119].

In the top hybrid (**Figure 2.5a)** and bottom hybrid **(Figure 2.5b)** configurations, distillation is used as a pretreatment step while the final separation is carried out by membrane separation. Such configurations are better suited for mixtures having a tangent pitch or forming an azeotrope. Moreover, the membrane should have a high separation factor to achieve the purity target. In series hybrid **(Figure 2.5c)** and parallel hybrid **(Figure 2.5d)** configurations, membrane separation is used as a pretreatment step followed by distillation to achieve the final product specifications. They are generally used for mixtures with low relative volatility and/or when membranes cannot provide high purity

separations. In a series configuration, the feed composition to the membrane unit is fixed, while in a parallel configuration it can be varied depending upon the stage of side stream extraction from the distillation column. However, it has been shown that the side draw stage in a parallel configuration is usually located near the feed stage where the distillation is least effective [148,152-155], which effectively makes it similar to the series configuration. Sometimes, a vapor feed is preferred over a liquid feed for the membrane separation to eliminate the heavy impurities which otherwise may clog the membrane pores. In those cases, if the original feed is liquid then a parallel configuration with a vapor side draw can be used. In this research, only the series configuration (**Figure 2.5c**) is considered which is also expected to be easier to retrofit and control as compared to the parallel configuration.

As the governing equations for the membrane unit and the distillation unit can be solved sequentially in a series configuration, the membrane unit is simulated in gPROMS while the distillation unit is simulated in Aspen Plus. The permeate stream from the membrane is compressed to match the column pressure.. The location of the two feed streams to the distillation column (retentate and permeate streams from the membrane unit) is optimized for a fixed membrane stage-cut (φ) to minimize the reboiler duty, where the membrane stage cut (φ) is defined as the ratio of *n*-butane flow rate in the permeate stream to that in the feed.

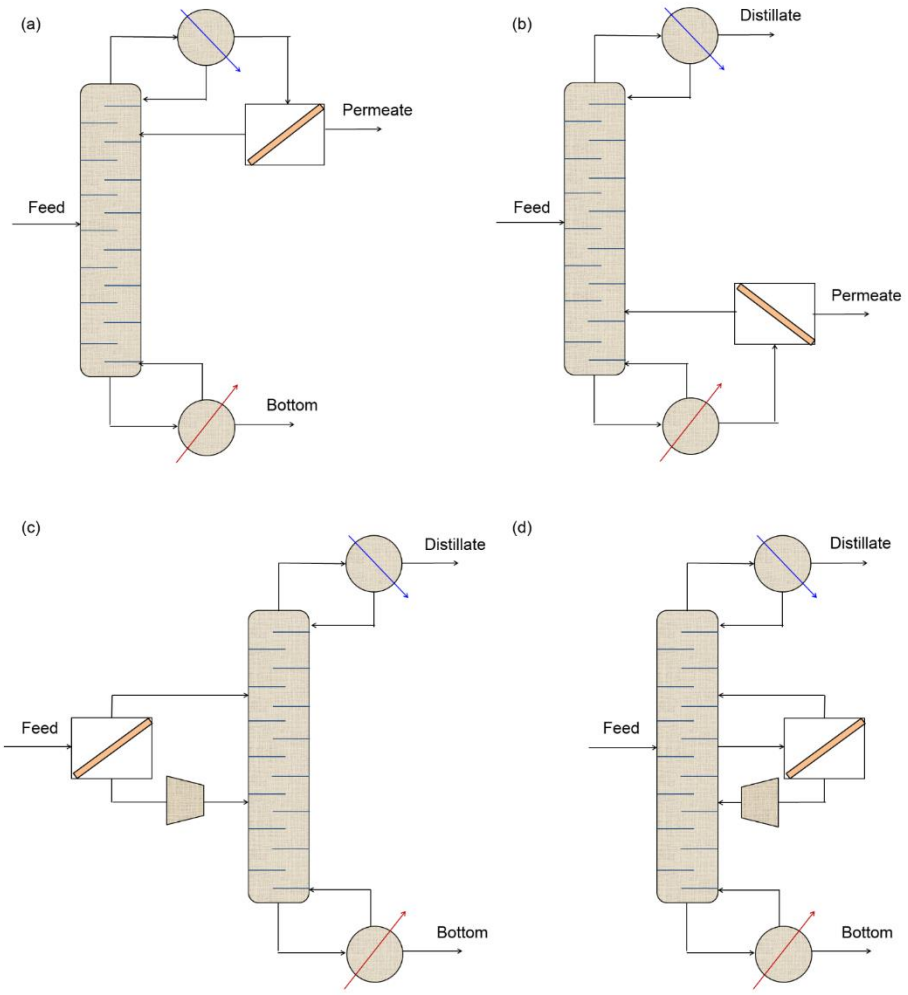

Figure 2.5: Schematic of hybrid membrane-distillation systems consisting of a single distillation unit and a single membrane unit. **(a)** top-hybrid configuration, **(b)** bottom-hybrid configuration, **(c)** series hybrid configuration, and **(d)** parallel hybrid configuration.

2.5 Concluding remarks

The permeation through a zeolite membrane is a complex interplay of adsorption and diffusion properties of permeating components. Further, the non-idealities in both the adsorption and diffusion phenomenon, such as co-adsorption due to hydrogen bonding and intersection blocking, respectively, can introduce more complexities. In addition to the adsorption and diffusion based transport through zeolite layer, factors such as mass transfer through the porous support, the use of a sweep gas, concentration polarization phenomenon

and presence of defects should also be included. The models used in the literature are usually based on only ideal adsorption-diffusion through the zeolite layer. The effects of non-idealities and external resistances are usually neglected. This results in discrepancy between the results obtained from the model and the experiments. Here, the membrane model is developed considering all the above mentioned transport phenomenon and further integrated with process-scale model for both stand-alone membrane processes and hybrid membrane-distillation processes. This first-of-its-kind modeling approach does not only improve the understanding of zeolite membrane processes but is also significant from an engineering perspective as it can be used as a template to rigorously design and optimize membrane systems.

Chapter 3: Butane isomer separation using hybrid membrane-distillation

3.1 Introduction

Butanes offer a great opportunity for implementation of zeolite membrane technology. While n-butane is primarily used in liquefied petroleum gas (LPG) as a cooking and heating fuel and in petrochemical industry as a feedstock for producing ethylene and butadiene, the major application of i-butane is in refineries where it is used as a blending agent mixed in gasoline. LPG accounts for the biggest share of butane application consisting 66% whereas petrochemical and refineries accounts for 17% and 15% respectively. Their global market is growing at an annual rate of 2.46% in terms of demand and at a CAGR of 8.9% in terms of revenue [6]. Currently, the industrial separation of butane isomers is accomplished using distillation, and due to the close boiling-point of the components, it is considered as one of the most energy-intensive distillation separations.

Zeolite membrane separation has also been proposed as a possible solution for butane isomer separation as n-butane is both the preferentially adsorbing and the preferentially diffusing component resulting in synergetic separation [120].

3.2 Adsorption modeling

3.2.1 Single component adsorption parameters

The single component adsorption properties of butane isomers in MFI zeolites have been widely studied [60,121–132]. Adsorption isotherms and the heats of adsorption have been determined by various experimental, including adsorption calorimetry [121] , gravimetric analysis [122,123] and tapered element oscillating microbalance [124,125] experiments, and molecular simulations using configurational-bias Monte Carlo methods

[60,127–129,132] and were found to be in good agreement with one another. Volumetric adsorption experiments have also been performed on silicalite-1 pellets for *n*-butane [126]. The results from these techniques are in agreement to one another, and isotherms for *n*-butane and *i*-butane at $T \sim 300$ K are shown in **Figure 3.1a and 3.1b** respectively.

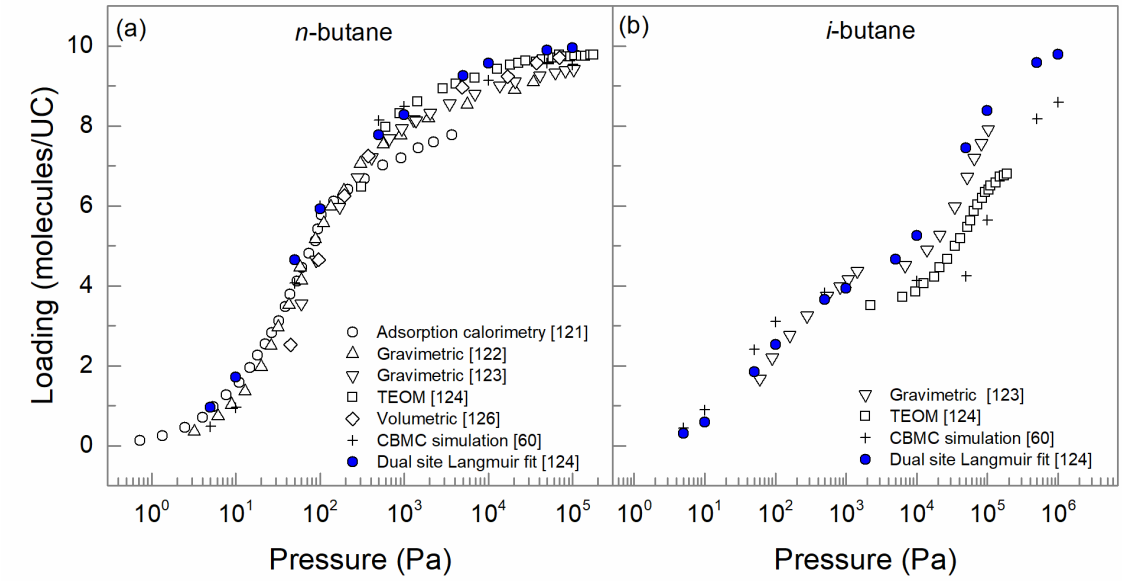

Figure 3.1: Single component adsorption isotherms for **(a)** *n*-butane **(b)** *i*-butane on MFI crystals measured and simulated using various techniques in the range $T = 300$ K - 308 K.
○: Adsorption calorimetry 300 K Stach et al. [121],△: Gravimetric 303 K Richards and Rees [122], ▽: Gravimetric 308 K Sun et al. [123], □: TEOM 303 K Zhu et al. [124], ◇: Volumetric 300 K Abdul-Rehman et al. [126], +: Molecular simulation 300 K Vlugt et al. [60], ●: Dual site Langmuir fit 300 K Zhu et al. [124]. For volumetric method [11], silicalite-1 pellets were used and the amount of adsorbent is corrected for the binder weight assuming that no adsorption takes place on the binder.

The adsorption has been described in terms of a volume filling process with two different types of sites – channels and intersections, and thus the dual-site Langmuir isotherm;

$$q_{\mathrm{i}} = \frac{q_{\mathrm{i,a}}^{\mathrm{sat}} k_{\mathrm{i,a}} P}{1 + k_{\mathrm{i,a}} P} + \frac{q_{\mathrm{i,b}}^{\mathrm{sat}} k_{\mathrm{i,b}} P}{1 + k_{\mathrm{i,b}} P} \tag{3.1}$$

where q is the loading, q^{sat} is the saturation loading, *k's* are the Langmuir constants, P is the pressure and 'a' and 'b' represent the two sites, has been used to model the adsorption

isotherm [125]. *n*-Butane prefers channels over intersections for loading up to 8 molecules/UC (unit cell) and then starts filling intersections at higher pressure. On the other hand, *i*-butane (or 2-methylpropane) is preferentially adsorbed in the intersections for loading up to 4 molecules/UC and the channels are occupied in addition at high pressure. The loading values predicted by the model are in good agreement with those obtained by experiments and simulations. The heat of adsorption calculated from the fitted dual site Langmuir isotherm are also in fair agreement with the values determined independently from calorimetry experiments [130,131]. Calorimetry measurements [130,131] show that, as the coverage increases, the heat of adsorption of *n*-butane initially increases from ~50 kJ/mol to ~60 kJ/mol before finally decreasing near saturation, which is in agreement with the calculated values (from dual-site Langmuir fit) of 56.1 kJ/mol in the channels (0 to 8 molecules/ UC) and 49.5 kJ/mol in the intersections (8 to 10 molecules/UC) [125]. For *i*-butane, the heat of adsorption increases from ~48 kJ/mol (0 – 4 molecules/UC) to ~56 kJ/mol as loading increases from 4 – 8 molecules/UC [130], which is in fair agreement with the calculated values (from dual-site Langmuir fit) of 46 kJ/mol in the intersections (0 to 4 molecules/ UC) and 65.6 kJ/mol in the channels (4 to 10 molecules/ UC) [125]. The *n*-butane Henry's coefficients obtained from molecular simulations [127–129] are also nearly equal to the values calculated using dual-site Langmuir fit as shown in **Figure 3.2.** Thus, **t**he dual-site Langmuir isotherm with parameter values reported in [125] accurately describes the experimental and simulation results, and is also used here to determine the single component adsorption properties.

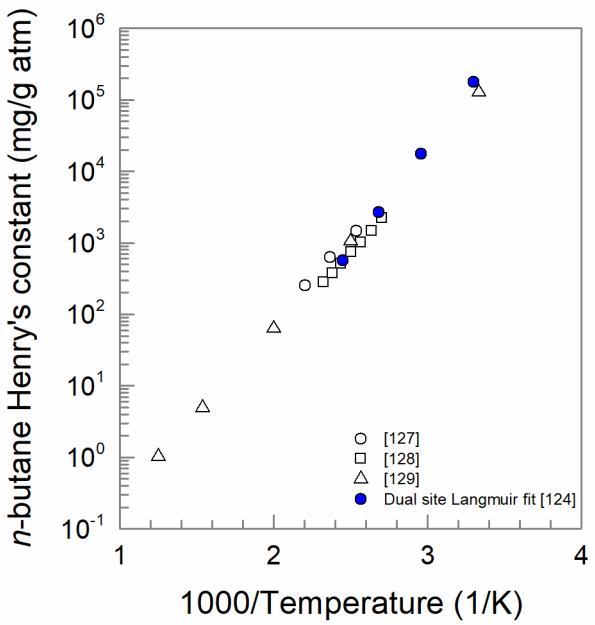

Figure 3.2: *n*-Butane Henry's coefficients for adsorption on MFI crystals obtained using molecular simulations at various temperatures.
○: June et al. [127], □: Smit and Siepmann [128], △: Maginn et al. [129], ●: Dual site Langmuir fit - Zhu et al. [124].

3.2.2 Multi component adsorption parameters

Although single component adsorption of butane isomers on MFI zeolites is well established, only a few studies exist for mixture adsorption [53,60,133,134]. Configurational-bias Monte Carlo (CBMC) simulations [60,133] have been carried out to determine the equimolar mixture adsorption at T = 300 K. Both isomers were shown to follow single-component behavior up to a total loading of 4 molecules/UC. For higher loadings, *n*-butane tends to squeeze-out *i*-butane molecules causing a maximum of *i*-butane loading at a total loading of 4 molecules/UC. The squeezing-out effect has been attributed to higher packing efficiency of *n*-butane versus *i*-butane molecules in the zeolite channels. For a total loading greater than 4 molecules/UC, *n*-butane loading increases with pressure while *i*-butane loading decreases with pressure. These results are also in agreement with infra-red microscopy (IRM) experiments [134]. Similar conclusions were also reached for higher temperatures by Lu et al. [53]. The same phenomenon has also been observed for

hexane isomers (*n*-hexane/2-methyl-pentane), i.e., linear isomer occupies both channels and intersections while the branched isomer is located preferentially at intersections [120,133]. At high pressure (total loading greater than 4 molecules/UC), the adsorption of the linear isomer is favored by squeezing out the branched isomer. This leads to high selectivity of the linear isomer making MFI type of zeolite an attractive choice for these isomer separations.

The squeezing-out effect also introduces non-idealities in the mixture and leads to failure of the Ideal Adsorption Solution Theory (IAST), which is widely used in predicting mixture isotherms. To model the mixture adsorption isotherm, Vlugt et al. [60] suggested two different mixture rules based on extended Langmuir multi-component isotherms. The first mixture rule has been shown to underpredict *n*-butane loading and overpredict *i*-butane loading, while the other mixture rule overpredicts *n*-butane loading and underpredicts *i*-butane loading. A combination of mixture rule 1 and mixture rule 2 was thus employed to predict the values obtained by molecular simulation at T = 300 K. The drawback of this model is that it is not thermodynamically consistent and fails to predict the simulation results at higher temperature. Lu et al. [53] proposed a surface area corrected IAST (SAC-IAST) to account for the different area/sites available for *n*-butane (channels and intersections) and *i*-butane (intersections) mixture adsorption. They introduced a vapor mole-fraction dependent parameter to fit the deviation from IAST. The drawback of this model is that there is no capability to account for the changes in deviations with changing total pressure. As stated earlier, deviations are small at low pressure when both molecules adsorb independently as compared to high pressure where the non-idealities start to play an important role. Moreover, this model can only be used when mixture adsorption data is available for various mole fractions. Here, a Real Adsorption Solution Theory (RAST) is used to model the mixture isotherm. The activity coefficients based on the Wilson equation

are used here, and the resultant mixture adsorption isotherm at T = 323 K and T = 343 K is shown in **Figure 3.3**, which shows good agreement with the simulation data.

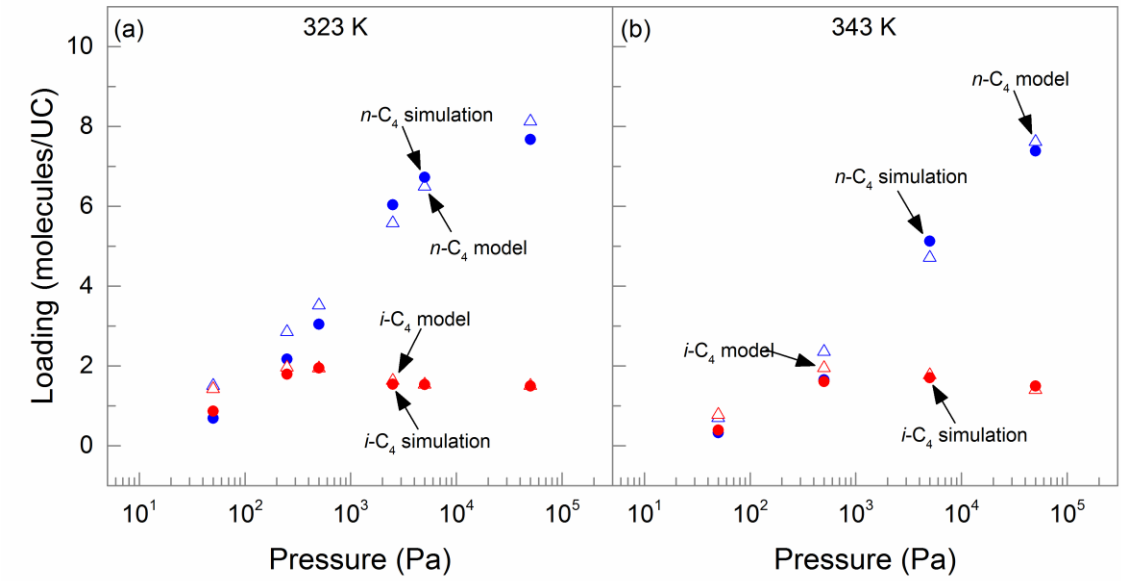

Figure 3.3: Adsorption isotherm for an equimolar mixture of *n*-butane and *i*-butane at **(a)** T = 323 K, and **(b)** T = 343 K; RAST model compared to molecular simulation data by Lu et. al. [53].
△: *n*-butane model, ●: *n*-butane simulation, △: *i*-butane model, ●: *i*-butane simulation

3.3 Diffusion modeling

The methods for determining micropore diffusion coefficients can be broadly classified into microscopic, macroscopic and molecular simulation methods. The diffusion of *n*-butane and *i*-butane in MFI zeolite crystals has been extensively studied in the literature using all three approaches [75,83,135–169]. However, the diffusion coefficients reported in the literature differ from one another by up to three orders of magnitude. Thus, the data should be carefully reviewed before selecting the diffusivity, as the permeation across the membrane is crucially dependent on these coefficients. Here, the literature data are organized and analyzed in a systematic manner in an attempt to select the most appropriate values of diffusion coefficients.

3.3.1 Microscopic techniques for diffusion properties

Nuclear magnetic resonance (NMR) and quasi-elastic neutron scattering (QENS) are the most common microscopic techniques for measuring micropore diffusion coefficients. Various studies [135–141] have been performed to measure the *n*-butane diffusivity in MFI crystals using these techniques and the measured self-diffusion coefficients are shown in **Figure 3.4**. Datema et al. [135] and Heink et al. [136] have also studied diffusion in ZSM-5 (high Al content MFI-type zeolite) crystals with a Si/Al ratio of 53 and 13 respectively and their results (**Figure 3.4**) show that Si/Al ratio does not influence the diffusivity. The loading in molecules/UC corresponding to the different studies is also shown and stated in the figure caption. Since the self-diffusion coefficient should decrease with loading due to the correlation effects, the values results are in good agreement to one another except for the diffusivities obtained by Fernandez et al. [139] and Banas et al. [140]. The values obtained by Fernandez et al. [139] are an order of magnitude higher than the other NMR results at the same loading. Although the loading is not specified in the results obtained by Banas et al. [140], the values are significantly lower even for higher loadings. The existence of these outliers may be attributed to variability of crystal quality including crystal twinning, crystal intergrowth, crystal defects, etc. The temperature dependence of the diffusion coefficient was also studied by Datema et al. [135] and Heink et al. [136] and the activation energy was found to lie between 6 kJ/mol and 8 kJ/mol.

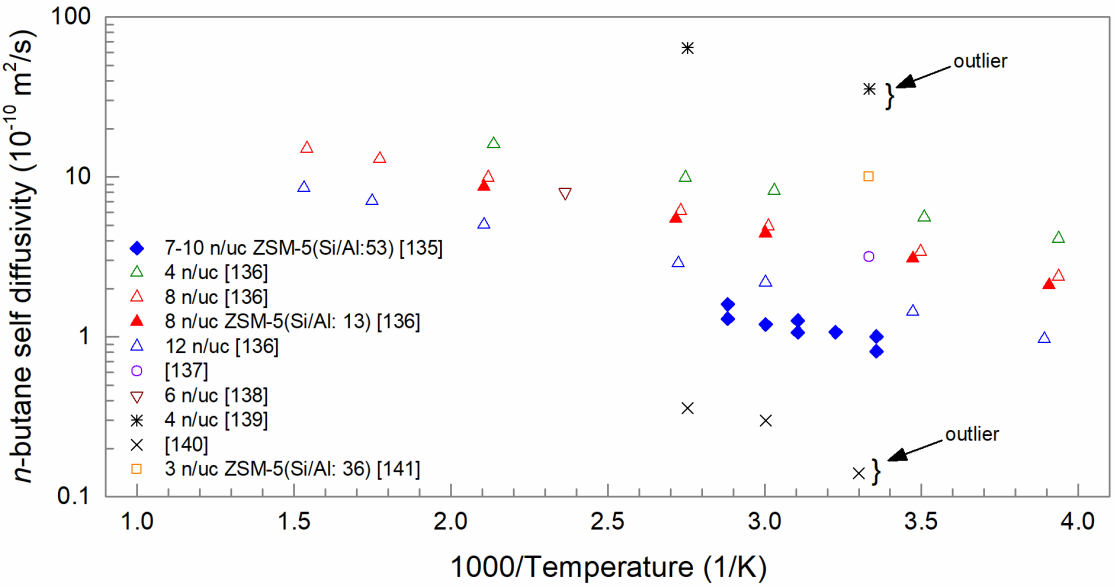

Figure 3.4: *n*-butane self-diffusion coefficients in MFI crystals obtained using microscopic techniques (NMR and QENS) at various temperatures. The corresponding loading in molecules/UC and Si/Al ratio for ZSM-5 crystals are shown in the legend.
◆: 7-10 molecules/UC in ZSM-5(Si/Al = 53) Datema et al. [135], △: 4 n/uc Heink et al. [136], △: 8 n/uc Heink et al. [136], ▲: 8 n/uc in ZSM-5(Si/Al = 13) Heink et al. [136], △: 12 n/uc Heink et al. [136], ○: Pampel et al. [137], ▽: 6 n/uc Brandani et al. [138], ✳: 4 n/uc Fernandez et al. [139], ×: Banas et al. [140], □: 3 n/uc in ZSM-5(Si/Al = 36) using QENS Jobic [141].

Only a couple of NMR studies of *i*-butane diffusion in silicalite-1 (low Al content MFI-type zeolite) could be found in the literature. They were performed by Fernandez et al. [139] and Banas et al. [140] and the results are in agreement with each other as shown in **Figure 3.5**. However, the corresponding single component *n*-butane/*i*-butane diffusivity ratio was found to be ~3000 and ~15, respectively. This large discrepancy is due to the difference between *n*-butane diffusivities found in these studies. As stated earlier, the *n*-butane diffusivities obtained in these studies have large discrepancies when compared to the other NMR measurements and thus the results cannot be assured to be accurate. Diffusion coefficients, using QENS, in ZSM-5 crystals (Si/Al = 36) at a loading of 3 molecules/UC have been obtained by Millot et al. [142] and shown in **Figure 3.5**. These

experiments were performed at higher temperatures (> 450 K) and the activation energy was determined to be 17 kJ/mol. Besides QENS, another technique based on neutron scattering, known as neutron spin-echo (NSE), has also been used to determine the *i*-butane diffusivity in silicalite [170]. This technique is primarily used if the diffusivity is too small to be measured by conventional QENS instruments and is considered to be more accurate than the QENS [171,172]. The diffusivity measured by the NSE method was found be an order of magnitude larger than that measured by QENS. The activation energy, using diffusivities measured by NSE [170], was found to be 22.6 kJ/mol which is also higher than that determined by QENS [142].

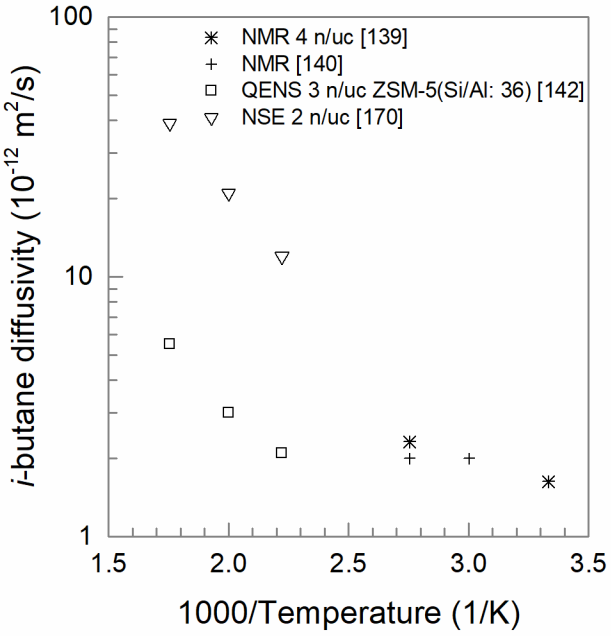

Figure 3.5: *i*-butane self-diffusion coefficients in MFI crystals obtained using microscopic techniques (NMR, QENS and NSE) at various temperatures. The corresponding loading in molecules/UC and Si/Al ratio for ZSM-5 crystals are shown in the legend.
✳: 4 molecules/UC Fernandez et al. [139], ×: Banas et al. [140] , □: 3 n/uc in ZSM-5 (Si/Al=36) using QENS Millot et al. [142], △: 2 molecules/UC O'Malley et al. [170].

3.3.2 Macroscopic techniques for diffusion properties

Among the macroscopic techniques, pulse chromatography [143–146], zero length chromatography (ZLC) [140,147–151], permeation measurements through single crystal

membrane (SCM) [152–155], interference microscopy [156–159] and frequency response (FR) [160,168] methods have been widely studied for calculating butane diffusivity in MFI crystals. The macroscopic techniques usually determine the corrected diffusivity or Fick's diffusivity while microscopic techniques provide the self-diffusivity. However, the values from different techniques can be compared at zero loading as all three kinds of diffusivities (self, corrected and Fick's) are equal at zero loading. Moreover, Fick's (D) and corrected diffusivities ($Đ$) are related as ($Đ = D/\Gamma$), where the thermodynamic factor (Γ = d ln p / d ln θ) can be determined from the adsorption isotherm.

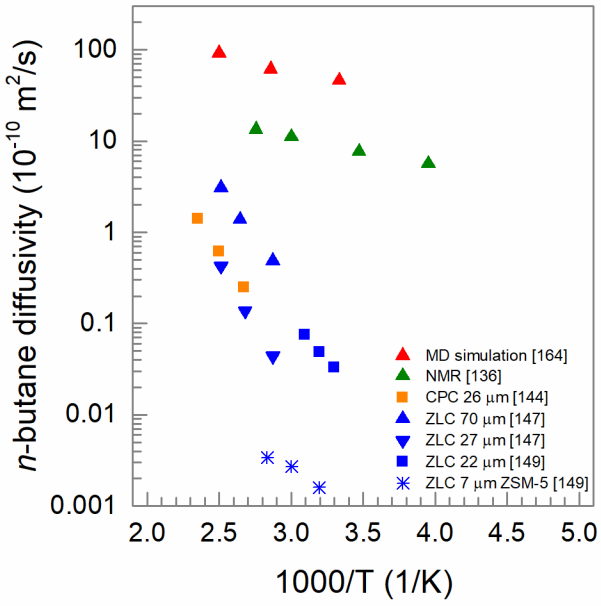

Figure 3.6: *n*-butane corrected diffusivity in MFI crystals obtained at infinite dilution using macroscopic techniques (CPC and ZLC) for various temperatures. Values obtained using NMR and molecular simulations are also shown for comparison.
▲: MD simulation Runnebaum and Maginn [164], ▲: NMR Heink et al. [136], ■: CPC 26 µm crystal Hufton and Danner [144], ▲: ZLC 70 µm Hufton and Ruthven [147], ▼: ZLC 27 µm Hufton and Ruthven [147], ■: ZLC 22 µm Jiang and Eic [149], ✳: ZLC 7 µm in ZSM-5 Jiang and Eic [149].

Hufton and Danner [144] carried out concentration pulse chromatography (CPC) experiments at infinite dilution using silicalite-1 crystals. The *n*-butane diffusion coefficients (**Figure** 3.**6**) were found to be at least an order of magnitude lower as compared

to microscopic measurements. The authors have concluded that these *n*-butane diffusion coefficients must be considered as a lower limit of the true diffusion coefficients since the actual values are too large to be measured via chromatography. The measured activation energy (45 kJ/mol) was also found to be almost equal to the heat of adsorption (50 kJ/mol) indicating insignificant microporous mass transfer resistance. In contrast to *n*-butane, large microporous resistance for *i*-butane allowed accurate measurement of diffusion coefficient. The diffusion coefficients obtained for two different crystal sizes (26 μm and 36 μm) are shown in **Figure 3.7** and are nearly equal. The activation energy was computed to be 24.4 kJ/mol.

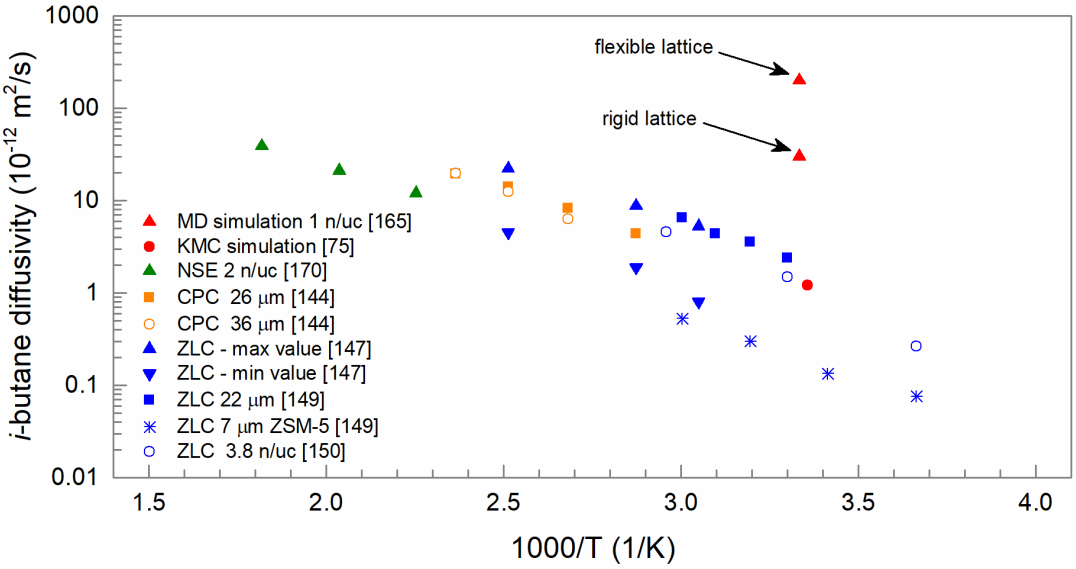

Figure 3.7: *i*-butane corrected diffusivity in MFI crystals obtained using macroscopic techniques (CPC and ZLC) for various temperatures. Self-diffusivity values obtained using NSE and molecular simulations are also shown for comparison. Values shown are at infinite dilution (zero loading) except wherever mentioned.
▲: MD simulation 1 molecule/UC Bouyermaouen and Bellemans [165], ●: KMC simulation Chmelik et al. [75], ▲: NSE 2 molecule/UC O'Malley et al. [170], ■: CPC 26 μm crystal Hufton and Danner [144], ○: CPC 36 μm Hufton and Danner [144], ▲: ZLC max value Hufton and Ruthven [147], ▼: ZLC min value Hufton and Ruthven [147], ■: ZLC 22 μm Jiang and Eic [149], ✳: ZLC 7 μm in ZSM-5 Jiang and Eic [149], ○: ZLC 3.8 n/uc Zhu et al. [150].

Pulse chromatography experiments have also been performed by Chiang et al. [143] and Nijhuis et al. [145,146]. Chinag et al. [143]obtained *n*-butane diffusion coefficients

which are 3 orders of magnitude lower than other chromatography or macroscopic techniques. Moreover, *n*-butane and *i*-butane diffusion coefficients were found to be similar. This discrepancy is attributed to the small silicalite-1 crystals (R ~ 1 μm) used in their study which provide negligible microporous resistance and thus transport in these crystals is dominated by external resistances. Nijhuis et al. [145,146] applied a transient pulse-response technique to determine the diffusion coefficient at high temperatures. They obtained the pre-exponential factor of diffusivity and the activation energy by fitting the experimental data. Though these diffusion parameters are in good agreement with values obtained from microscopic techniques, their fitted value of diffusion coefficient is an order of magnitude higher than their experimental value (10^{-10} m^2/s) at 400 K. The experimental activation energy is also much higher than the fitted value of 7.3 kJ/mol in the range of 400 K – 450 K. For *i*-butane, only the fitted results have been reported and the diffusion coefficients and activation energy (28.9 kJ/mol) are in agreement to the results obtained by Hufton and Danner [144].

Hufton and Ruthven [147] have studied diffusion in silicalite-1 crystals using ZLC technique. To this end, a dimensionless parameter 'L' is used to determine whether the process is equilibrium controlled (L > 10) or diffusion controlled (L < 1). For *n*-butane, the L values calculated were found to lie between 1 and 4 which are smaller than those required for diffusion-controlled process. Furthermore, the activation energy (41.6 kJ/mol) was found to be similar to the heat of adsorption (50 kJ/mol). The diffusion coefficients measured using different sized crystals (shown in **Figure 3.6**) shows that the diffusivity increases with crystal size indicating that the external resistance also plays a substantial role. The authors have concluded that the permeation of *n*-butane is too fast to be measured using the ZLC method, and the calculated diffusion coefficient must be taken as a lower limit of the true diffusion coefficient. For *i*-butane, diffusivities in silicalite-1 crystals

yielded L > 50 indicating significant micropore resistance. The diffusivities were obtained for different crystal sizes using short-time and long-time methods. Since the individual data points lie close to each other and are not clearly distinguishable in the original figure, only the highest and lowest values of diffusivities are shown in **Figure 3.7**; the average values are in agreement to the values obtained using CPC experiments. The activation energy of 23.1 kcal/mol is also similar.

Jiang and Eic and co-workers [148,149] have studied butane isomer permeation in both silicalite-1 crystal and ZSM-5 crystals using ZLC techniques. For both isomers, diffusivities in silicalite-1 crystals were found to be higher than ZSM-5 crystals (**Figure 3.6** for *n*-butane and **Figure 3.7** for *i*-butane) and contradicts the NMR results for *n*-butane where the Si/Al ratio does not influence the diffusivity. However, L values for *n*-butane in these ZLC experiments [149] were found to be < 5 which indicates that the transport may be equilibrium controlled rather than diffusion controlled. Another possible reason for the discrepancy in diffusivity might be the difference in the crystal size (R = 22 μm silicalite-1 crystals and R = 7 μm for ZSM-5 crystals) as Hufton and Danner [144] also found this discrepancy in CPC measurements where the transport was governed by the external resistance. For *i*-butane, L ~ 10 for silicalite-1 crystals (R = 22 μm) and ~ 5 for ZSM-5 crystals (R = 7 μm). The diffusivities obtained with silicalite-1 crystals are nearly equal to those obtained using CPC, while values for ZSM-5 are 5 to 10-fold lower. Thus the discrepancy for ZSM-5 crystals can be attributed to their small size which have low microporous resistance and results in inaccurate measurement of the diffusion coefficient. Moreover, Zhu et al. [150] have also mentioned that the sorbate concentration in these ZSM-5 crystals, which was maintained at 0.025 vol%, corresponds to a loading of 0.26 molecules/UC and 2.95 molecules/UC at 333 K and 273 K, respectively. At these conditions, the adsorption isotherm lies outside the Henry's regime and contradicts the

assumption used in the ZLC technique. Furthermore, the diffusivity also decreases at finite loading, which should also be taken into account as all the other values have been reported at infinite dilution.

Zhu et al. [150], investigated the diffusivities of *i*-butane at finite loading in silicalite-1 using the ZLC technique. They modified the ZLC modeling approach to include the effect of non-linear adsorption equilibrium to calculate the average corrected diffusivities over the finite loading in the sample. The results for 3.84 molecules/UC are shown in **Figure 3.7**. The values are in agreement to the other values but it must be noted that they are average values over a finite loading while the other results are shown for infinitely diluted loading.

Diffusion coefficients of *n*-butane in silicalite-1 have also been measured using permeation across a single crystal membrane. Hayhusrt et al. [152] and Shah et al. [153] used the time-lag technique to determine the average Fick's diffusivity. Sun et al. [155] used the transient mass response method to determine the average corrected diffusivity, while Talu et al. [154] used steady-state permeation measurements to determine the average corrected diffusivity in z-direction. Among other macroscopic experiments, Shen and Rees [160] and Shen et al. [168] used frequency response methods and Moller et al. [161] used sorption uptake curves to determine the *n*-butane diffusivity in MFI crystals. The values obtained in the above mentioned experiments are comparable to the values obtained by other macroscopic techniques (CPC and ZLC) but are at least an order of magnitude smaller than the values obtained by microscopic techniques, again indicating the inadequacy of macroscopic methods to determine *n*-butane diffusivity in MFI.

Other macroscopic techniques that have been employed to measure *i*-butane diffusivity in MFI crystals include permeation through single crystal membrane [153] and application of interference microscopy along with sorption/desorption concentration profile

determination [156–159]. These techniques provide average Fick's diffusivities over a finite loading in the zeolite sample. The diffusivity was found to be of the order of 10^{-12} m^2/s and almost constant over an average loading of 1-4 molecules/UC. As stated earlier, Fick's (D) and corrected diffusivity ($Đ$) are related as ($D = Đ \times \Gamma$) where Γ is the thermodynamic factor ($\Gamma = \mathrm{d} \ln p / \mathrm{d} \ln \theta$). For *i*-butane, Γ increases with loading and corrected diffusivity decreases with loading for up to 4 molecules/UC, and thus explains the constant Fick's diffusivity obtained in these macroscopic methods. Iso-butane diffusivities measured by various macroscopic methods are also compared to that obtained by NSE microscopic technique (**Figure 3.7**). Diffusivities obtained by NSE method are found to only marginally lower than those obtained by CPC method. This may be due to the reason that the NSE experiments are carried out at a finite loading of 2 molecules/UC while the CPC experiments are carried out at infinite dilution. The activation energy of 22.6 kJ/mol from NSE is also in agreement with that obtained by macroscopic techniques (of 24.5 kJ/mol).

3.3.3 Molecular simulations for diffusion properties

Several molecular simulation studies have been performed to study *n*-butane diffusion in silicalite-1 crystals [83,139,162–166,169]. Self-diffusivities obtained using MD (molecular dynamics) simulations at $T \sim 298$ K for various loadings are shown in **Figure 3.8**.

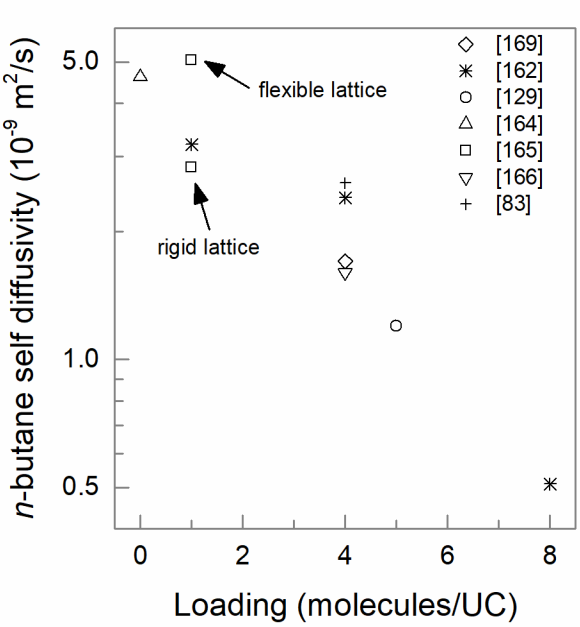

Figure 3.8: *n*-butane self-diffusion coefficients in MFI crystals obtained at T = 300 K using molecular simulation techniques for various loadings.
◇: Goodbody et al. [169], ✳: June at al. [162], ○: Maginn et al. [129], △: Runnebaum and Maginn [164], □: Bouyermaouen and Bellemans [165], ▽: Gergidis and Theodorou [166], +: Krishna and van Baten [83].

In all these MD simulations, a united atom model of *n*-butane was considered in a rigid silicalite-1 structure. Bouyermaoeun and Bellemans [165]also studied the effect of vibrations of the silicalite-1 lattice on the diffusivity and showed that the vibrations ease the molecular displacements leading to larger diffusion coefficients. Maginn et al. [163] used a combination of Brownian motion theory and transition state theory to determine *n*-butane self-diffusivity. Though the exact loading is not mentioned in this study, the diffusivity is in agreement with other MD simulations for 5 molecules/UC. However, the diffusion coefficients predicted by molecular simulations are an order of magnitude higher than those obtained by microscopic techniques **(Figure 3.6)**. This discrepancy is usually attributed to the assumption of perfect crystals in the simulation while the presence of lattice defects and acid sites in the real crystals used in microscopic measurements inhibit the mobility of the diffusing species. Runnebaum and Maginn [164] also mentioned the

choice of a united atom model as a possible reason, as it has been shown to yield enhanced mobility. Maginn et al. [163]and Runnebaum and Maginn [164] also studied the effect of temperature and reported an activation energy of 6 kJ/mol and 7 kJ/mol respectively which is in good agreement to the microscopic results.

MD simulations to determine the diffusion coefficients tend to be computationally expensive for slowly permeating species ($Đ < 10^{-11}$ m^2/sec). As a result, only a single MD study could be found in literature for *i*-butane in silicalite-1; Bouyermaoeun and Bellemans [165] computed the diffusivity at a loading of 1 molecule/UC for both the rigid and flexible lattice structures which is found to be an order of magnitude larger than the macroscopic measurements as shown in **Figure 3.7**. In other molecular simulation studies for *i*-butane diffusion, Paschek and Krishna [167] and Chmelik et al. [75] employed infrared microscopy along with kinetic Monte Carlo simulations to predict the loading dependency of *i*-butane diffusivity at T = 298 K and have shown that the corrected diffusivity exhibits a strong inflection at a loading of 4 molecules/UC (**Figure 3.9**). The initial decrease is attributed to the correlation effects while the strong inter-molecular repulsions between *i*-butane molecules occupying channels at loading > 4 molecules/UC causes the corrected diffusivity to increase with further loading. It was also shown that Fick's diffusivity is essentially constant (10^{-12} m^2/sec) up to a loading of 4 molecules/UC and then increases up to 10^{-11} m^2/sec for 8 molecules/UC. Similar conclusions have also been reached by Millot et al. [142] by measuring *i*-butane permeation flux across ZSM-5 membrane. Thus, diffusivities obtained by kinetic Monte Carlo simulations are in good agreement with those obtained by other macroscopic measurements and microscopic measurements employing NSE method.

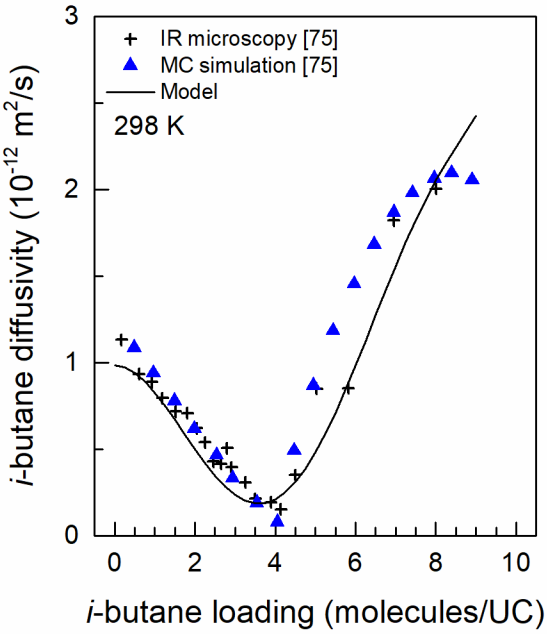

Figure 3.9: Loading dependency of *i*-butane Maxwell-Stefan diffusion coefficient determined using Kinetic Monte Carlo simulation and infra-red microscopy experiments at T = 298 K. +: IR microscopy Chmelik et al. [75], ▲: MC simulation Chmelik et al. [75], —: Model.

3.3.4 Single component diffusion parameters

Based on the analysis presented above, it is safe to conclude that the current macroscopic techniques are inadequate in determining the *n*-butane microporous diffusion coefficient, and the diffusivities predicted by molecular simulations are an order of magnitude higher than those obtained from the microscopic methods such as nuclear magnetic resonance (NMR) and quasi-elastic neutron scattering (QENS). Here, diffusivities obtained by NMR [136] are selected for *n*-butane based on the opinion that they closely represent the intrinsic transport in the zeolite pores. The concentration dependence is modeled using the strong confinement scenario [43], as both NMR and molecular simulation studies show a decrease in diffusivity with increase in loading. For *i*-butane, diffusivities obtained by macroscopic techniques [144] and kinetic Monte Carlo simulations [75] are found to be in good agreement with each other. Among the microscopic methods to measure *i*-butane diffusivities, which are as low as of the order of

10^{-12} m^2/s, values obtained by neutron spin-echo (NSE) [170] technique are considered to be more accurate than NMR and QENS[142], and are in agreement with those obtained by macroscopic measurements and kinetic Monte Carlo simulations The activation energy of 22.6 kJ/mol from NSE [173] is also in agreement with that obtained by macroscopic techniques (of 24.5 kJ/mol) [144]. The pre-exponential factor of diffusion coefficient and the activation energy for both isomers selected for developing the model are shown in **Table 3.1**.

Table 3.1. Pre-exponential factor of diffusion coefficient at zero loading and the corresponding activation energy for butane isomers in MFI crystals.

Component	Pre-exponential factor (10^{-8} m^2/s)	True activation energy (kJ/mol)
n-butane	1.03	6.2
i-butane	2.19	24.5

3.3.5 Multi-component diffusion parameters

Generally, the corrected diffusivity of a species in a mixture is taken equal to its single component corrected diffusivity at the same total fractional loading. However, for a butane isomer mixture in MFI zeolite, presence of *i*-butane molecules has shown to adversely affect the *n*-butane diffusion. This effect is caused due to a phenomenon known as intersection blocking [139]. The branched hydrocarbon preferentially adsorbs at the intersection of MFI crystals which causes blocking of the pore and severely reduces the diffusivity of the linear alkane. However, at high pressure (total loading greater than 4 molecules/UC), the branched isomer loading decreases. Therefore, the effect of intersection blocking is diminished and transport of the linear isomer is enhanced. The synergy of adsorption and diffusion, both favoring the linear isomer, is uncommon, as most separations are based on either selective adsorption or selective membrane permeation, and

is a main reason for using MFI membranes for butane-isomer and hexane-isomer separations [120,134].

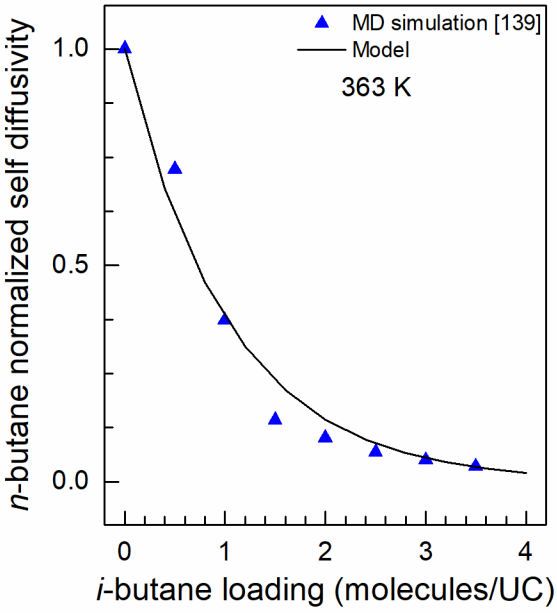

Figure 3.10: Effect of *i*-butane loading on *n*-butane diffusion coefficient in a mixture of butane isomers at T = 363 K. ▲: MD simulation Fernandez et al. [139], —: Model

The effect of *i*-butane loading on *n*-butane self-diffusion coefficients has been analyzed using MD simulations [139], which show that the *n*-butane diffusivity is reduced to nearly zero as *i*-butane loading is progressively increased to 4 molecules/UC. At 4 molecules/UC, *i*-butane molecules occupy almost every intersection which leads to a complete blockage. While the *n*-butane diffusivity in a butane isomer mixture has been obtained at a total loading of 4 molecules/UC, the effect of *i*-butane loading on *n*-butane diffusion is decoupled from the effect of *n*-butane loading by using the strong confinement model for *n*-butane loading dependency of *n*-butane diffusivity. To model *i*-butane loading dependency on *n*-butane diffusivity, an exponential decay:

$$Đ_{nB}(\theta_{iB}) = Đ^{0}_{nB} \exp(-\lambda\theta_{iB}) \tag{3.2}$$

where $Đ^{o}_{nB}$ is the single component *n*-butane diffusivity and θ_{iB} is the *i*-butane fractional loading, is used to model the simulation data and is shown in **Figure 3.10.**

The exchange coefficients ($Đ_{ij}$) are modeled using the Vignes correlation [55]. The improved correlation in [36] also reduces to the Vignes correlation for butane isomer mixture as the saturation loadings of both isomers are the same.

3.3.6 Discrepancy between diffusion properties in crystals and membranes

In addition to the microscopic, macroscopic and molecular simulation methods employed to obtain the diffusivities in MFI crystals, single component *n*-butane corrected diffusivity has also been determined from permeation measurements through MFI membranes made up of intergrown crystals.

Kapteijn, Mouleijn and co-workers [174–177] have carried out steady state *n*-butane permeation experiments through a 40 μm thick membrane on a stainless steel support. To obtain the diffusivity from these measurements, adsorption was modeled using a single-site Langmuir isotherm and the effects of the support were incorporated using support porosity. Kapteijn et al. [174] found that the corrected diffusivity was an order of magnitude smaller than the values obtained by NMR measurements. The reported activation energy of 30 kJ/mol is also considerably higher than the 8 kJ/mol obtained from NMR measurements. Bakker et al. [175] later used the detailed molecular diffusion theory to model permeation through the support layer but the diffusivity values were still found to be lower. Van de Graaf et al. [176] also found similar results and concluded that the permeation through a membrane is fundamentally different than diffusion in a crystal. The higher activation energy, as compared to the values obtained using microscopic techniques, was attributed to higher energy barrier due to the randomly intergrown crystals. The reported activation energy values may also be larger because these values are determined at different finite loadings while the activation energy from NMR measurements was

calculated at zero loading. After incorporating the loading dependency of diffusivity, the activation energy (at zero loading) from permeation experiments is calculated to be 9 kJ/mol, which is nearly equal to that obtained in MFI zeolite crystals using NMR measurements. Bakker et al. [177], by carrying out the permeation experiments with *i*-octane, also stated that these membranes contained non-zeolitic pores, which are larger than the zeolite pores and result in larger flux and thus overestimation of the diffusivity. Moreover, SEM images of the membranes [176] show that the crystals are loosely intergrown and thus the effective thickness of the membrane should be even less than the visual thickness of ~40 μm. For a given flux, a higher than actual thickness also results in overestimation of the diffusivity. This implies that the actual diffusivity through the membranes could be even lower than the values obtained from the steady state permeation experiments and therefore, their differences from the values obtained by NMR could be even more pronounced.

Burgraaf and co-workers [178–180] have studied *n*-butane permeation through 3 μm thick membranes supported on 2 mm thick alumina support. The permeation data were analyzed using single-site Langmuir isotherm, and support porosity to account for support effects. The diffusivity values were found to be two orders of magnitude lower than those obtained by NMR measurements.

Noble, Falconer and co-workers [44,181,182] have developed a method to obtain adsorption and diffusion properties by measuring permeation through the membranes. Transient permeation measurements were used to calculate adsorption parameters and membrane thickness. These parameters were further used to determine the diffusion parameters using steady state permeation measurements. A single-site Langmuir isotherm was used for the adsorption and the support was modeled using molecular diffusion. The membrane thickness was stated to be 220 μm and the *n*-butane diffusion coefficients were

found to be an order of magnitude lower than the values obtained by NMR measurements. The method was further extended to include a dual-site Langmuir isotherm but the resultant diffusivities did not show any considerable differences, especially at high temperature. This may be because *n*-butane isotherm can be accurately modeled using a single-site Langmuir isotherm at low pressure and high temperature. Moreover, SEM images for membranes grown with a similar technique [183] show that the continuous zeolite layer is loosely intergrown and has a thickness of 70 μm with the deposited zeolite crystals extending for another 100 μm into the support. Thus, the effective thickness should be < 220 μm and the calculated diffusion coefficients could be an overestimation.

Thus, diffusivities obtained using membrane permeation are 2-3 orders of magnitude than those determined by the experiments.

3.4. Model validation

The real adsorption solution theory and the intersection blocking phenomenon, used to determine the butane isomer mixture adsorption and diffusion parameters respectively, were incorporated in the Maxwell-Stefan model and the resultant partial differential equations were solved in gPROMS [115]. Models for the support layer, sweep gas and concentration polarization were included. The results were obtained for 500 nm thickness zeolite layer and 3 mm thickness support (pore size: 3 μm, porosity: 0.3, and tortuosity: 2.5) by simulating an equimolar feed at total pressure of 1 atm and the permeate side, also set at 1 atm, with Helium as the sweep gas. The steady-state flux and separation factors predicted by the model are also compared to those determined by experiments [31] performed under the same conditions, and shown in **Figure 3.11a and 3.11b**, respectively. Simulation results for zeolite membrane "without support" i.e. neglecting the effect of the support are also shown. The computed separation factors for the membrane (including the zeolite layer and the support) are almost 5-fold lower than the ones calculated for zeolite

membrane “without support”, which suggests that the butane permeation in the model is mostly governed by the (non-selective) transport through the support layer. Significantly lower values of flux for the membrane, as compared to those for zeolite membrane “without support” also suggest the same. On the other hand, the experimental values for the separation factor are nearly equal to the values obtained for the simulated case of zeolite membrane “without support”. Assuming that the simulation prediction for the intrinsic separation factor is correct, this suggests that the permeation in the experiments is mostly governed by the zeolite layer.

The comparison between the experimental and the simulated values indicates that the permeation rate in the real membranes is lower than that predicted by modeling based on the NMR transport data. This discrepancy has also been mentioned in the literature [44,174–182], as discussed in section 4.3. To account for this discrepancy, the corrected diffusivity values for both isomers in the model are decreased, and a reduction by a factor of 50 ($Đ = Đ_0/50$) gives values in good agreement with the experiments (**Figure 3.11a-b**). The agreement is further improved when the effects of concentration polarization are also included.

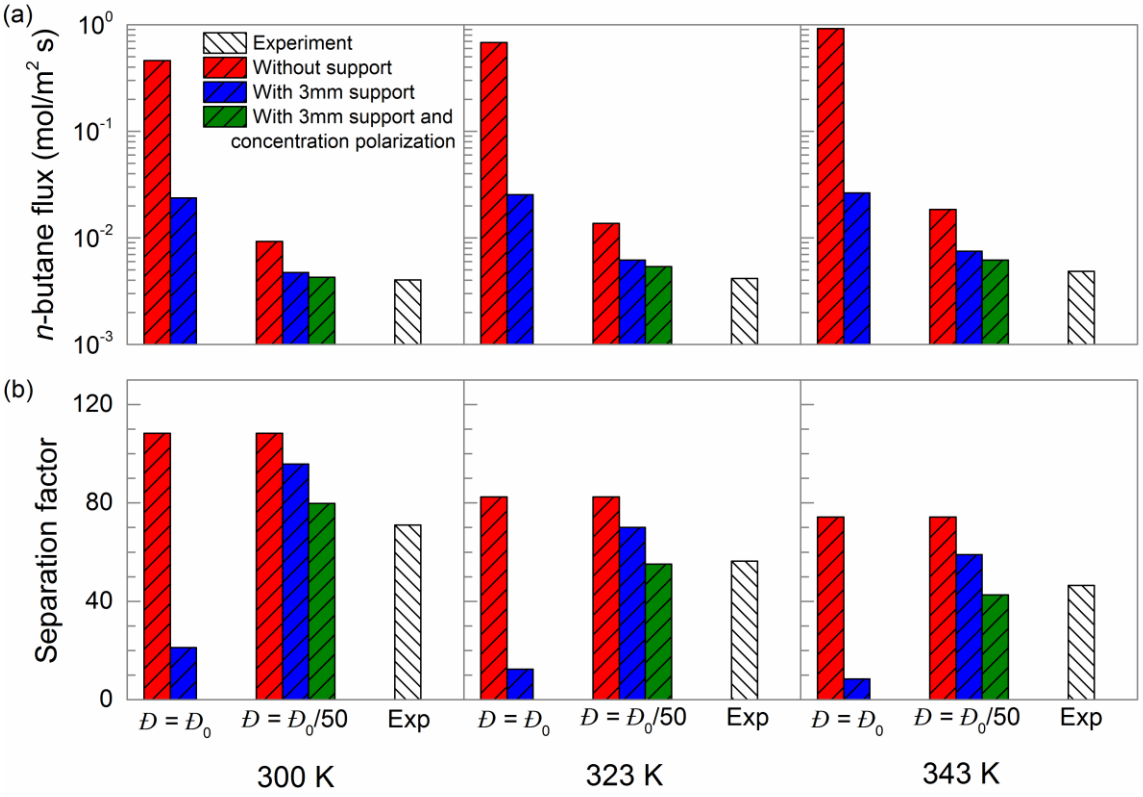

Figure 3.11: Model predictions compared to experimental values (Agrawal et al. [31]) of **(a)** *n*-butane flux **(b)** separation factor.

Feed: equimolar *n*-butane/*i*-butane mixture at a total pressure of 1 atm. Sweep: Helium at 1 atm. Membrane thickness: 500 nm. Support thickness: 3 mm.

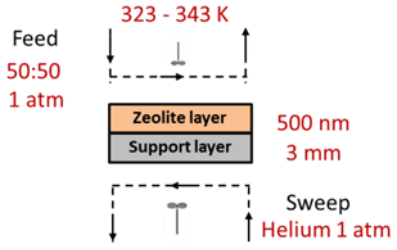

A possible reason for the reduced mobility may be the more rigid structure of zeolite membranes as compared to free standing zeolite crystals which can be more flexible. When the size of the permeating molecule is similar to or slightly larger than the pore size of the crystal, the molecule could still permeate through the pores by expansion of the crystal. However, zeolite membranes grown over a rigid support do not allow the expansion of the membrane pores, and thus the permeation through the rigid membrane is decreased. Jeong et al. [184] have shown that the MFI crystals during the membrane synthesis are under

compressive stress and thus differ from the crystals in MFI powder. They have shown that the crystals in c-oriented membranes are contracted along the a-axis and b-axis (in-plane) and elongated along the c-axis (out-of-plane). Rangnekar et al. [185] have also observed a similar phenomenon with nanosheets. Although other explanations, like pore blockage for a large fraction of the membrane pores could also be responsible for this discrepancy, a reduction in the value of the diffusion coefficients used in the model is adapted here as a reasonable approach. In what follows, the model is further used to analyze the scope of improvement and a process level model is developed and simulated to determine the economic feasibility of membrane separation processes for butane isomer mixtures.

3.5 Scope of improvement

As the diffusivity of butane isomers in the current real (experimentally available) MFI membranes is predicted to be 50-fold lower than the diffusivity values realized in free-standing MFI crystals, there is a considerable scope of improvement in the separation of butane isomers using MFI membranes. Three different cases for improvement in the current values of diffusion coefficients in membranes are analyzed – improvement by a factor of 5 ($Đ = Đ_0/10$), 10 ($Đ = Đ_0/5$) and 50 ($Đ = Đ_0$); where $Đ_0$ refers to the diffusion coefficient in free-standing MFI crystals, which is the largest theoretically achievable value. This 5 to 50-fold improvement could be realized by improving the membrane microstructure to reduce strain in zeolite films and increase the diffusivity in the membrane by up to 50-fold. In practice, the flux increase could be equivalently achieved, by further decreasing the membrane thickness. If pore blocking is responsible for the discrepancy, then its elimination or the corresponding membrane thickness reduction will be required to improve flux.

As the permeance across the membrane increases, the relative contribution of the resistances due to support layer, sweep gas and concentration polarization increases. Thus,

the effect of these factors on the membranes with improved diffusion is analyzed next in order to determine: (i) if and when a thinner support is desirable, (ii) under what conditions one should use the sweep gas, and (iii) to what extent the permeation through zeolite layer can be improved so that the concentration polarization does not become a limiting factor.

3.5.1 Effect of support and sweep gas on membranes with improved performance

Improved permeation through the zeolite layer will increase the relative support resistance which can lead to lower separation factors. Thus, simulations were also carried out with a thinner support layer of 1 mm thickness, which should be still strong enough to hold the zeolite layer. The membrane operation with a Helium sweep was simulated for an equimolar feed at 1 atm and temperature between 300 K and 343 K. A comparison of *n*-butane flux (**Figure 3.12a**) and separation factor (**Figure 3.12b**) obtained for membranes with a 1 mm and a 3 mm thick support with the corresponding values obtained for membrane "without support" suggests that even 1 mm thick support layer provides a significant resistance to the permeation. For a 50-fold improvement in the diffusivity ($Đ = Đ_0$), the permeation is found to be mostly governed by the support layer leading to very low separation factors.

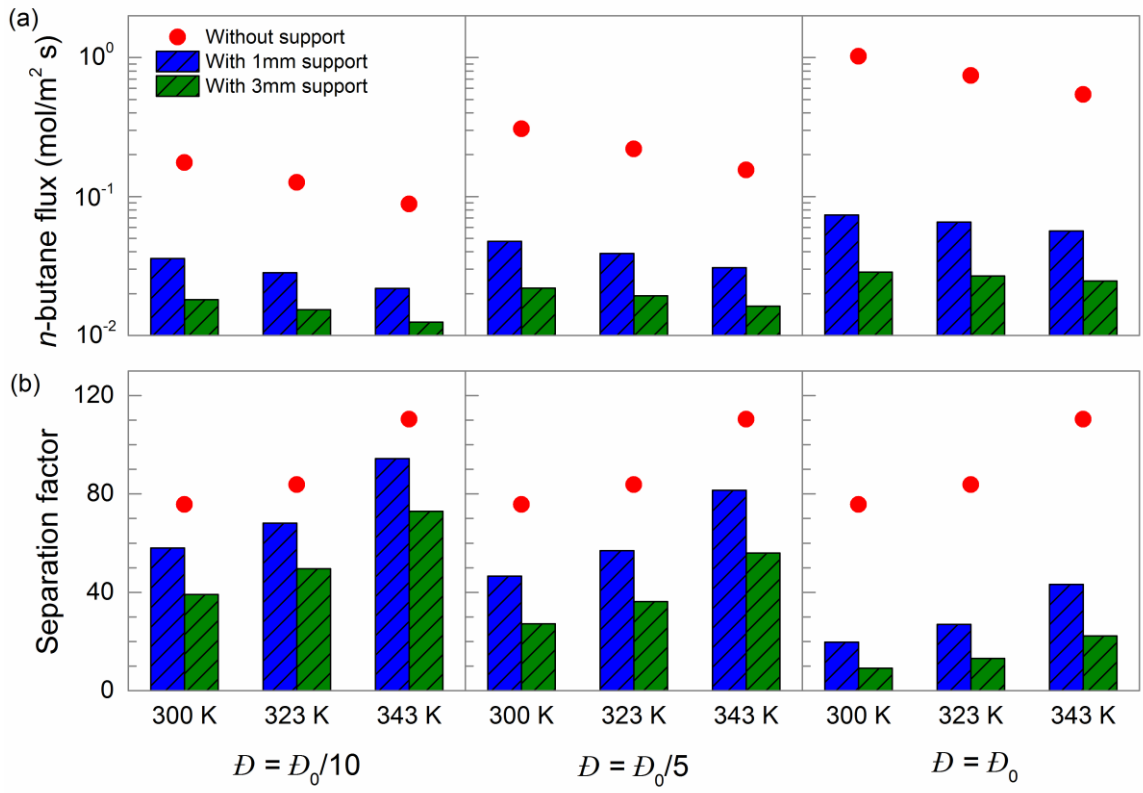

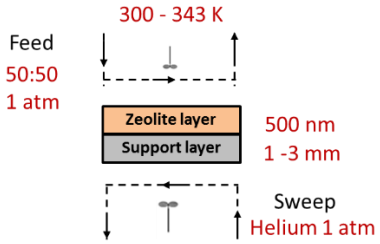

Figure 3.12: Predicted separation performance of membranes with improved performance for various feed temperatures. Values are shown for a 5-fold ($Đ = Đ_0/10$), 10-fold ($Đ = Đ_0/5$) and 50-fold ($Đ = Đ_0$) improvement in diffusivity compared to the value used to model experimentally observed permeance ($Đ = Đ_0/50$) where $Đ_0$ is the diffusivity predicted by theory. **(a)** *n*-butane flux **(b)** separation factor.

Feed: equimolar *n*-butane/*i*-butane mixture at a total pressure of 1 atm. Sweep: Helium at 1 atm. Membrane thickness: 500 nm. Support thickness: 1 mm and 3 mm.

Results are also obtained at higher pressures for a fixed temperature of 343 K and are shown in **Figure 3.13a** and **Figure 3.13b**. Though the separation performance is improved at higher pressure, *n*-butane flux for membranes with a 1 mm thick support is still < 50% of the flux for membrane "without support". Thus, further improvements in the support layer (sub-mm support) are essential to gain maximum benefits out of the improved zeolite layer.

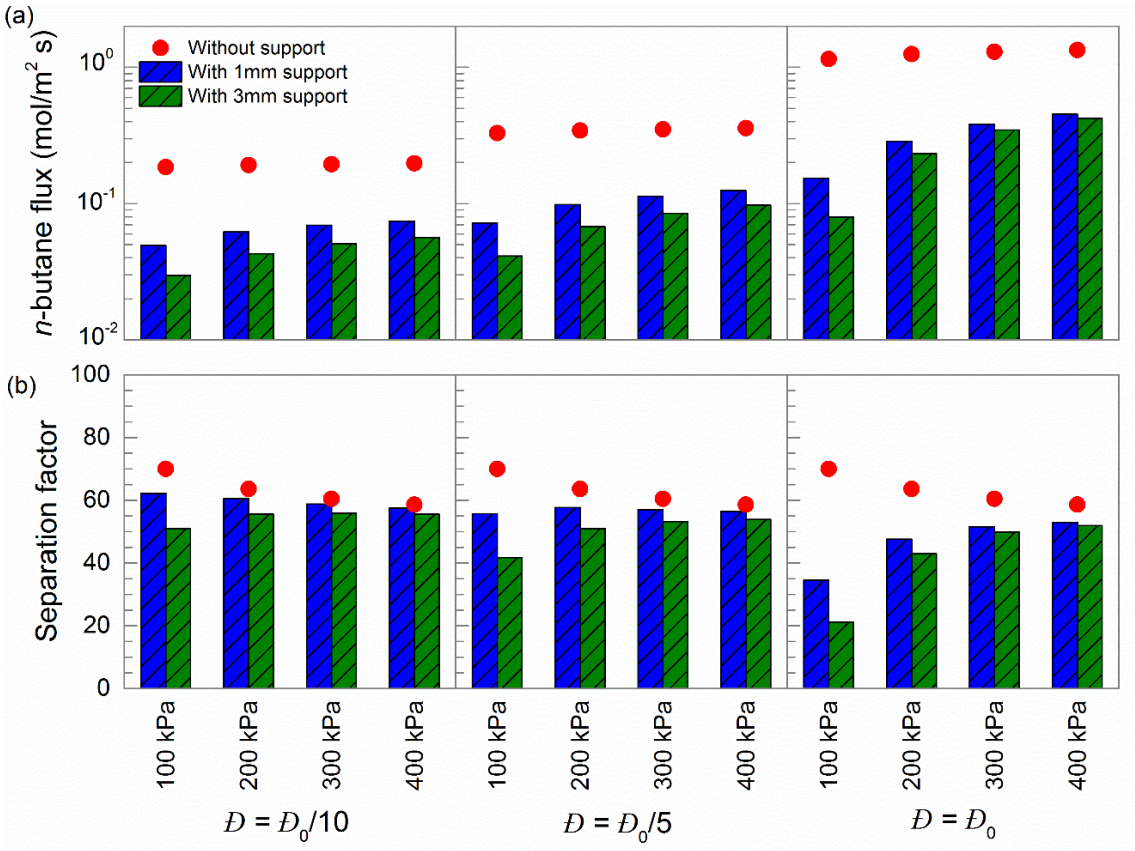

Figure 3.13: Predicted separation performance of membranes with improved performance for various feed partial pressure. Values are shown for a 5-fold ($Đ = Đ_0/10$), 10-fold ($Đ = Đ_0/5$) and 50-fold ($Đ = Đ_0$) improvement in diffusivity compared to the value used to model experimentally observed permeance ($Đ = Đ_0/50$) where $Đ_0$ is the diffusivity predicted by theory. **(a)** *n*-butane flux **(b)** separation factor.

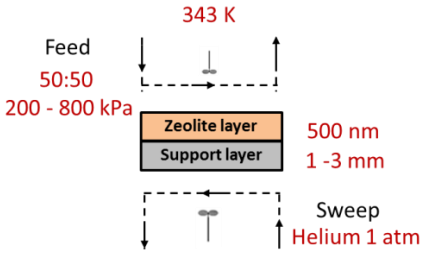

Feed: equimolar *n*-butane/*i*-butane mixture at T = 343 K. Sweep: Helium at 1 atm. Membrane thickness: 500 nm. Support thickness: 1 mm and 3 mm.

As the relative support layer resistance for membranes operated without any sweep is less compared to membranes operated with a sweep, membrane permeation without sweep gas was also studied. Since the total pressure of butane isomers on the permeate side, operated without sweep, is 1 atm, only high feed pressures are considered. The *n*-butane flux and separation factors obtained for an equimolar feed at a fixed temperature of 343 K and total feed pressure between 400 kPa and 800 kPa are shown in **Figure 3.14a** and

Figure 3.14b respectively. The values for both 1 mm and 3 mm thick support membranes are almost equal to those obtained for membrane "without support", which suggests that the permeation is totally governed by the zeolite layer. Thus, when operated without any sweep, even 3 mm thick support membranes can realize the full potential of the improved zeolite layer.

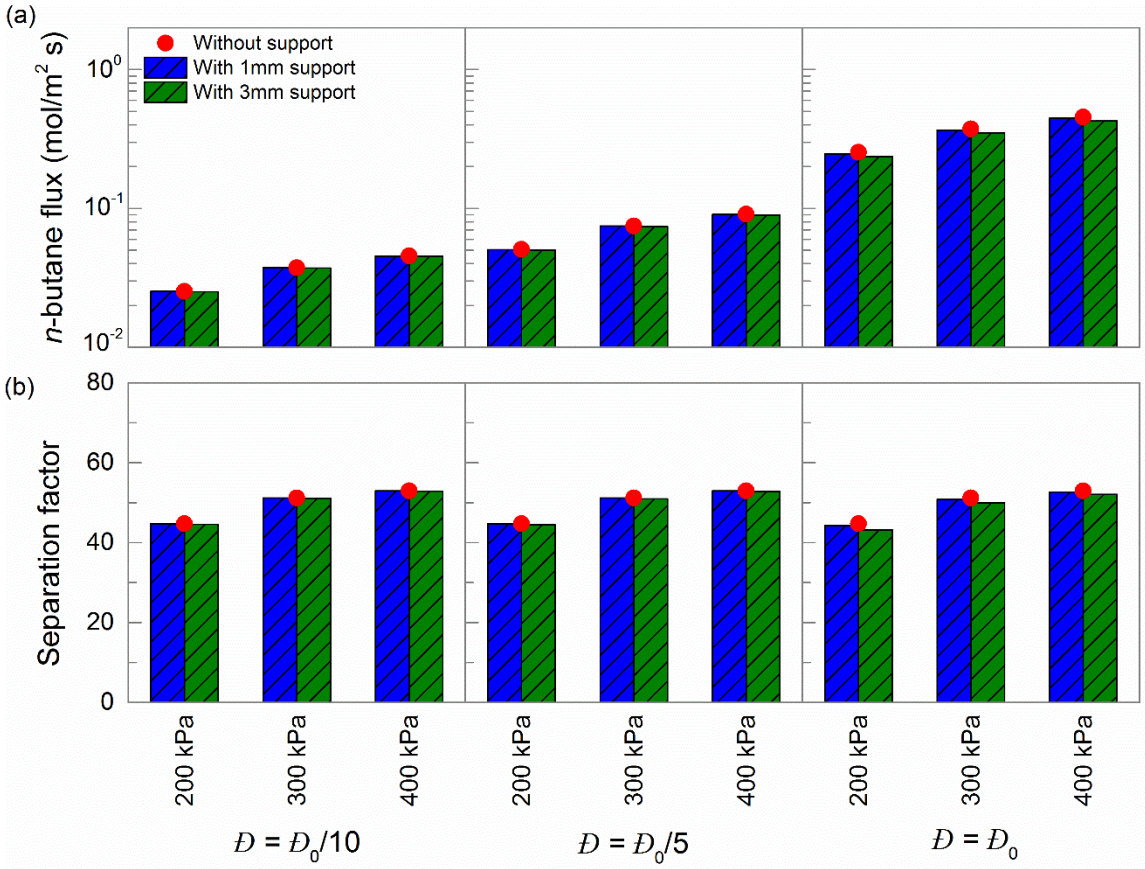

Figure 3.14: Predicted separation performance of membranes with improved performance for various feed partial pressure. Values are shown for a 5-fold (Đ = Đ$_0$/10), 10-fold (Đ = Đ$_0$/5) and 50-fold (Đ = Đ$_0$) improvement in diffusivity compared to the value used to model experimentally observed permeance (Đ = Đ$_0$/50) where Đ$_0$ is the diffusivity predicted by theory. **(a)** *n*-butane flux **(b)** separation factor.

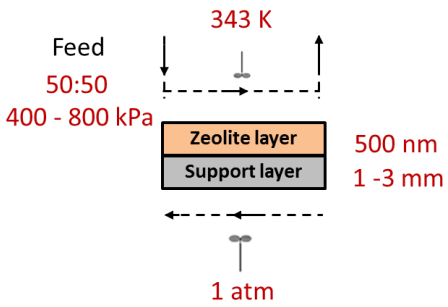

Feed: equimolar *n*-butane/*i*-butane mixture at T = 343 K. Permeate: 1 atm without any sweep. Membrane thickness: 500 nm. Support thickness: 1 mm and 3 mm.

As the absence of sweep gas has an adverse effect on separation performance, *n*-butane flux and separation factors obtained for membranes operated with sweep and without sweep for a fixed support thickness of 3 mm are compared in **Figure 3.15a-b**. The results indicate that, especially at higher pressure, there is only a marginal increase in the values when the sweep is introduced. Moreover, if the sweep gas is used, subsequent purification steps are required to separate *n*-butane from sweep gas itself. Thus, for process design studies, support thickness of 3 mm is used and membrane operation is considered without sweep.

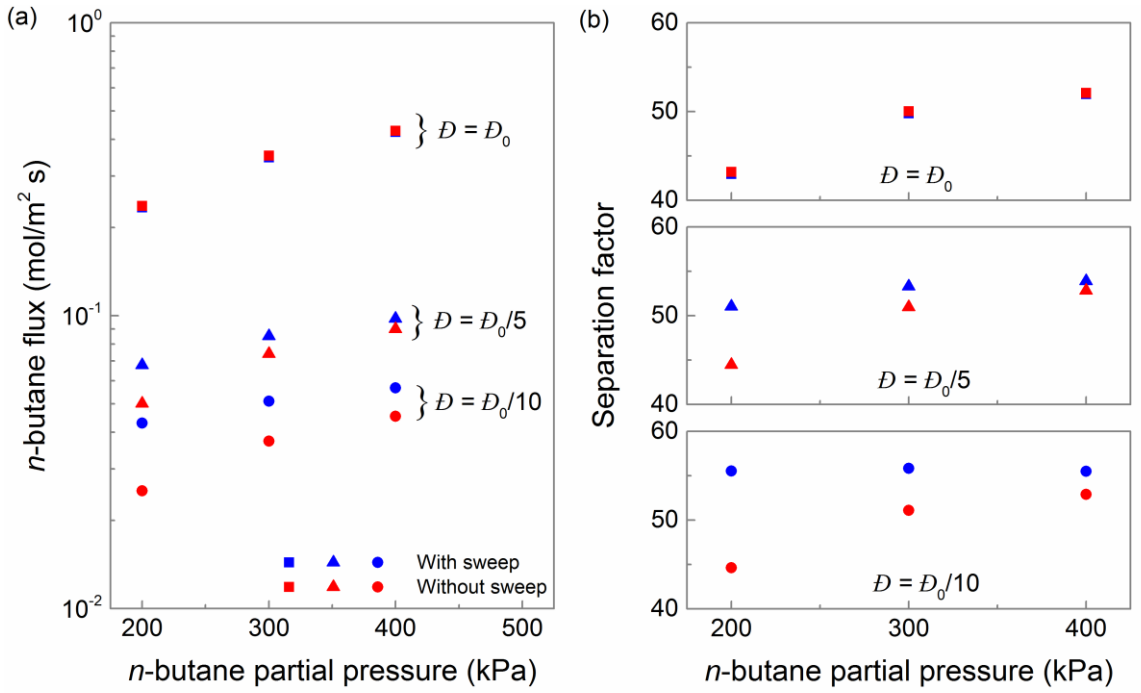

Figure 3.15: Effect of sweep gas on permeation through membranes with improved performance**.** Values are shown for a 5-fold ($Đ = Đ_0/10$), 10-fold ($Đ = Đ_0/5$) and 50-fold ($Đ = Đ_0$) improvement in diffusivity compared to the value used to model experimentally observed permeance ($Đ = Đ_0/50$) where $Đ_0$ is the diffusivity predicted by theory. **(a)** *n*-butane flux **(b)** separation factor.
Feed: equimolar *n*-butane/*i*-butane mixture at a T = 343 K. Sweep (when present): Helium at 1 atm. Membrane thickness: 500 nm. Support thickness: 3 mm.

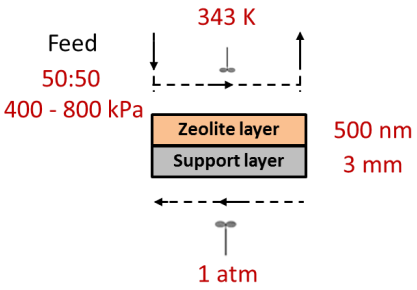

3.5.2 Effect of concentration polarization on membranes with improved performance

The improved membrane permeability will also enhance the contribution from concentration polarization. As stated earlier, concentration polarization depends on the membrane permeability, membrane enrichment and the external mass transfer coefficient. The membrane permeability and enrichment are determined by solving the transport equations (Maxwell-Stefan model) through the membrane. The mass transfer coefficient is directly proportional to the Sherwood number and inversely proportional to the characteristic thickness of the boundary layer. While the Sherwood number depends on the module geometry and flow conditions, the characteristic thickness depends only on the geometry. The three most common geometries are selected here: circular tube, annulus and tube bundles (**Figure 3.16**). For all three geometries, the characteristic thickness is equal to the hydraulic diameter, and the Sherwood number for laminar and turbulent flow regime is obtained from the literature [104,105].

For a laminar flow inside a circular tube, the Sherwood number varies between 3.57 and 4.36 for varying boundary conditions and thus an average value of 4 is chosen in this study. Since the mass transfer coefficient is inversely proportional to the tube diameter, a thinner tube is more attractive. However, sub-mm radius tubes are difficult to fabricate for a 3 mm thick hollow fiber so results are obtained for 1 mm radius tube (i.e. tube diameter equal to 2 mm). For laminar flow in an annulus (shell side of a circular tube) with a fixed inner dimension, both the Sherwood number and the hydraulic diameter increase with increasing outer dimension, indicating a trade-off. For a fixed inner diameter of 8 mm (2 mm diameter tube + 3 mm thick hollow fiber on each side), Sh~10 can be obtained for a hydraulic diameter of 6 mm. For flow on shell side in a tube bundle, widely spaced tubes increases the Sherwood number but it also increases the hydraulic diameter. Similar to flow in an annulus, a Sh~10 can be obtained for a hydraulic diameter of 6 mm. For turbulent

flow, Sherwood number, as high as, 40 can be obtained for all geometries but turbulent flow is difficult to achieve in small diameter tubes. The transition from laminar to turbulent flow starts at a Reynolds number (*Re*) of 2300 while the Re that can be achieved for butane isomer gaseous mixture at 800 kPa and 343 K flowing at 10 cm/s in a 6 mm diameter tube is 1500. Thus, turbulence or mixing can only be achieved via external factors such as introducing secondary flow through curved geometries [186], using baffled membrane modules [187], creating fluid instabilities by placing protuberance and inserts in the tube or superimposing flow pulsations[187]. However, this will lead to larger pressure drop along the membrane. The Sherwood numbers for annulus and tube bundles are nearly equal.

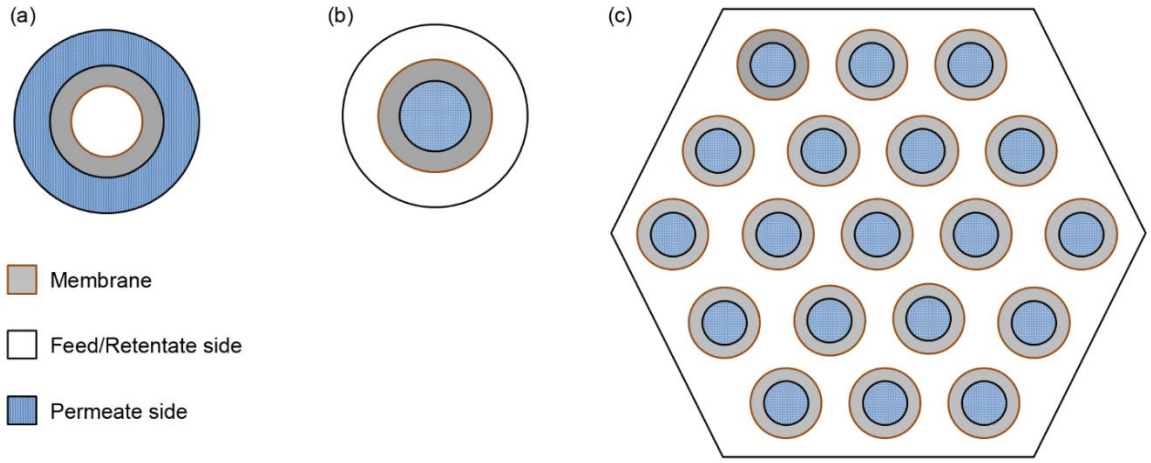

Figure 3.16: Cross-section of various geometries **(a)** flow in a circular tube **(b)** flow in a concentric annulus, and **(c)** flow on the outer surface of tube bundles.

The effect of concentration polarization on the separation performance of membranes with improved performance is shown in **Figure 3.17a-b.** While the *n*-butane flux and separation factors for a 5-fold ($Đ = Đ_0/10$) and a 10-fold ($Đ = Đ_0/5$) improvement in diffusivity from the currently achieved performance experimentally ($Đ = Đ_0/50$) are less affected, the corresponding values for a 50-fold ($Đ = Đ_0$) improvement in diffusivity are significantly lower when concentration polarization is taken into account. Thus, a 10-fold

improvement in the diffusivity (with respect to the diffusivity that fits the currently available experimental data) is a reasonable upper limit. Even if one achieves a higher permeation by either improving transport (increasing diffusivity) in the zeolite layer or, equivalently, by reducing membrane thickness, external resistances will start to dominate and the performance will deteriorate accordingly.

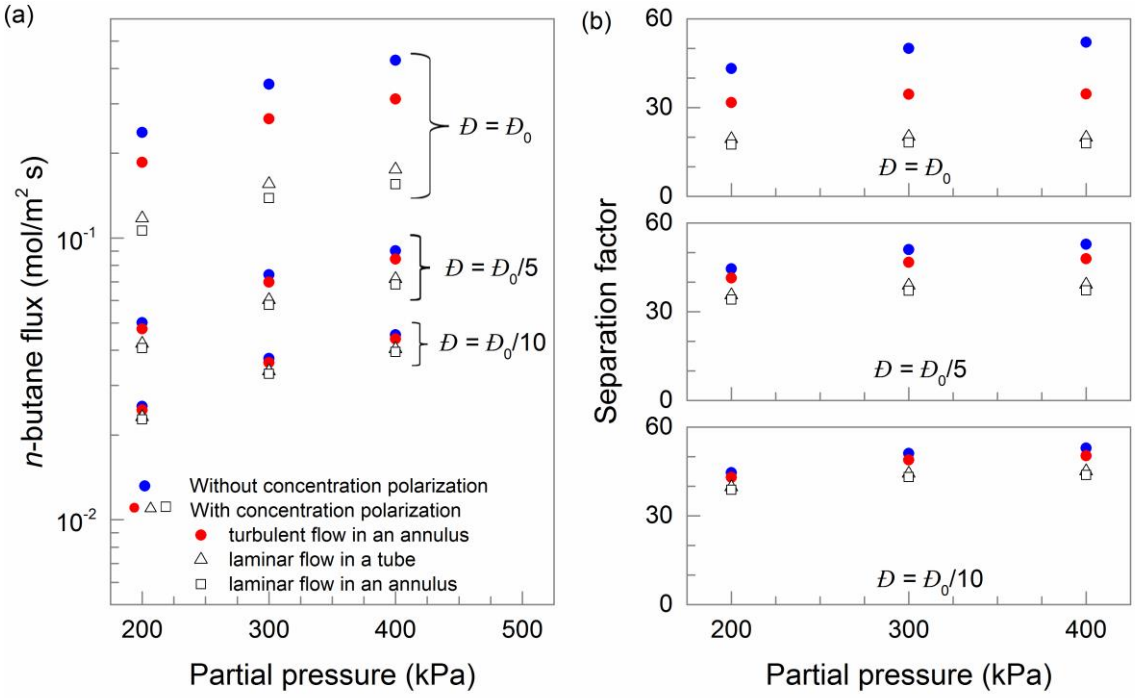

Figure 3.17: Effect of concentration polarization on permeation through membranes with improved performance**.** Values are shown for a 5-fold ($Đ = Đ_0/10$), 10-fold ($Đ = Đ_0/5$) and 50-fold ($Đ = Đ_0$) improvement in diffusivity compared to the value used to model experimentally observed permeance ($Đ = Đ_0/50$) where $Đ_0$ is the diffusivity predicted by theory. **(a)** *n*-butane flux **(b)** separation factor.
Feed: equimolar *n*-butane/*i*-butane mixture at a T = 343 K. Membrane thickness: 500 nm. Support thickness: 3 mm.

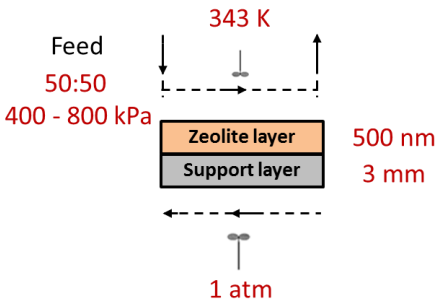

3.6 Process design

Both the stand-alone membrane processes and the hybrid membrane/distillation processes are considered to analyze the industrial feasibility of MFI membranes for butane isomer separation. To evaluate the benefits of using these membrane-based designs, a distillation technology was selected as the base case, and is discussed next.

3.6.1 Base Case

Industrial separation of butane isomers is currently accomplished using distillation. The feed conditions and the separation performance obtained from the literature [188] are summarized in **Table 3.2**. A distillation column for the same performance was also simulated in Aspen Plus. The reboiler and condenser duty of the simulated model are almost the same as those of the industrial column but the number of trays in the simulated model was found to be 90 as opposed to 74 trays in the industrial column. A similar discrepancy has also been reported earlier [188], and thus an overall column efficiency of 122 % was used to simulate the industrial performance.

Table 3.2. Feed conditions and separation performance of distillation for butane isomer separation

Pressure	8.81 atm
Temperature	343 K
Flowrate	121.8 mol/s
n-butane wt %	69.6 %
Recovery	98.8 %
Purity	99.7 %

The column size data and the reboiler and condenser duties were used to estimate the capital and the annual operating costs of the column, respectively, and are shown in **Table 3.3** [189,190]. Although the reboiler duty and the condenser duty are of the same magnitude, the reboiler makes up for the majority of the operating costs due to the

requirement of expensive steam as compared to low cost cooling water required for the condenser.

Table 3.3. Capital and annual operating cost of distillation column for butane isomer separation

Column height	51.8 m
Column diameter	2.9 m
Total number of trays	74
Feed tray location	37
Capital Cost (CAPEX)	2.59 MM$
Cooling duty	11.09 MW
Heating duty	10.72 MW
Operating Cost (OPEX)	2.25 MM$
Total Cost (OPEX + CAPEX)	**4.84 MM$**

(MM$ = 10^6 $)

The feed location of the distillation column was also optimized to minimize the reboiler duty for the same separation performance and same number of trays. The reboiler duty and the condenser duty for the optimized base case is found to be 1.13 MW and 1.14 MW lower respectively. This reduces the operational cost from 2.25 MM$/year to 2.01 MM$/year.

3.6.2 Single stage membrane process

A tubular membrane design (single tube cartridge or tubes packed together in small bundle) is considered, and a schematic of a single circular tube with feed on the shell side is shown in **Figure 3.18a.** A single-stage membrane unit (**Figure 3.18b**) is investigated initially as an alternative to distillation. For a target recovery of 98.8%, the purity is found to be 97% which is less than the target value of 99.7%. Membrane operation with lower pressures on the permeate side (pervaporation) was also examined. As discussed in the Supporting Information S6, pressures below 10 kPa do not appear practical for industrial implementation of butane isomer separation due to excessive cooling requirements.

Simulations performed with a total permeate pressure of 10 kPa suggest that purity increases only marginally to 97.6%, which is still below the required target of 99.7%. Thus, a multi-stage membrane unit is required to improve the product purity.

3.6.3 Multistage membrane process

A schematic of the two-stage membrane unit considered is shown in **Figure 3.18c**; the design consists of two membrane stages operated in series with permeate from the first stage being fed to the second stage. An inter-stage compressor is also used to increase the pressure of the feed to the second stage. The total recovery is the product of the recovery of the two stages. Since the feed to the second stage is more enriched in *n*-butane as compared to the feed to the first stage, the driving force for *n*-butane permeation is greater in the second stage. Thus, a higher recovery is selected for the second stage i.e. 99.8 % which sets a first stage recovery of 99% in order to achieve the target total recovery of 98.8 %. The area required for the current membranes ($Đ = Đ_0/50$) and product purity obtained for different compressor discharge pressure are shown in **Table 3.4**.

Table 3.4. Membrane area and product purity for two-stage membrane system

Compressor Output	Stage #1 Area (m^2)	Stage #1 Purity (%)	Stage #2 Area (m^2)	Stage #2 Purity (%)	Total Area (m^2)
2 atm	16,697	96.89	25,070	99.34	41,767
5 atm	16,697	96.89	10,970	99.59	27,667
8 atm	16,697	96.89	8,812	99.57	25,509

There are only marginal savings in membrane area for compressor discharge pressure over 5 atm. This is because the adsorption isotherm reaches saturation and increasing pressure further does not improve the flux through the membrane. The results also show that a significantly large membrane area is required to match the performance of the distillation unit. Even for a 10-fold improvement in diffusivity ($Đ = Đ_0/5$), the area required is found to be ~3,000 m^2. In comparison, the largest zeolite membrane facility

(implemented for *i*-propanol dehydration at Jiangsu Chemical Co. Ltd in 2012 by Dalian Institute of Chemical Physics) utilizes an area of only 350 m^2 [2].

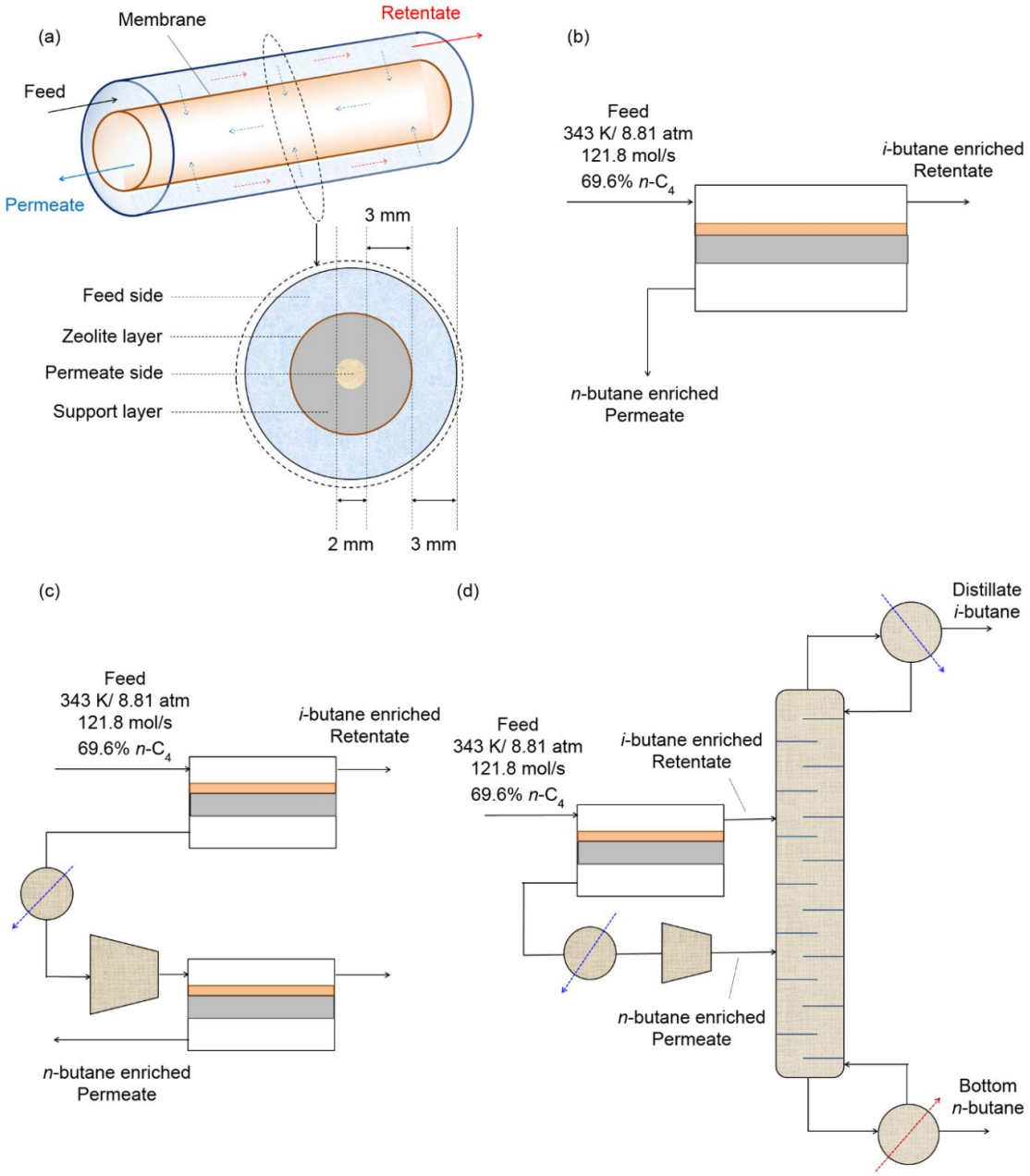

Figure 3.18: Schematic of **(a)** a tubular membrane, **(b)** a single stage membrane unit, **(c)** a two stage membrane unit, and **(d)** a series hybrid membrane distillation unit for butane isomer separation.

The area requirement can be reduced by lowering the pressure on the permeate side. Simulations foe a total permeate pressure of 10 kPa suggest a 3-fold decrease (from ~3,000 m^2 to ~1,000 m^2) in the required membrane area. However, the profits gained form the reduced area should be considered in conjunction with the increased costs associated with the use of vacuum. A preliminary analysis suggests that pervaporation is beneficial only if the membrane cost is more than \$3,000/m^2. Additionally, complete replacement of the columns in operation will be not only technically challenging, but also economically unfavorable because of the long life of the existing depreciated capital infrastructure. For these reasons, a hybrid membrane/distillation process is examined next.

3.6.4 Hybrid membrane/distillation process

A series hybrid configuration is considered. The membrane area and the reboiler and condenser duties required for various values of φ are shown in **Figure 3.19a and 3.19b,** respectively. A membrane with a 10-fold improvement in permeation ($Đ = Đ_0/5$) compared to the value used to model experimentally observed permeance ($Đ = Đ_0/50$), where $Đ_0$ is the diffusivity predicted by theory, was used to calculate the required area. For $\varphi = 0.4$, the reboiler duty is almost half of the stand-alone distillation column and the membrane area (~300 m^2) is almost one-tenth of the stand-alone membrane process, and is comparable to that used in the existing zeolite membranes in industry (~350 m^2). An NPV (net present value) analysis was also carried out to determine NPV savings projections over base-case distillation. A discount rate of 7% per annum was assumed. Furthermore, the membrane was assumed to have a lifetime of 5 years and to cost 50% of the initial investment when replaced. The capital and operating expenses for the additional heat exchangers and compressors were also included in the analysis. The NPV savings calculated with 10-fold improved permeation membranes ($Đ = Đ_0/5$) for different values of φ (0.2 – 0.8) at a fixed membrane cost of \$1000/m^2, and for membrane cost in the range of \$1000/m^2 - \$5000/m^2,

which is a rough estimate of cost of a zeolite membrane [5], at a fixed φ = 0.4 are shown in **Figure 3.20a** and **3.20b,** respectively. For φ = 0.4, a payback period of ~3 years can be achieved with installed membrane cost of up to \$5,000/m^2. Simulations were also performed for pervaporation with a total permeate pressure of 10 kPa. A preliminary analysis suggests that for a similar payback period, pervaporation is beneficial only if the membrane cost is more than \$5,000/m^2.

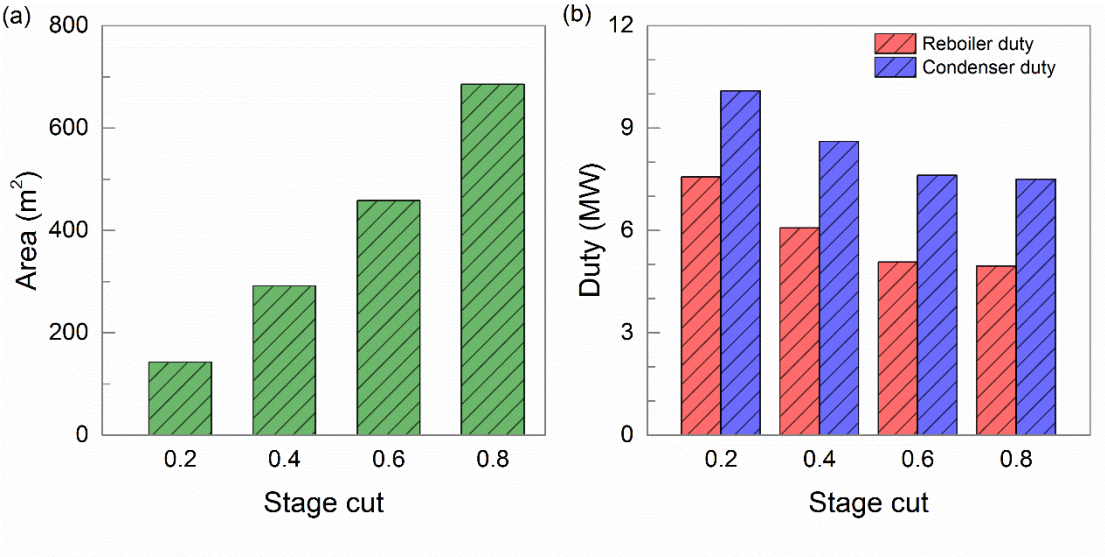

Figure 3.19: (a) The membrane area required for a hybrid membrane distillation unit calculated with a 10-fold improvement in diffusivity ($Đ = Đ_0/5$) compared to the value used to model experimentally observed permeance ($Đ = Đ_0/50$) where $Đ_0$ is the diffusivity predicted by theory. For reference, the area required for a two-stage membrane unit is ~2,500 m^2. **(b)** The corresponding reboiler and condenser duties for the hybrid membrane distillation unit. For reference, the reference reboiler and condensed duty for current distillation technique is 10.72 MW and 11.09 MW respectively.

The hybrid case was also analyzed for the current membrane performance. For φ = 0.4, the required membrane area is calculated to be ~3,000 m^2, which is 10-fold than the corresponding area required for the improved permeation membranes. This large area requirement brings down the NPV savings, and membrane cost as low as \$500/m^2 is needed to achieve a payback period of < 3 years. To reduce the area requirement, a preliminary analysis was also carried out with a pervaporation system (permeate pressure of 10 kPa).

Although, pervaporation leads to a ~3 fold decrease (from ~3,000 m^2 to ~1,000 m^2) in the required membrane area, it was found to be profitable only if the membrane cost is more than \$500/m^2.

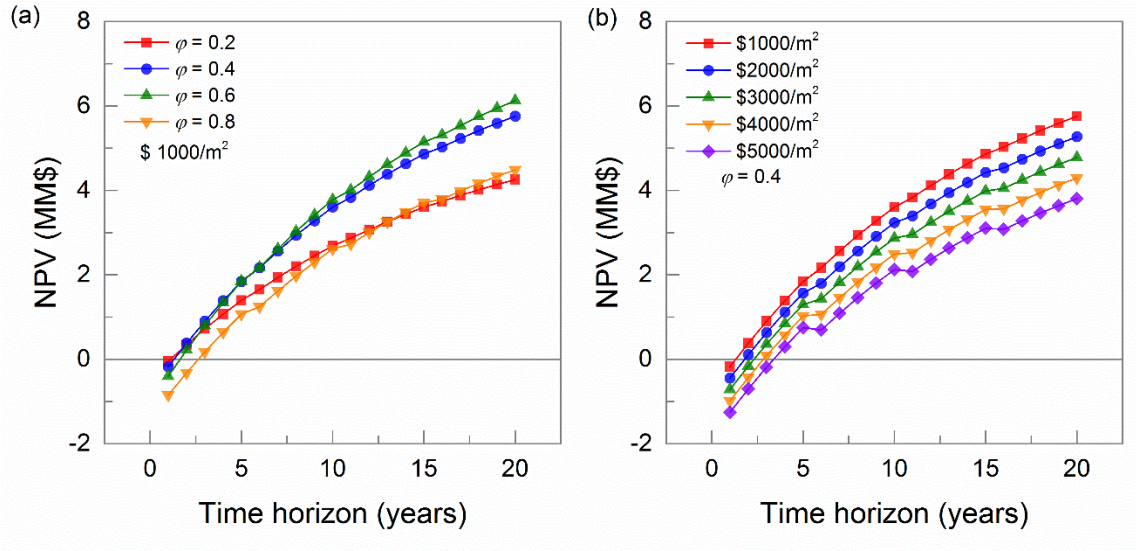

Figure 3.20: NPV savings projection of a series hybrid membrane-distillation system over current distillation technique for a fixed **(a)** membrane cost = \$ 5000/m^2, and **(b)** stage cut (φ) = 0.4, calculated with a 10-fold improvement in diffusivity ($Đ = Đ_0/5$) compared to the value used to model experimentally observed permeance ($Đ = Đ_0/50$) where $Đ_0$ is the diffusivity predicted by theory. (MM\$ = 10^6 \$)

The current membrane technology, thus, is not adequate for attractive performance in butane isomers separation due to the requirement of large area and/or low cost. However, a 10-fold improvement in permeation through these membranes brings down the required membrane area comparable to that used in currently operating zeolite membrane plants [2]. Accordingly, the incurred cost can be as high as \$5,000/m^2 which is also a reasonable estimate of the cost of zeolite membranes [13]. This 10-fold improvement in permeation which can be achieved by either improving membrane microstructure and/or by reducing membrane thickness makes these membranes very attractive from an industrial perspective.

3.7 Conclusion

A detailed adsorption-diffusion model of a zeolite membrane process was developed and applied for butane isomer separation. The effects of the support layer, sweep gas and concentration polarization were also included. The comparison of steady state flux and separation factors predicted by the model with the experimentally determined quantities suggests a discrepancy between diffusion in zeolite membranes and diffusion in zeolite crystals. We found that in order to obtain the experimentally observed permeance and separation factor by simulation, we have to decrease the butane diffusivity in MFI crystals by a factor of 50 ($Đ = Đ_0/50$). The scope of improvement in the performance of current membranes was explored by 5-fold ($Đ = Đ_0/10$), 10-fold ($Đ = Đ_0/5$) and 50-fold ($Đ = Đ_0$) improvement in diffusivity observed in current membranes ($Đ = Đ_0/50$). The results indicate that for up to a 10-fold improvement in diffusivity through the membrane, gains in membrane performance can be attained; for larger diffusivities, concentration polarization effects become significant and further improvement in membrane performance is not possible. We envision that this 10-fold improvement in diffusivity ($Đ = Đ_0/5$) can be achieved by reducing pore blockages in the intergrown membranes or, equivalently, its effect on performance can be achieved by reducing the membrane thickness from the currently achieved ~500 nm to 50 nm or less.

Process simulations based on the detailed model for permeation through the membrane combined with a plug flow model along the length of the membrane, were also performed. Promising design options were determined to carry out butane isomer separation at industrial scale and compared to the current distillation technique. A single-stage membrane process was found to be inadequate as the purity is ~2% lower as compared to the one achieved by distillation. A two stage membrane process, although matches the distillation performance, requires prohibitively large membrane area. Moreover, replacing

distillation completely by membranes does not leverage the existing capital infrastructure. Therefore, a hybrid membrane-distillation process, which exploits the advantages of both processes was examined and found to be energy efficient and economically attractive. A series hybrid process, which is expected to be easy to retrofit and control, was proposed for this separation. With a 10-fold improvement in permeance as compared to that in current state-of-the-art ceramic supported MFI membranes, payback period of 3 years can be achieved with installed membrane cost of up to $5,000/m^2. Alternatively, the same payback period can be achieved by the current technology if manufacturing improvements bring the membrane cost down to $500/m^2.

Chapter 4: Bioethanol enrichment using hydrophilic and hydrophobic membranes

4.1 Introduction

Ethanol, derived from lignocellulosic biomass, is considered a promising renewable fuel [191–193]. The biochemical conversion of biomass to fuel-grade ethanol (99.5 wt. %) requires several steps, namely, pretreatment, hydrolysis, fermentation and dehydration [194,195]. Among these steps, the dehydration consumes more than half of the energy and contributes correspondingly to the operating cost of the entire process, thereby reducing the environmental and economic benefits of bioethanol as a fuel [196–198]. Thus, various energy-efficient separation alternatives have been developed for sustainable production of bioethanol [199–201].

Zeolite membrane separation has also been proposed as a possible solution [202–204]. Hydrophilic zeolite membranes (e.g., zeolite NaA membranes) have been developed and commercialized for dehydrating streams near the azeotropic concentration [205,206]. On the other hand, hydrophobic zeolite membranes (e.g., all-silica MFI membranes), which have a greater affinity towards ethanol, have been considered for the enrichment of dilute ethanol feed [18,26,207]. To date, only hydrophilic zeolite membranes have been implemented in industry for obtaining fuel-grade ethanol from mixtures near the azeotropic concentration [13]. The primary reason for commercialization of hydrophilic membranes is their higher flux (~ 10-fold) and separation factor (~ 100-fold) compared to those obtained for hydrophobic membranes [23]. The higher flux is attributed to the selective permeation of faster-moving water molecules in hydrophilic membranes as compared to the selective permeation of slower moving ethanol molecules in hydrophobic membranes. The lower separation factor for hydrophobic membranes is attributed to the unavoidable

water co-adsorption due to hydrogen-bonding effects (*i.e.*, water is brought in by adsorbed ethanol molecules) [52,208] and due to favorable interaction of water molecules with hydrophilic silanol defects [109,209].

4.2 Model for hydrophilic zeolite membrane

It has been shown that the hydrophilic zeolite membranes can be modeled using ideal theories and, thus, permeation can be characterized by almost constant permeance as observed both at lab-scale and industrial-scale experiments for a large range of operating conditions [210,211]. The hydrophilic membrane is operated in vapor permeation mode and is modeled using a constant permeance model:

$$J_{\mathrm{i}} = \Pi_i \left(p_{i,ret} - p_{i,perm} \right) \tag{4.1}$$

where J is the flux through the membrane, p is the partial pressure, Π is the permeance and 'ret' and 'perm' denote the retentate and the permeate side, respectively.

As the hydrophilic membranes are currently used over azeotropic concentration, most of the experimental data is available at a feed concentration of 10 wt. % water. At 75 °C and 10 wt. % water, commercial hydrophilic membranes have exhibited a flux of 5-10 kg/m^2-hr (permeance of 4.5-9 x 10^{-6} mol/m^2-sec) with separation factor > 10,000 (selectivity of ~ 11,700) [14,206]. In other lab-scale experimental studies, while the permeance has been shown to be almost constant with increasing water content, the selectivity increased with the water content in the feed [210]. Usually, the hydrophilic membranes are operated in vapor permeation mode with feed at high temperature and pressure. Under these conditions, the commercial NaA zeolite membranes from Bussan Nanotech Research Institute Inc. (Japan) have exhibited a flux of 20 kg/m^2-hr (permeance of 2.54 x 10^{-6} mol/m^2-sec) at 130 °C and total pressure of 550 kPa for 10 wt. % water [212].

Thus, hydrophilic membranes are modeled using a constant water permeance of 2.5 x 10^{-6} mol/m^2-sec and a selectivity of 10,000.

4.3 Model for hydrophobic zeolite membrane

However, due to the presence of strong intermolecular hydrogen-bonding interactions and defects, and the resulting highly non-ideal adsorption and diffusion behavior in hydrophobic membranes, the use of ideal theories based on single-component adsorption and diffusion leads to over-estimation of their separation capability [52,208].

Here, atomistic-level simulations are carried out to obtain a consistent set of mixture adsorption and diffusion properties incorporating the effects of hydrogen bonding. Furthermore, real adsorption solution theory [69] and the Maxwell-Stefan formulation with non-zero correlation effects [43] are used to model the non-ideal interactions and determine permeation through the membrane. The support layer is also included in the model. The effects due to the hydrophilic defects are included using an empirical relation for enhanced water adsorption.

4.4 Molecular simulation methods

The molecular simulations were performed in collaboration with Dr. Peng Bai in Siepmann Research Group in Chemistry at the University of Minnesota.

Ethanol, water, and the sorbate-zeolite interactions are described by the TraPPE-UA [213], TIP4P [214], and TraPPE-zeo [215] force-fields, respectively. This choice of molecular models has been shown to predict both the adsorption and diffusion properties in good agreement with available experimental data [52,208,215].

The solution-phase adsorption of water, ethanol, and their mixtures was calculated using configurational-bias Monte Carlo simulations [216–218] in the NPT-version of the Gibbs ensemble [219]. These simulations used a periodic box containing 12 unit cells of

zeolite MFI and a total of 1100 molecules for the entire system with overall compositions ranging from 64:1 to 1:64 water:ethanol, at T = 323 K and P = 1 atm.

Diffusion coefficients were calculated using molecular dynamics simulations in the canonical ensemble [220,221] (ethanol mole fractions of 0.75, 0.85, and 0.92 for total loadings of 1, 2, 5, and 10 sorbate molecules per unit cell, 12 unit cells of MFI zeolite with fixed framework positions, T = 323 K, and a time constant of T_t = 100 fs for the thermostat) with starting configurations obtained from the above CB-GEMC simulations and initial velocities drawn randomly from the Maxwell-Boltzmann distribution. The linear regions with a unity slope in the logarithmic plots of mean-square displacements versus time were used to extract the Maxwell-Stefan diffusivity via the Einstein relation [222]. The complete details of the CB-GEMC and molecular dynamics simulations can be found in [52,215].

4.5 Adsorption modeling

The single component adsorption for ethanol and water on defect-free and all-silica MFI zeolite shows good agreement with experimental measurements. In particular, water shows negligible adsorption at low pressure with a sudden uptake at ~100 MPa. Studies of water intrusion in other hydrophobic zeolites such as beta, chabazite, and ferrite, have similarly shown that water can adsorb only at high pressure on the order of 100 MPa [223]. However, in other studies, water uptake was observed even below the saturation vapor pressure and full loading is reached at ~0.1 MPa [224,225]. This water uptake at low pressure in supposedly hydrophobic adsorbents, including all-silica MFI zeolite, has been attributed to the hydrophilic defects in real crystal used in experiments [209].

For mixture adsorption, water molecules get co-adsorbed with ethanol molecules through hydrogen bonding. This phenomenon lowers the selectivity values compared to those determined from single component adsorption isotherms. The extensively used Ideal Adsorption Solution Theory (IAST) does not account for these intermolecular interactions,

and thus, fails to interpret the results obtained by molecular simulations [52]. Thus, RAST was used and the activity coefficients based on the Margules equation [61]:

$$\ln \lambda_{\text{water}} = x_{ethanol}^2 \left(A_{21} + 2(A_{12} - A_{21}) x_{water} \right) \tag{4.2}$$

were used, and the associated parameters (A_{21} = -11.84 and A_{12} = 4.80) were obtained by fitting of the molecular simulation results. As ethanol adsorption is largely unaffected by the presence of water molecules, the activity coefficient for ethanol was selected as unity. As shown in **Figure 4.1a**, the RAST model agrees well with the results obtained by molecular simulations and yields mean squared errors for the ethanol and water loadings of 0.08 and 0.03, respectively.

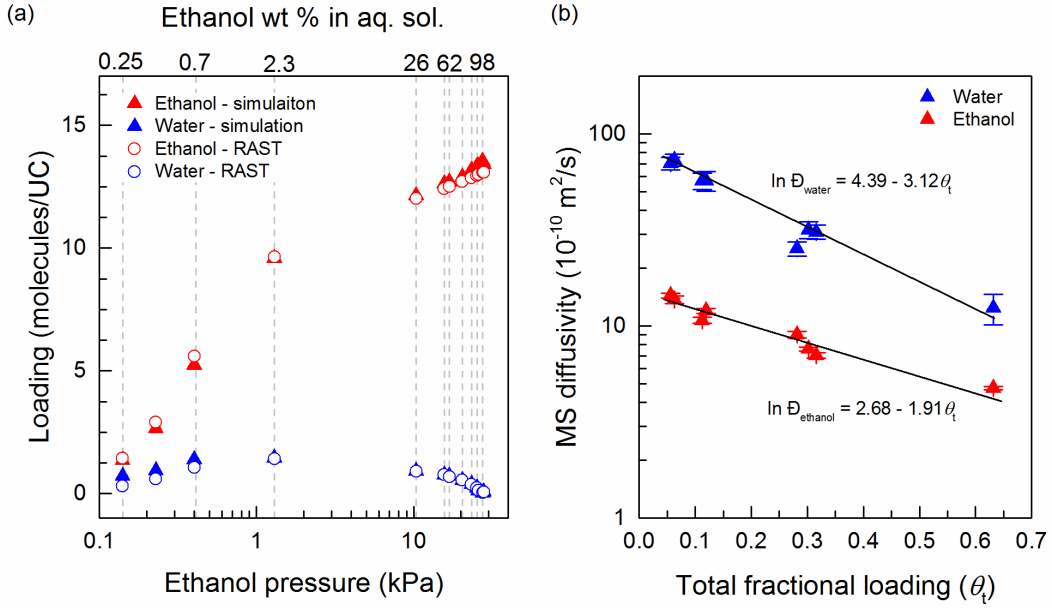

Figure 4.1: (a) Adsorption isotherm as function of ethanol partial pressure (lower axis) obtained using CB-GEMC (Configurational-Bias Monte Carlo - Gibbs Ensemble) simulations and fitted using Real Adsorption Solution Theory for water-ethanol mixture in all-silica MFI zeolite at T = 323 K. The corresponding ethanol wt. % in solution-phase is labelled on the upper axis. The standard error of the mean for the simulation data is smaller than the symbol size. (b) Maxwell-Stefan diffusion coefficients for water-ethanol mixture obtained using molecular dynamics simulations and fitted as a function of total fractional loading in all-silica MFI zeolite at T = 323 K.

4.6 Diffusion modeling

The single component diffusion coefficients of ethanol and water in MFI zeolite has also been extensively studied in the literature [47,84,226–235]. Although it is well-established that the diffusivity of water in MFI zeolite is an order of magnitude higher than that of ethanol, which is attributed to the smaller size of water molecules, the diffusivity values differ by over three orders of magnitude depending upon the techniques used to measure the diffusion coefficient. As shown in **Figure 4.2**, values obtained by molecular simulations and/or microscopic methods (10^{-9}-10^{-10} m^2/s) are 2-4 orders of magnitude higher than those obtained by macroscopic methods (10^{-13}-10^{-14} m^2/s) [23,47,84,230,236].

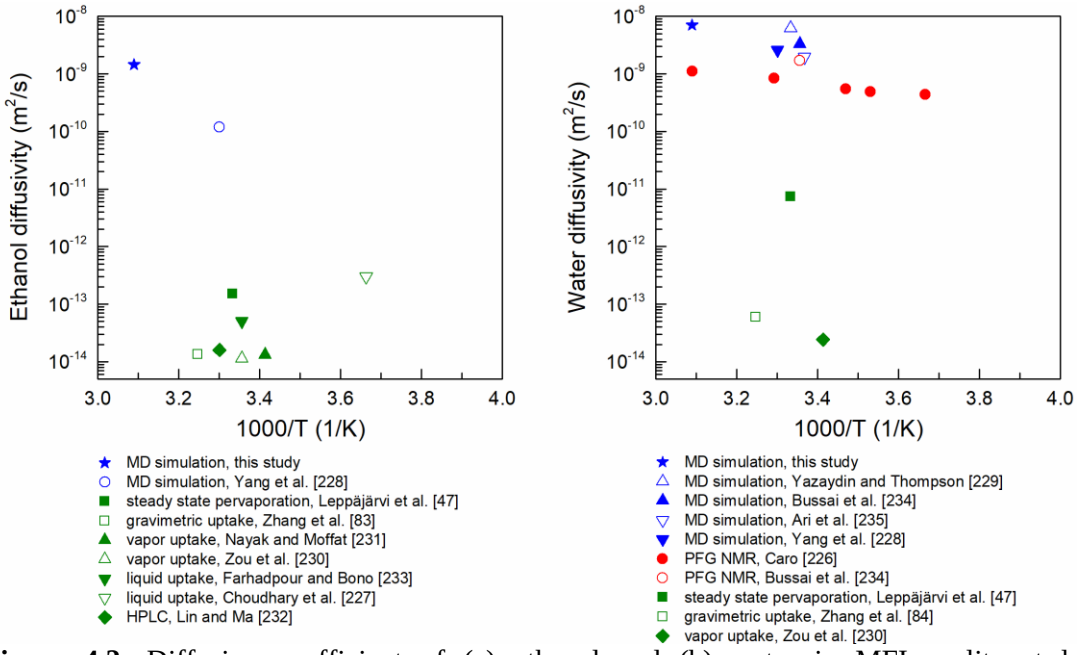

Figure 4.2: Diffusion coefficient of (a) ethanol and (b) water in MFI zeolite at low concentration/infinite dilution obtained by various molecular simulations, microscopic and macroscopic experimental techniques.

In this research, molecular dynamics simulations were used to obtain the mixture diffusion coefficients of water and ethanol for several values of total loading and mole fraction in all-silica MFI zeolite. Note that the adsorbed phase mole fractions do not include $x_{ethanol} < 0.75$, as they are constrained by mixture isotherms and solution-phase concentrations. The mixture diffusion coefficients are shown in **Figure 4.3** and numerical

values are given in **Table 4.1**. The data indicate only a weak dependence on mole fraction (within the statistical uncertainty of the simulation data), but a pronounced dependence on loading and thus, the diffusivities were fitted only as a function of total fractional loading (**Figure 4.1b**). The diffusivities for water exceed those for ethanol by factors ranging from 3 to 5 with the difference decreasing at higher loading. This can be attributed to the reasoning that in a binary mixture the slower moving molecules (ethanol) slow down the faster moving molecules (water) and vice-versa [228,237].

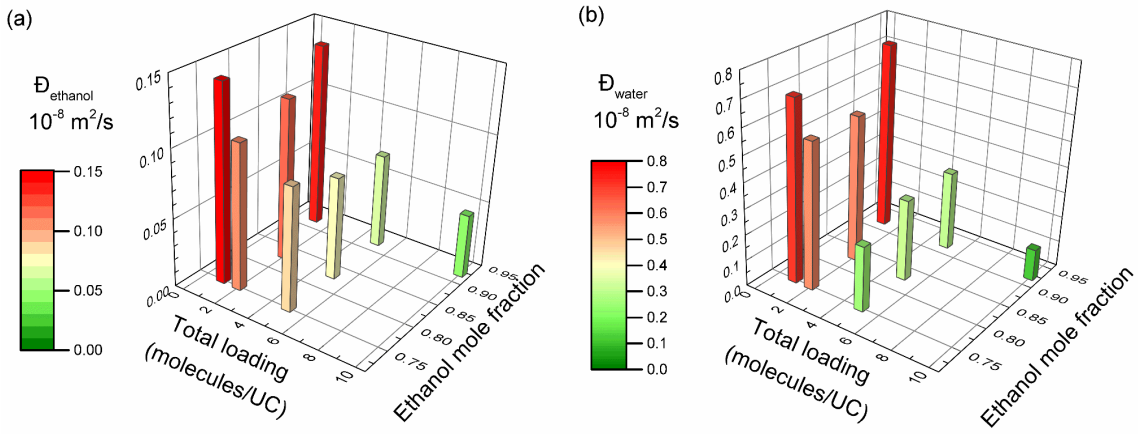

Figure 4.3: Maxwell-Stefan diffusion coefficients for water-ethanol mixture in MFI zeolite obtained using molecular dynamics simulations for various ethanol mole fraction (0.75, 0.85 and 0.92) and total loadings (1, 2, 5 and 10 molecules/UC) in the adsorbed phase at T = 323 K.

Table 4.1. Mixture diffusion coefficients (Maxwell-Stefan obtained using molecular simulations) of water and ethanol in MFI zeolite at T = 323 K for various loading and mole fraction.

No of molecules/12 UC			Total fractional loading	Diffusivity (10^{-8} m^2/s)			
Total	Water	Ethanol		Water	Error	Ethanol	Error
12	3	9	0.06	0.70	0.05	0.144	0.004
12	1	11	0.06	0.73	0.05	0.137	0.006
24	6	18	0.11	0.57	0.06	0.107	0.004
24	4	20	0.12	0.57	0.07	0.120	0.003
60	15	45	0.28	0.25	0.02	0.090	0.004
60	9	51	0.30	0.32	0.03	0.076	0.002
60	5	55	0.32	0.31	0.03	0.070	0.002
120	10	110	0.63	0.12	0.02	0.047	0.001

4.7 Model validation

The multi-component adsorption and diffusion models were incorporated in the Maxwell-Stefan formulation and the resulting model was solved in gPROMS [115]. The thicknesses of the zeolite layer and support layer, i.e. 1.5 μm and 3 mm, respectively, were chosen to be similar to those of MFI membranes for ethanol-water separation reported in [26]. Ethanol permeance and its selectivity over water are shown in **Figures 4.4a** and **4.4b**, respectively. The permeance and selectivity values are selected for validation as opposed to commonly reported flux and separation factor because the permeance and the selectivity mainly reflect the intrinsic properties of the membranes while the flux and separation factor depend on the operating conditions to a larger extent [238].

Ethanol permeance predicted by the model is found to be lower, while the selectivity was found to be higher as compared to those determined in an experiments [26]. To gain insights into this discrepancy, ethanol permeance predicted by the model considering only the support (i.e. neglecting the effect of the MFI zeolite layer) and selectivity considering only the zeolite layer without support (i.e. neglecting the effect of the support) are also shown. These values represent the highest permeance and the highest selectivity, respectively, that can be obtained by the membrane. As shown in **Figure 4.4a-b**, the permeance predicted by the model is almost equal to that obtained by the non-selective support layer. The selectivity (~1) is much less than that obtained by the selective zeolite layer. These results suggest that the zeolite layer in the simulated membrane is more permeable than the real membranes, and thus the overall permeation in the model is governed predominantly by the support layer, thereby resulting in lower selectivity and higher permeation rates as compared to those achieved in the experiment. This discrepancy has also been found in other studies in the literature [239], and is explained with the reasoning that the diffusion coefficients obtained using molecular simulations reflect the

behavior in crystals with ideal pore structure, while the presence of structural non-idealities, compressive stresses, thermodynamic and physical surface barriers in the real membranes results in reduced permeation rates [84,184,185].

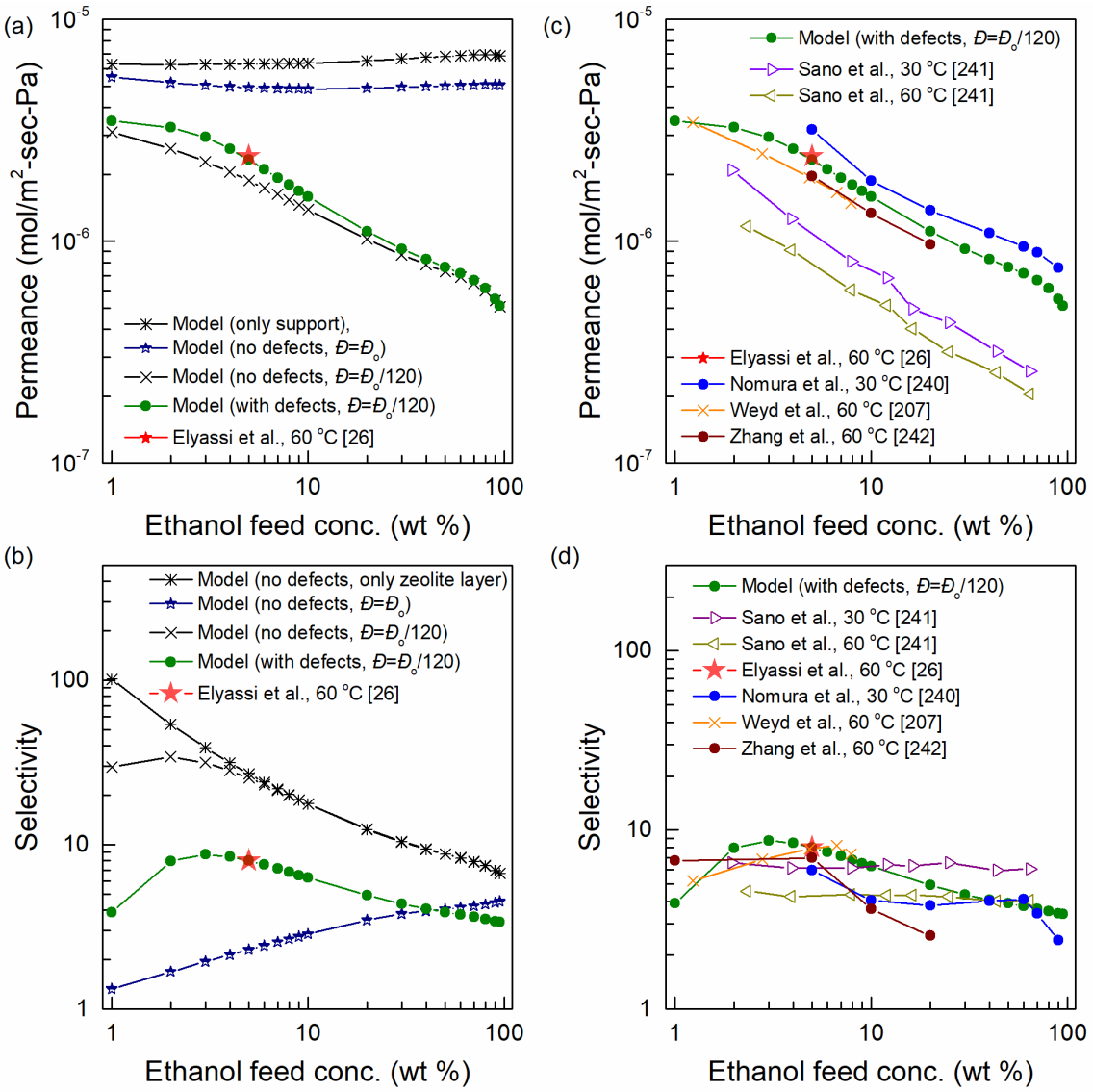

Figure 4.4: **(a)** Steady-state ethanol permeance and **(b)** selectivity of ethanol over water obtained in this study for various feed concentrations at 50 °C and permeate pressure of 100 Pa using the real adsorption solution theory and the Maxwell-Stefan formulation for an all-silica MFI membrane (1.5 μm thick zeolite layer and 3 mm thick support) pervaporation process, and compared to experimental values obtained in [26]. **(c)** Steady-state ethanol permeance and **(d)** selectivity obtained using a 120-fold reduction in diffusivity and including the effects of silanol defects compared to experimental studies in the literature.

Another discrepancy between the experimental and simulation results is the capability of simulated membranes to achieve selectivity as high as ~30 (for a 5 wt. % feed) as shown for the case "only zeolite layer" in **Figure 4.42b**. However, even for thicker membranes in which the permeation should be governed by mostly the zeolite layer, such high selectivity has not been experimentally reported in the published literature. The maximum selectivity obtained in the literature is ~10 as shown in **Figure 4.4d**. This may be because the simulation results are obtained for defect-free crystals while the presence of hydrophilic silanol groups at the grain boundaries and/or as internal defects in real membranes result in reduced selectivity [108,109,209,236]. It has been shown that up to 10 water molecules/UC (unit cell) can be adsorbed on silanol defects present in silicalte-1 crystals. Thus, the high selectivity realized in simulated membranes is not exhibited by the real membranes.

The above-mentioned discrepancies can be accounted for in the model by reducing the permeation rate through the membrane and incorporating the effects of silanol defects. The permeation is reduced by using lower diffusivity values as suggested from the macroscopic measurements. It has been shown that the ethanol adsorption on hydrophobic zeolites is largely unaffected by water molecules but water adsorption is severely affected by ethanol molecules [52,240]. Thus, the effects due to silanol defects are incorporated by increasing the loading of water molecules. Furthermore, the defects become more prominent at lower ethanol loading when the zeolite is not saturated. At high ethanol loading, the adsorption of water is restricted by the presence of ethanol molecules. The following empirical relation was used to determine the loading of water molecules:

$$q_{\text{water\_with\_defects}} = q_{\text{water\_without\_defects}}\left(1 + A(1 - q_{ethanol}/q_{ethanol\_sat})\right) \tag{4.3}$$

where A is a fitting parameter. In addition to obtaining a good agreement between the selectivity determined from model and experiments, the value of A is selected such that the

total fractional loading is always below unity. A 120-fold reduction in diffusion coefficients (of both water and ethanol molecules) and A = 7.5 provided good agreement with experimental data [207,240–242] over the entire concentration range (**Figure 4.4c-d**). The lower permeance obtained in [241] could be attributed to the thicker membranes used in their experiments compared to those in our model.

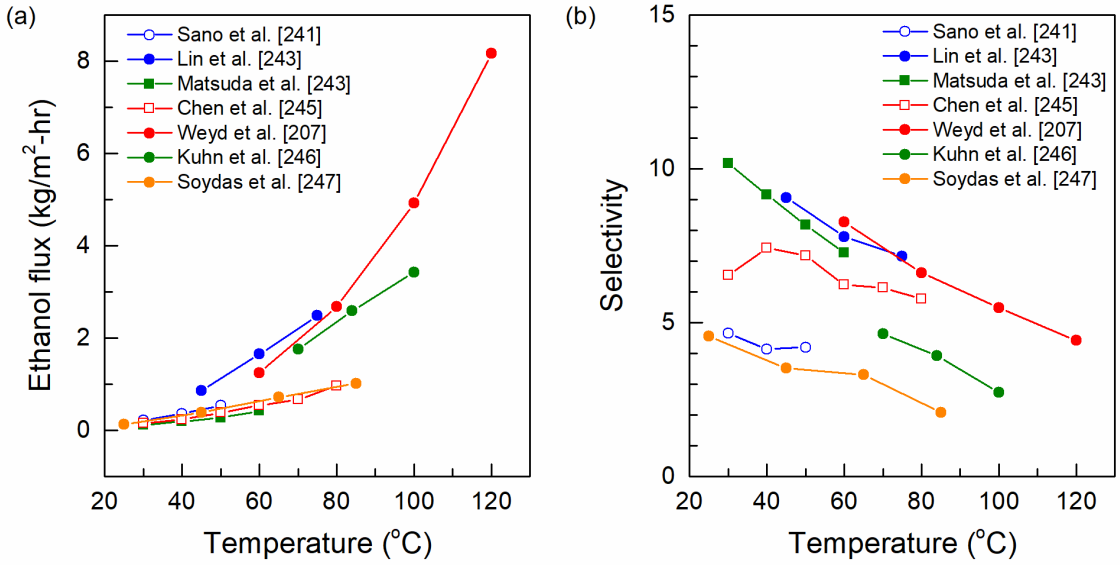

Figure 4.5: Temperature dependence of **(a)** steady-state ethanol flux and **(b)** selectivity of ethanol over water in MFI membranes for a 3-7 wt. % ethanol feed.

Due to the lack of adsorption and diffusion data at higher temperatures, the model developed is restricted to a feed temperature of 50 °C. However, it is well established from experimental studies [207,241,243–247] that the flux increases significantly with increasing temperature (due to an increase in driving force due to higher vapor pressure) while the selectivity decreases. As shown in **Figure 4.5**, the flux increases 4 to 5-fold from 40 °C to 80 °C and another 3-fold from 80 °C to 120 °C while a 2-fold decrease in selectivity is observed. Thus, in order to describe the membrane separation performance at 120 °C with our model, the relative permeation of ethanol over water in the model was reduced by 2-fold from its value at 50 °C. A comparison of the selectivity obtained from the model and those obtained in the experiments [207] is shown in **Figure 4.6**. The required

membrane area for 120 °C is estimated to be 1/9th of that required for 50 °C due to a 9-fold increase in ethanol permeation.

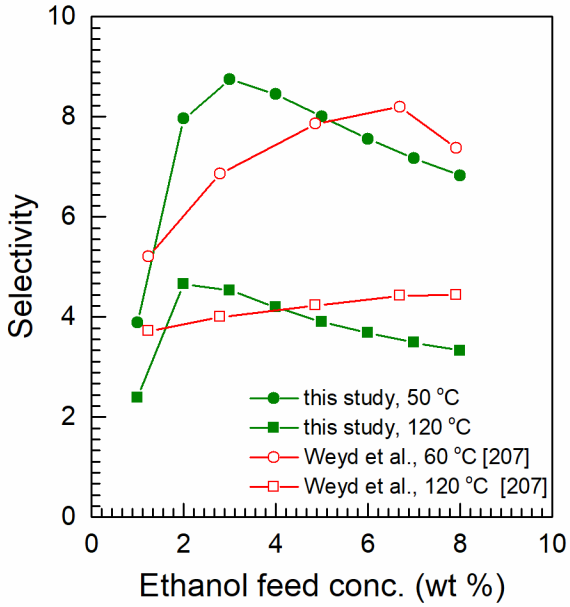

Figure 4.6: Simulation results for selectivity of ethanol over water in MFI membrane permeation obtained using the model at 50 °C and using a reduced-selectivity model for 120 °C compared to the experimental results obtained by Weyd et al. [207].

4.8 Review of process design studies

Most of the process design studies in the literature are either focused on hydrophobic membranes integrated with fermentation (reaction-separation integration) at very low ethanol concentration [248–250] or on hydrophilic membranes for enrichment over the azeotropic concentration [251]. Relatively few studies exist for using membranes with distillation (separation-separation integration) at low to intermediate ethanol concentration. A process using a combination of distillation, hydrophobic membranes and hydrophilic membranes, but without heat integration, has been proposed [252]. A heat-integrated low-energy membrane/distillation process using both hydrophilic and hydrophobic membranes has also been proposed [253,254]. However, only polymer membranes have been considered in these studies. While zeolite membranes have shown better performance than

polymer membranes, the high cost and the lack of large-scale production capability are some of their major challenges [2,253]. However, the continuing commercialization of hydrophilic zeolite membranes [13] and the improvements in separation performance of hydrophobic zeolite membranes may overcome these limitations and enable commercialization of hydrophobic membranes as well. With this motivation, the process model developed for zeolite membrane separation is further used in designing heat integrated flowsheets for bioethanol enrichment, considering both hydrophobic and hydrophilic membranes. Thus, this research provides a comprehensive assessment of zeolite membrane separation for bioethanol enrichment, from atomistic-level simulation to process-scale design. Although beyond the scope of this research, the membrane model developed can be used for other bio refinery applications [255].

4.9 Base-case distillation for ethanol enrichment

The separation process for recovering fuel-grade ethanol from the fermentation broth has been published by the National Renewable Energy Laboratory (NREL) [256]. The fermentation broth product, also known as beer, contains 5.5 wt. % ethanol and is enriched up to near azeotropic composition (93 wt. %) by a sequence of two distillation columns (beer column and rectification column). This is followed by molecular sieves adsorption process to achieve fuel-grade ethanol of 99.5 wt. %. The process flow diagram is shown in **Figure 4.7**.

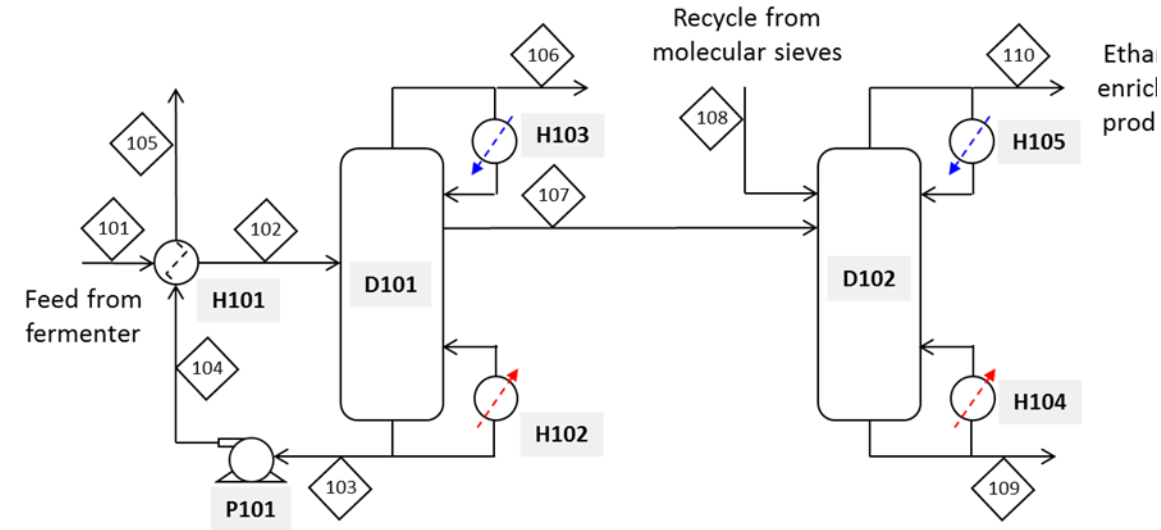

Stream Name	Ethanol kg/hr	Water kg/hr	Temp °C	Pres atm	Vap fraction	Mass_% Ethanol
101	21941	378525	32	6	0	5.48%
102	21941	378525	103	6	0	5.48%
103	184	341765	125	2.8	0	0.05%
104	184	341765	125	6.3	0	0.05%
105	184	341765	47	6.3	0	0.05%
106	66	23	60	2	1	74.16%
107	21691	36737	117	2.1	1	37.12%
108	5349	2056	71	1.7	0	72.23%
109	18	36629	114	1.6	0	0.05%
110	27022	2164	91	1.6	1	92.59%

Equipment Name	Duty MW	
H101	34.16	
H102	38.38	
H103	-0.54	
H104	6.57	
H105	-26.94	
P101	0.008	

Figure 4.7: Conceptual process flow diagram of base-case distillation for bioethanol enrichment based on the NREL report [256].

The beer column enriches the low concentration ethanol product from the fermenter to 37 wt. % with a recovery of 99 %. The ethanol enriched stream is fed to the rectification column. In addition, a 72 wt. % recycle stream from the molecular sieve adsorption process is also fed to the rectification column. The vapor overhead from the rectification column recovers 99.9 % of ethanol at 93 wt. %. Further dehydration to fuel grade ethanol (99.5 wt. %) is carried out by molecular sieve adsorption. Recently, hydrophilic zeolite membranes have also been implemented in industry for this dehydration step [13]. As zeolite membranes/molecular sieves have already been commercialized for ethanol enrichment over the ethanol/water azeotropic composition, the viability of zeolite

membranes only for separation to achieve the azeotropic composition is examined in this study. The total heating and cooling duties required for distillation separation are 45 MW and 27.5 MW, respectively. As heating and cooling duties require different amount of fuel per unit of energy, the corresponding fuel-equivalent energy is also calculated. The fuel-equivalent energy for heating duty (steam) is estimated considering a boiler efficiency of 90 % so that 1 MJ of steam energy requires 1.11 MJ fuel-equivalent energy. The minimum energy cost associated with cooling is estimated using an expression obtained from the Carnot cycle:

$$E_{\text{elec}} = E_{\text{cooling}} \times \frac{\left(T_{ambient} - T_{cooling}\right)}{T_{cooling}} \tag{4.4}$$

where E_{elec} is the electric power required for a unit of cooling power (E_{cooling}) at a temperature of T_{cooling}. Furthermore, the fuel-equivalent energy for cooling duty is estimated considering a compressor efficiency of 90%, ambient temperature of 300 K and 3 MW-fuel equivalents for 1 MW of electrical power. The corresponding fuel-equivalent energy is determined to be 8.29 MJ-fuel/kg-ethanol. As the process also includes the additional energy associated with the recycle stream from the molecular sieves, the corrected energy is calculated to be 7.67 MJ-fuel/kg-ethanol for concentration up to azeotropic composition. For reference, the heat of combustion of ethanol is 30 MJ/kg [201]. In the next sections, the separation performance of both the hydrophobic and hydrophilic zeolite membranes is analyzed and evaluated against the distillation process.

4.10 Application of zeolite membranes at low ethanol concentration

As the fermentation product contains ~ 5 wt. % ethanol, only ethanol-selective hydrophobic MFI membranes are examined.

The membrane process can be operated either in an end-of-pipe mode or a slip-stream mode. In the end-of-pipe process, the alcohol is recovered after the fermentation has

reached completion while in a slip-stream process, alcohol recovery and fermentation are carried out simultaneously. Although the slip-stream process reduces product inhibition and improves fermenter productivity, additional preconditioning such as degassing, heating and solids removal is necessary before ethanol recovery. Furthermore, the effect of broth components on the membrane fouling and on the thermodynamics and transport of water-ethanol mixture through the membrane should be included. Other considerations in integrating the pervaporation with the fermentation system have been reviewed by Vane et al. [203]. Fermenter modeling and its response to continuous removal of ethanol is beyond the scope of this study and, thus, zeolite membrane separation with only end-of-pipe recovery mode is considered.

Another design parameter is the feed temperature. Fermentation is usually carried out below 30 °C as higher temperatures can be lethal to the micro-organism [201]. Temperatures larger than 60 °C also cause enzyme deactivation. Recovery at near fermenter temperature allows recycling of micro-organism and enzymes, thus increasing fermenter productivity. It also eliminates the need for heating and the associated heat transfer equipment. However, for pervaporation, the driving force due to the saturated vapor pressure on the feed side increases with temperature leading to higher flux at elevated temperatures, but with a decrease in selectivity. For instance, for a 5 wt. % mixture, ethanol partial vapor pressure is 0.9 kPa at 30 °C, 2.7 kPa at 50 °C and 10.4 kPa at 80 °C, as determined using the non-random two-liquid (NRTL) vapor-liquid equilibrium. As ethanol partial pressure on the permeate side should be lower than that on the feed side, the permeate should be immediately condensed so that the total pressure on the permeate side is equal to the corresponding vapor pressure of the condensed permeate. Thus, another advantage associated with high-temperature pervaporation is that the permeate can be maintained at near room temperature without the need of expensive cooling, e.g.,

temperature as low as -30 °C is required for a permeate pressure of 0.1 kPa, -5 °C for 1.0 kPa and 20 °C for 5 kPa. Cooling at -30 °C requires 0.78 MW-fuel/MW-cooling which is almost double the amount of energy than that required for cooling at -5 °C (0.40 MW-fuel/MW-cooling). Here, feed temperatures of 50 °C and 120 °C and permeate pressures of 1 kPa and 5 kPa are considered.

The low pressure on the permeate can be generated using vacuum pumps and/or ejectors [257]. The vacuum generation will be required only at the start-up and the resulting low pressure can be subsequently maintained by condensing the permeate considering there are no air-leaks. However, air leakage into the vacuum system is an important concern and ejectors are commonly applied in process industries for evacuating the leaked air and maintaining pressures below atmospheric pressures. Thus, an ejector system was designed according to the procedure specified in [257] for maintaining pressure with a suction load equivalent to air leak rate (**Figure 4.8**).

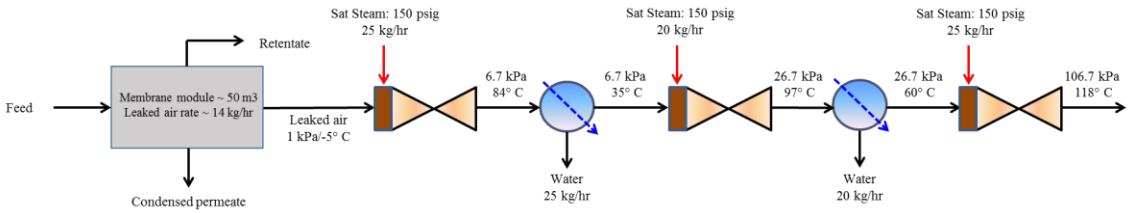

Figure 4.8: A 3-stages ejector system in series for evacuating the leaked air for a 10,000 m^2 membrane module operating at a permeate pressure of 1 kPa.

The permeate pressure of 1 kPa was maintained by implementing a 3-stages ejector system in series i.e. from 7.5 torr (1 kPa) to 50 torr (6.7 kPa), from 50 torr (6.7 kPa) to 200 torr (26.7 kPa) and from 200 torr (26.7 kPa) to 800 torr (106.7 kPa). Considering a membrane area of 10,000 m^2 and a packing of 100 m^2/m^3, the permeate volume is calculated to be ~ 50 m^3. The corresponding air leak rate is determined to be 14 kg/hr. The total medium pressure steam usage is calculated to be 70 kg/hr and the cooling water usage

to be 2,640 kg/hr. A total of 0.05 MW of fuel power is consumed which amounts to only 0.007 MJ-fuel/kg-ethanol. The size of three ejectors is estimated to be 3 in. by 30 in. (weight: 200 lb), 1.5 in. by 15 in. (weight: 70 lb), and 1 in. by 10 in. (weight: 40 lb), respectively, while the size of the condensers are estimated to be 2.7 m^2 and 0.4 m^2. Thus, this process requires only a small amount of energy and capital cost which is insignificant compared to the requirement for the overall process.

As the pervaporation involves phase change from liquid to vapor phase, energy corresponding to latent heat is supplied on the retentate side. Cooling is needed on the permeate side to condense the permeate and maintain the required temperature. The separation performance for a recovery of ~ 99 % (similar to that obtained for the beer column) is shown in **Figure 4.9**. The required membrane area and ethanol purity with increasing recovery is shown in **Figure 4.10.** It is found that the membranes at their current performance are unable to match the purity obtained by the beer column. Furthermore, the membrane area required for 50 °C operation is prohibitively large. Only defect-free membranes at 120 °C operation appear promising in that they can meet the beer column purity and require reasonable membrane area (~10,000 m^2). As shown in **Figure 4.9**, permeate pressure of 1 kPa yields better purity and requires less area as compared to that for 5 kPa. However, maintaining a permeate pressure of 1 kPa requires expensive cooling (at -5 °C) as opposed to cooling at near ambient temperature (20 °C) for a permeate pressure of 5 kPa.

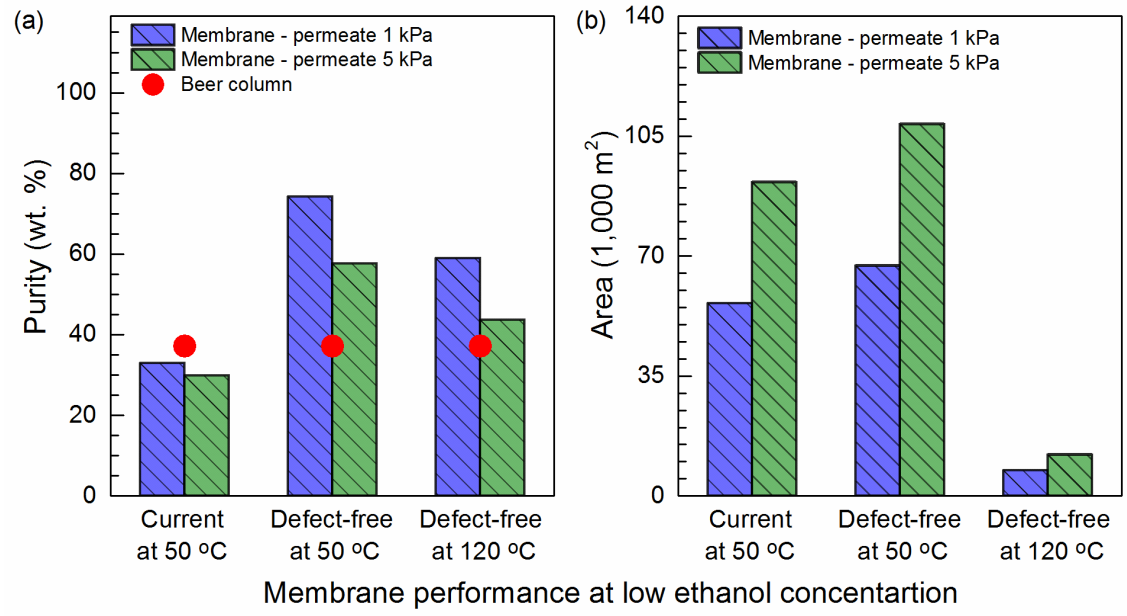

Figure 4.9: (a) Ethanol purity obtained and (b) membrane area required for bioethanol enrichment of low ethanol concentration feed (5 wt. %) obtained from the fermenter using hydrophobic MFI zeolite membranes for a permeate pressure of 1 kPa and 5 kPa. The corresponding purity for the beer column is also shown.

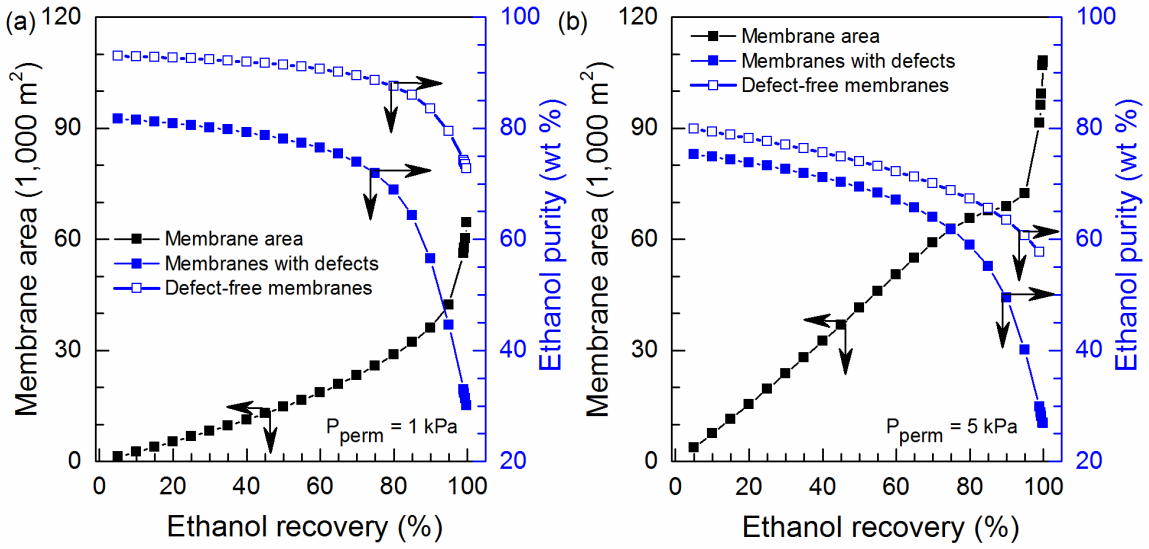

Figure 4.10: Simulation results for the separation performance of hydrophobic MFI zeolite membrane (1.5 μm thick zeolite layer and 3 mm thick support) for an aqueous feed at a low ethanol concentration of ~ 5 wt. % from fermenter. Feed temperature of 50 °C and a permeate pressure of (a) 1 kPa and (b) 5 kPa. The corresponding purities for defect-free membranes are also shown.

The separation for both the cases (permeate pressure of 1 kPa and 5 kPa) for defect-free membranes operating at 120 °C is further analyzed to estimate the total energy requirement. The ethanol enriched permeate stream is fed to the distillation (rectification) column to achieve the target purity of 92.6 wt. % (**Figure 4.11)**. A major part of energy is consumed in the reboiler duty of the rectification column and as the latent heat associated with the pervaporation process. The increase in reboiler duty of the rectification column as compared to that required for base case is due to the low-temperature liquid feed permeate in the membrane process as opposed to high-temperature vapor product obtained from the beer column. The significant amount of energy on the feed side of the pervaporation process is attributed to the ~ 3-fold larger latent heat of water (~ 2.26 MJ/kg) as compared to that of ethanol (~ 0.84 MJ/kg). Thus, water consumes almost 77 % of the latent energy for a permeate pressure of 5 kPa. This energy can be reduced by lowering the permeate pressure as it results in lesser water permeation. At a permeate pressures of 1 kPa, the energy required on the feed side reduces by 35 %. However, the additional energy required for cooling on the permeate side associated with lower permeate pressure results in only modest total energy savings. Nonetheless, the total energy requirement (~ 12 MJ-fuel/kg-ethanol) is almost 1.5-fold as compared to that for distillation. Furthermore, at the current cost estimate for zeolite membranes ($1,000-5,000/$m^2$) [13], the membrane area requirement would result in a capital cost of over 8 million USD. In comparison, the capital cost of the beer column, based on the specifications provided in the NREL report [256], is estimated to be only ~ 2 million USD. Thus, the membrane separation process results in higher energy and capital cost than distillation. This superior performance of distillation over membrane separation can be attributed to the favorable vapor-liquid equilibrium (high relative volatility) for water-ethanol mixture at low concentration and the high energy (latent heat) requirement associated with water permeation in the pervaporation process.

As the effect of both these factors diminishes, i.e., both the relative volatility and the amount of water permeation decreases with increasing ethanol concentration, the membrane separation for intermediate ethanol concentration feed is analyzed next.

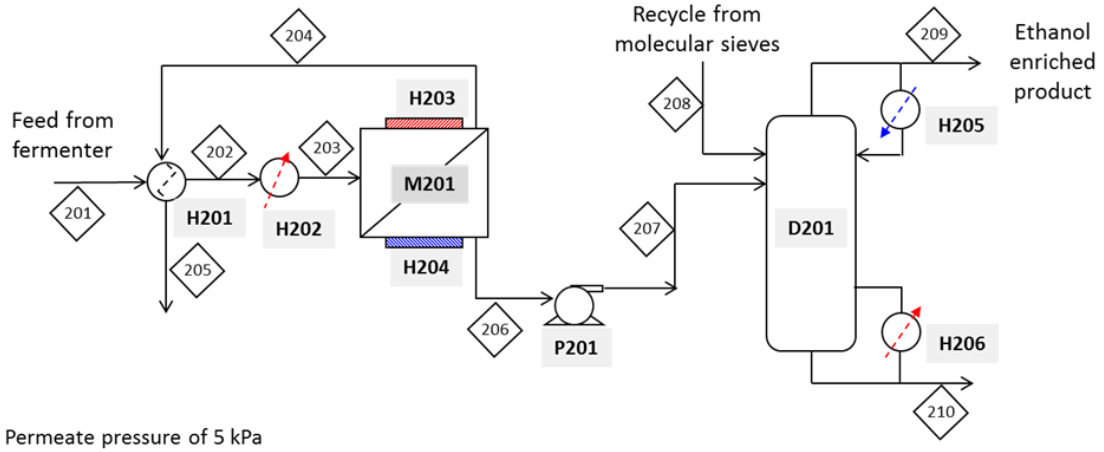

Permeate pressure of 5 kPa

Stream Name	Ethanol kg/hr	Water kg/hr	Temp °C	Pres atm	Vap fraction	Mass_% Ethanol
201	21941	378525	32	6	0	5.48%
202	21941	378525	99	6	0	5.48%
203	21941	378525	120	6	0	5.48%
204	250	350401	120	6	0	0.07%
205	250	350401	47	6	0	0.07%
206	21691	28124	20	0.05	0	43.54%
207	21691	28124	20	2	0	43.54%
208	5349	2056	71	1.7	0	72.23%
209	27023	2160	91	1.6	1	92.60%
210	17	28020	117	1.8	0	0.06%

Equipment Name	Duty MW	Fuel MJ/kg
H201	30.20	0.00
H202	10.30	1.90
H203	22.02	4.06
H204	-27.20	0.00
H205	-24.14	0.00
H206	35.71	6.58
P201	4.715	0.00

Permeate pressure of 1 kPa

Stream Name	Ethanol kg/hr	Water kg/hr	Temp °C	Pres atm	Vap fraction	Mass_% Ethanol
201	21941	378525	32	6	0	5.48%
202	21941	378525	99	6	0	5.48%
203	21941	378525	120	6	0	5.48%
204	250	350401	120	6	0	0.07%
205	250	350401	47	6	0	0.07%
206	21691	15187	-5	0.01	0	58.82%
207	21691	15187	-5	2	0	58.82%
208	5349	2056	71	1.7	0	72.23%
209	27023	2160	91	1.6	1	92.60%
210	17	15083	117	1.8	0	0.11%

Equipment Name	Duty MW	Fuel MJ/kg
H201	30.20	0.00
H202	10.30	1.90
H203	14.00	2.58
H204	-18.50	1.23
H205	-21.88	0.00
H206	33.45	6.16
P201	3.762	0.00

Figure 4.11: Conceptual process flow diagram of bioethanol enrichment using defect-free hydrophobic MFI zeolite membrane at low ethanol concentration feed (5 wt. %) obtained from the fermenter followed by the distillation (rectification) column. The membrane area required is 59,000 m^2 for a permeate pressure of 5 kPa and 44,000 m^2 for a permeate pressure of 1 kPa.

4.11 Application of zeolite membranes at intermediate ethanol concentration

While it is practical to use hydrophobic membranes for recovery of low ethanol feed concentration (from fermenter at 5 wt. %) and hydrophilic membranes for dehydration of high ethanol feed concentration (above azeotropic composition), both hydrophobic and hydrophilic membranes can be used at intermediate feed concentration (from the beer column at 37 wt. %). In this section, process designs based on hydrophobic membranes, hydrophilic membranes and a combination of the two are analyzed.

4.11.1 Hydrophobic membranes

The separation performance of MFI zeolite membranes for a recovery of ~ 99 % (similar to that obtained for the rectification column) is shown in **Figure 4.12**. The membrane area and purity with increasing recovery is shown in **Figure 4.13**. It is found that the target purity (~ 93 wt. % as attained for the rectification column) can only be achieved for defect-free membranes operating at a feed temperature of 50 °C and a permeate pressure of 1 kPa. The corresponding total membrane area required is found to be ~ 21,000 m^2. At a cost estimate of \$1,000/m^2, it would result in an excessive capital cost of over 20 million USD. In comparison, the cost of the rectification column based on the specifications provided in the NREL report [81], is estimated to be ~1.5 million USD. Although the area can be reduced to ~ 2,400 m^2 by operating at 120 °C (**Figure 4.13**), it results in a purity of only 85 wt. % as the selectivity decreases by 2-fold on increasing the temperature from 50 °C to 120 °C. Thus, in addition to defect-free membranes, either a 5- to 10-fold improved permeance for operation at 50 °C or a 2-fold improved selectivity for operation at 120 °C is required to meet the rectification column purity with a reasonable area requirement.

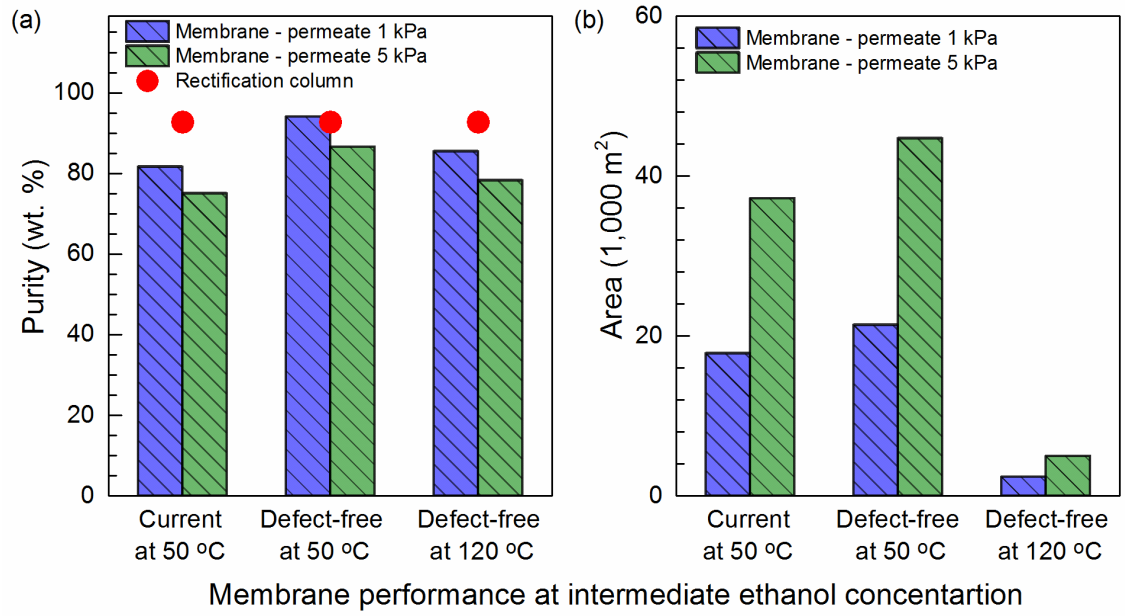

Figure 4.12: (a) Ethanol purity obtained and (b) membrane area required for bioethanol enrichment of intermediate ethanol concentration feed (37 wt. %) obtained as the beer column product using hydrophobic MFI zeolite membranes for a permeate pressure of 1 kPa and 5 kPa. The corresponding purity for the rectification column is also shown.

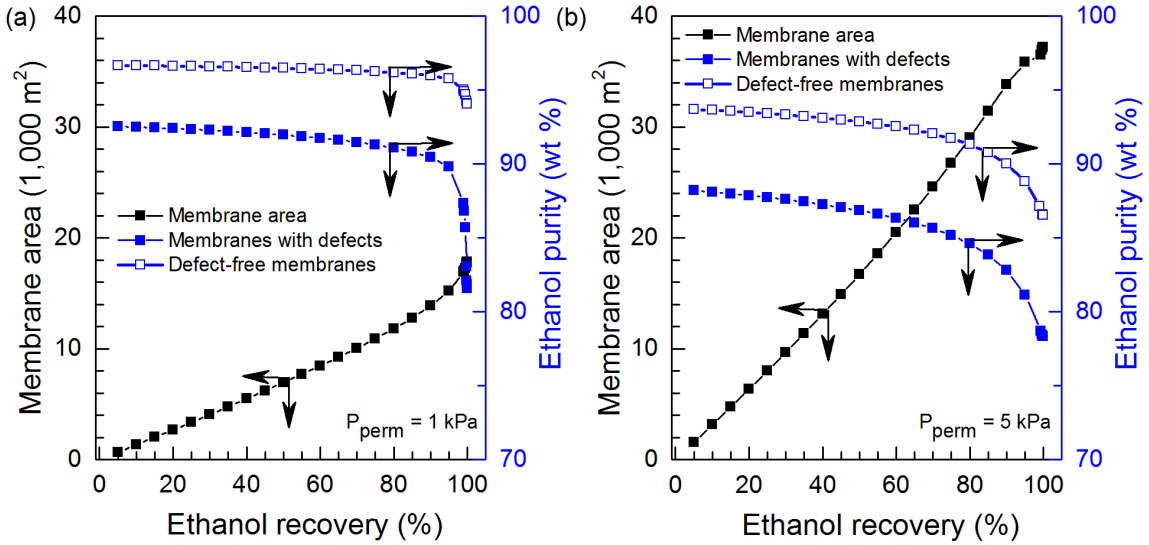

Figure 4.13: Simulation results for the separation performance of hydrophobic MFI zeolite membrane (1.5 μm thick zeolite layer and 3 mm thick support) for aqueous feed at an intermediate ethanol concentration of ~ 37 wt. % from beer column. Feed temperature of 50 °C and a permeate pressure of (a) 1 kPa and (b) 5 kPa. The corresponding purities for defect-free membranes are also shown.

An energy analysis was also performed to compare the membrane separation process against distillation. Defect-free membranes operating at a feed temperature of 50 °C and a permeate pressure of 1 kPa are considered. As the ethanol enriched stream from the beer column is obtained at 117 °C and the membrane is operated at 50 °C, the heat released during condensation is integrated within the process to provide heat of vaporization for pervaporation process and to heat the cold permeate streams. The resulting process flow diagram is shown in **Figure 4.14**. The total amount of energy required is determined to be 7.67 MJ-fuel/kg-ethanol. If similar purity can be obtained at a permeate pressure of ~ 5 kPa, the energy consumption can be further reduced to 7.07 MJ-fuel/kg-ethanol resulting in ~ 15 % savings as compared to the base case requirement of 8.29 MJ-fuel/kg-ethanol. However, the large membrane area required for the membrane separation poses a challenge for their implementation.

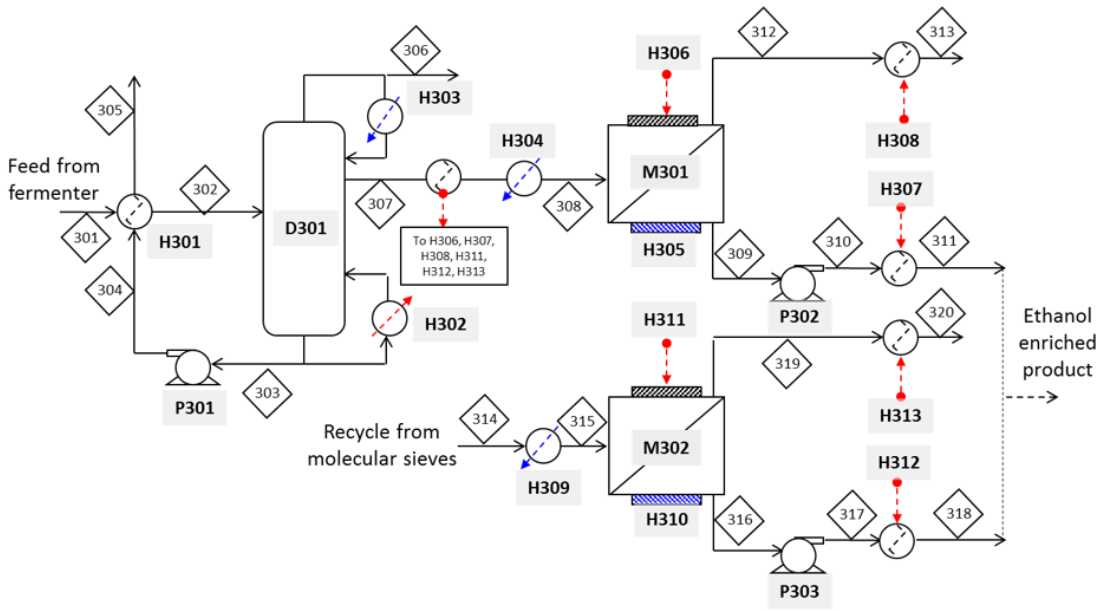

Stream Name	Ethanol kg/hr	Water kg/hr	Temp °C	Pres atm	Vap fraction	Mass_% Ethanol
301	21941	378525	32	6	0	5.48%
302	21941	378525	52	6	0	5.48%
303	184	341765	125	2.8	0	0.05%
304	184	341765	125	6.3	0	0.05%
305	184	341765	47	6.3	0	0.05%
306	66	23	60	2	1	74.16%
307	21691	36737	117	2.1	1	37.12%
308	21691	36737	50	2.1	0	37.12%
309	21644	1362	-10	0.01	0	94.08%
310	21644	1362	-10	1.63	0	94.08%
311	21644	1362	91	1.63	1	94.08%
312	47	35375	50	2.1	0	0.13%
313	47	35375	110	2.1	0	0.13%
314	5349	2056	71	1.7	0	72.23%
315	5349	2056	50	1.7	0	72.23%
316	5340	174	-10	0.01	0	96.84%
317	5340	174	-10	1.63	0	96.84%
318	5340	174	91	1.63	1	96.84%
319	9	1882	50	1.7	0	0.48%
320	9	1882	110	1.7	0	0.48%

Equipment Name	Duty MW	Fuel MJ/kg
H301	34.16	0.00
H302	38.38	7.07
H303	-0.54	0.00
H304	11.87	0.00
H305	-7.32	0.49
H306	6.24	0.00
H307	7.70	0.00
H308	2.57	0.00
H309	-0.15	0.00
H310	-1.69	0.11
H311	1.43	0.00
H312	1.78	0.00
H313	0.14	0.00
P301	0.008	0.00
P302	0.002	0.00
P303	0.001	0.00

Figure 4.14: Conceptual process flow diagram of bioethanol enrichment using defect-free hydrophobic MFI zeolite membranes (M301) at intermediate ethanol concentration feed (37 wt. %) obtained as the beer column side draw. The recycle stream from molecular sieves is also fed to defect-free hydrophobic MFI zeolite membranes (M302). The membrane area required is 21,000 m^2 for M301 and 3,500 m^2 for M302.

4.11.2 Hydrophilic membranes

As hydrophilic zeolite membranes have already been commercialized, their separation performance at industrial scale can be used to analyze their viability to replace the rectification column. This would require the dehydration of the beer column product from

63 wt. % water and the molecular sieve recycled stream from 28 wt. % water to nearly 7 wt. % water. As suggested earlier, the hydrophilic membrane separation process is operated in vapor permeation mode and is modeled using a constant water permeance of 2.5 x 10^{-6} mol/m^2-sec and a selectivity of 10,000 based on the performance exhibited by commercial hydrophilic membranes. A feed temperature of 120 °C is considered while the permeate is maintained at 40 °C (~ 10 kPa). Simulations were performed to determine the membrane separation performance and the results are shown in **Figure 4.15**. For the ethanol recovery of 99.93 %, the total membrane area is found to be ~ 3,300 m^2 and the overall purity is determined to be ~ 98 wt. %. At a membrane cost of $1,000/$m^2$, it would cost a total of ~ 3.3 million USD. Thus, hydrophilic membranes can achieve higher than the target purity at a capital cost comparable to the distillation column.

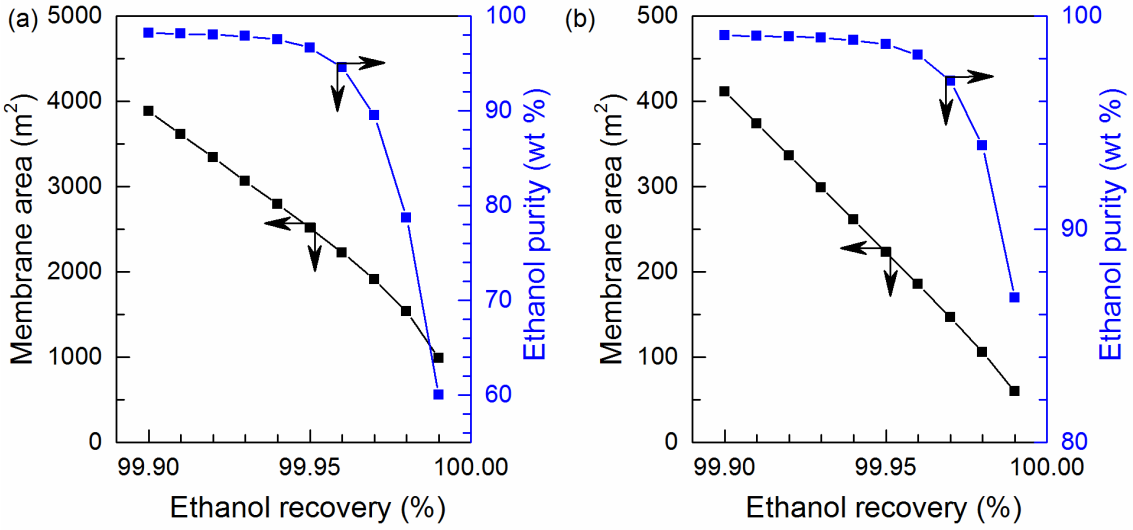

Figure 4.15: Simulation results for the separation performance of hydrophilic NaA zeolite membrane for vaporized feed at an intermediate ethanol concentration of (a) ~ 37 wt. % from beer column and (b) ~ 72 wt. % from molecular sieve recycle at 120 °C and a permeate pressure of 10 kPa.

Next, an energy analysis was performed to compare these membranes against the rectification column. The process flow diagram is shown in **Figure 4.16**. The total energy required is determined to be 8.26 MJ-fuel/kg-ethanol which is almost equal to the base case

distillation process. The higher energy requirement for hydrophilic membrane separation is due to ~ 3-fold higher energy (latent heat of water ~ 2.26 MJ/kg) consumed during water permeation than required for ethanol permeation (latent heat of water ~ 0.84 MJ/kg) for hydrophobic membranes. Considering that almost pure components are obtained in permeate, hydrophilic membranes would be effective for ethanol feed concentration only above 72 wt. %. Alternatively, it can be argued that as the molar latent heat of vaporization for water and ethanol is almost equal (~ 40 MJ/mol), hydrophilic membranes should be more practical for a solution with > 50 mol % (~ 72 wt. %) of ethanol. As the feed (from the beer column) is only 37 wt. % (~ 20 mol %), separation using hydrophilic membranes leads to higher energy consumption than hydrophobic membranes and no energy savings can be realized by replacing the rectification column with hydrophilic membranes.

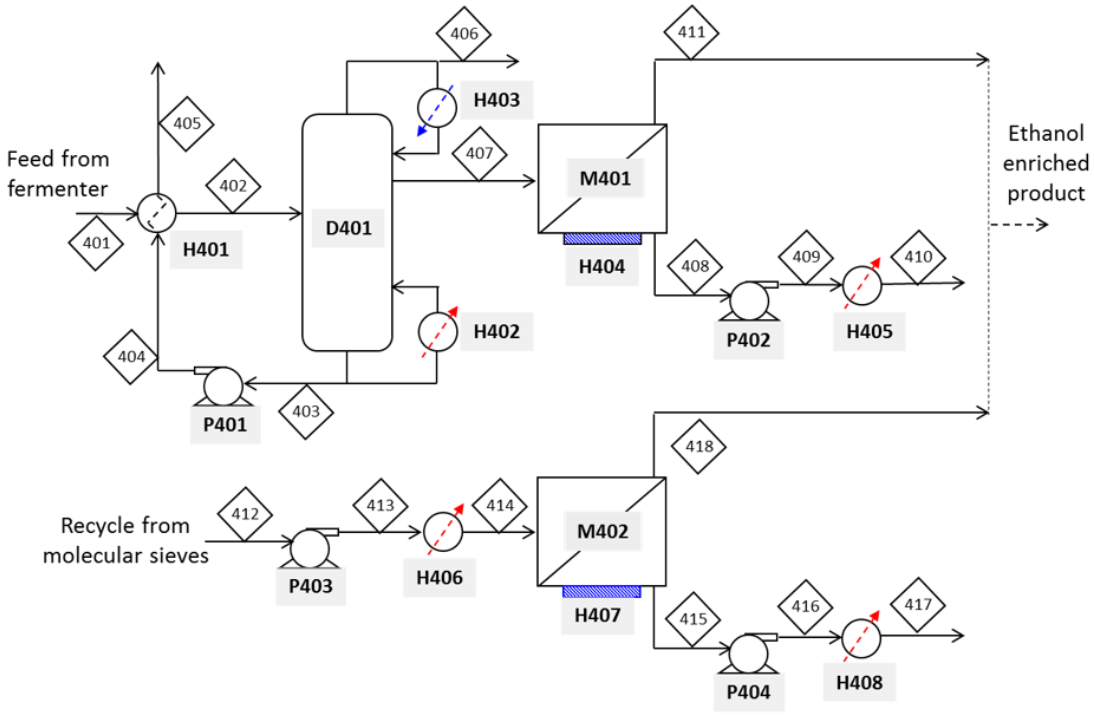

Stream Name	Ethanol kg/hr	Water kg/hr	Temp °C	Pres atm	Vap fraction	Mass_% Ethanol
401	21941	378525	32	6	0	5.48%
402	21941	378525	103	6	0	5.48%
403	184	341765	125	2.8	0	0.05%
404	184	341765	125	6.3	0	0.05%
405	184	341765	47	6.3	0	0.05%
406	66	23	60	2	1	74.16%
407	21691	36737	117	2.1	1	37.12%
408	16	36265	40	0.1	0	0.04%
409	16	36265	40	1.7	0	0.04%
410	16	36265	114	1.7	0	0.04%
411	21675	472	117	2.1	1	97.87%
412	5349	2056	71	1.7	0	72.23%
413	5349	2056	71	3.5	0	72.23%
414	5349	2056	120	3.5	1	72.23%
415	4	2001	40	0.1	0	0.20%
416	4	2001	40	1.7	0	0.20%
417	4	2001	114	1.7	0	0.20%
418	5345	55	120	3.5	1	98.98%

Equipment Name	Duty MW	Fuel MJ/kg
H401	34.16	0.00
H402	38.38	7.07
H403	-0.54	0.00
H404	-25.68	0.00
H405	3.13	0.58
H406	2.77	0.51
H407	-1.42	0.00
H408	0.17	0.03
P401	0.056	0.03
P402	0.003	0.00
P403	0.001	0.00
P404	0.000	0.00

Figure 4.16: Conceptual process flow diagram of bioethanol enrichment using hydrophilic NaA zeolite membranes (M401) at intermediate ethanol concentration feed (37 wt. %) obtained as the beer column side draw. The recycle stream from molecular sieves is also fed to hydrophilic NaA zeolite membranes (M402). The membrane area required is 3,000 m^2 for M401 and 300 m^2 for M402.

4.11.3 Combination of hydrophobic and hydrophilic membranes

As hydrophobic membranes results in energy savings but cannot attain the required purity and hydrophilic membranes are better suited for higher ethanol feed concentration,

thus, hydrophobic membrane separation followed by hydrophilic membrane separation is also considered. The corresponding process flow diagram is shown in **Figure 4.17**. As the hydrophobic membrane separation is carried out as pervaporation, the saturated vapor product from the beer column (at 117 °C) is condensed and the membrane separation is carried out at 100 °C. The heat released during condensation is used to provide heat of vaporization for pervaporation process and to heat the cold permeate streams. The permeate stream from the hydrophobic pervaporation separation is further enriched by hydrophilic membrane separation. As hydrophilic membranes show better performance during vapor permeation separation, the permeate from the hydrophobic membrane separation and the recycle stream from molecular sieves were mixed together and vaporized to 100 °C before feeding to the hydrophilic membrane unit. Ethanol recoveries of 99.95 % and 99.98 % were set for hydrophobic and hydrophilic membrane separation, respectively, to achieve a total recovery of 99.93 %.

A final purity of 93.2 wt. % is achieved for the combined process with the total membrane area requirement of ~ 9,000 m^2 (hydrophobic membrane area of ~ 8,000 m^2 and hydrophilic membrane area of ~ 1,000 m^2). The total amount of energy required is calculated to be 7.07 MJ-fuel/kg-ethanol. This results in a total energy savings of ~ 15 % as compared to the base case requirement of 8.29 MJ-fuel/kg-ethanol. In what follows, a techno-economic analysis is carried out to determine the target cost of zeolite membranes for their economic viability.

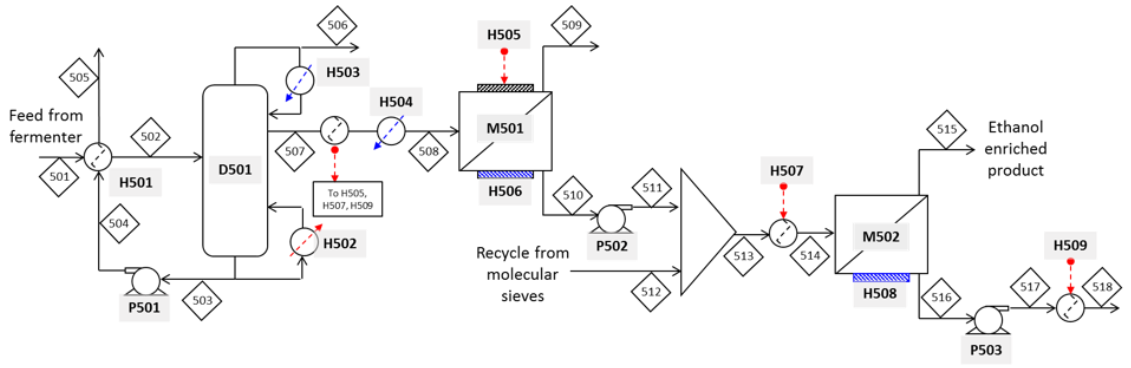

Stream Name	Ethanol kg/hr	Water kg/hr	Temp °C	Pres atm	Vap fraction	Mass_% Ethanol
501	21941	378525	32	6	0	5.48%
502	21941	378525	52	6	0	5.48%
503	184	341765	125	2.8	0	0.05%
504	184	341765	125	6.3	0	0.05%
505	184	341765	47	6.3	0	0.05%
506	66	23	60	2	1	74.16%
507	21691	36737	117	2.1	1	37.12%
508	21691	36737	100	2.1	0	37.12%
509	13	29590	100	2.1	0	0.04%
510	21678	7147	30	0.1	0	75.21%
511	21678	7147	30	1.7	0	75.21%
512	5349	2056	71	1.7	0	72.23%
513	27027	9203	39	1.7	0	74.60%
514	27027	9203	100	1.7	1	74.60%
515	27022	1958	100	1.7	1	93.24%
516	5	7245	40	0.1	0	0.07%
517	5	7245	40	1.7	0	0.07%
518	5	7245	110	1.7	0	0.07%

Equipment Name	Duty MW	Fuel MJ/kg
H501	34.16	0.00
H502	38.38	7.07
H503	-0.54	0.00
H504	4.58	0.00
H505	9.41	0.00
H506	-11.26	0.00
H507	13.97	0.00
H508	-5.07	0.00
H509	0.61	0.00
P501	0.008	0.00
P502	0.006	0.00
P503	0.001	0.00

Figure 4.17: Conceptual process flow diagram of bioethanol enrichment using defect-free hydrophobic MFI zeolite membranes (M501) at intermediate ethanol concentration feed (37 wt. %) obtained as the beer column side draw. The ethanol-enriched permeate from M501 and the recycle stream from molecular sieves is fed to hydrophilic NaA zeolite membranes (M502). The membrane area required is 8,000 m^2 for M501 and 1,000 m^2 for M502.

4.12 Techno-economic analysis

An economic assessment was performed to determine the NPV (net present value) profits over base case distillation. Only the combination of defect-free hydrophobic and hydrophilic membranes case (**Figure 4.17**) is considered as it shows the highest potential for separation. A discount rate of 10 % per annum was assumed. Furthermore, the membrane was assumed to have a lifetime of 5 years and to cost 50 % of the initial investment when replaced. Since the objective is to calculate the profits over distillation,

the labor cost, overhead expenses, and other related maintenance costs etc., were not included, as these expenses will be common for both processes. Similarly, the capital cost of the beer column is also common for both processes. However, the capital and operating expenses for the additional ancillary equipments were included in the analysis.

Table 4.2. Cost of utilities based on 2017 prices of natural gas ($3.50/GJ) and electricity ($0.07/kWh).

Utility	Cost ($/GJ)
High-pressure steam	6.17
Medium-pressure steam	4.93
Low-pressure steam	4.67
Cooling water	0.35
Cooling at 5 °C	4.43
Cooling at -5 °C	7.88
Cooling at -20 °C	13.11

The capital cost for rectification column based on the specifications provided in the report by NREL [256] is determined to be 1.39 million USD. In comparison, the capital cost for the membrane separation process considering a membrane cost of $1,000/$m^2$ is calculated to be ~ 10 million USD. For operational expenditure, the cost of various utilities is calculated using the procedure specified in [190] and is shown in **Table 4.2**. These are based on the natural gas ($3.50/GJ) and electricity ($0.07/kWh) prices for industrial use obtained from the US EIA database. The total operating cost for the base case distillation and the membrane separation are determined to be 6.32 and 5.38 million USD, respectively.

The NPV profits for a 20-year projection are shown in **Figure 4.18** for membrane cost of $100-1,000/$m^2$. It is found that at a cost of $1,000/$m^2$ (lower end of the estimate for current zeolite membrane cost), the membrane separation process results in no profit over distillation. At large scale production, the cost of zeolite membranes can be as low as $500/$m^2$ which will bring down the payback period to 4 years. However, further improvements are required to reduce the area requirement or equivalently bring down the

membrane cost to \$100/m^2 to achieve a payback period of 1 year. These improvements can either be achieved by making the supports thinner to improve the permeation [258–260] and/or replacing the expensive ceramic support by low-cost polymer-based support [261].

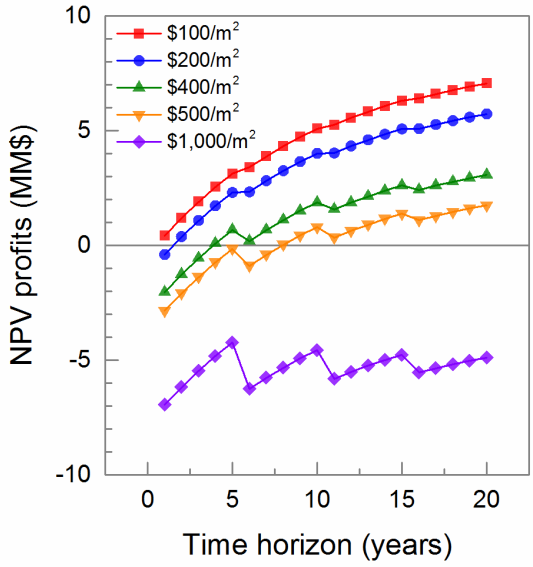

Figure 4.18: 20-year projection of Net Present Value (NPV) profits for a zeolite membrane separation process for bioethanol enrichment of intermediate ethanol concentration feed obtained at 37 wt. % from beer column using a combination of hydrophobic and hydrophilic membranes over the distillation process based on the NREL report [256]. Results shown for a membrane lifetime of 5 years, discount rate of 10 % and a membrane cost of \$100-1,000/m^2.

4.13 Conclusion

A comprehensive study of zeolite membrane separation for bioethanol enrichment is performed. Atomistic-level and molecular dynamics simulations are carried out to study the adsorption and diffusion of the ethanol-water mixture in hydrophobic all-silica MFI zeolites. The strong non-ideal interactions due to hydrogen bonding and hydrophilic defects significantly affects the separation performance of the hydrophobic zeolite membranes and thereby results in the failure of membrane models based on single component or ideal theories. To overcome these challenges, the real adsorption solution theory and the Maxwell-Stefan formulation with non-zero correlation effects for transport

were used to describe the permeation through zeolite membranes. The higher steady state permeance values predicted by the model than those determined in experiments suggest the presence of structural non-idealities, compressive stresses, and surface barriers in the real membranes and results in reduced permeation rates. Furthermore, real membranes show lower selectivity which is attributed to the presence of hydrophilic silanol defects. Hence, the diffusion coefficients in the model were reduced by a factor of 120 and the hydrophilic defects were accounted by enhanced water adsorption to obtain an experimentally validated model. For hydrophilic NaA zeolite membranes, the separation performance at industrial scale was used to determine the permeance and the selectivity.

Conceptual process design studies were also performed to study the energetic and economic viability of zeolite membranes over distillation separation. It is found that defect-free membranes are required to achieve similar performance as distillation. At low ethanol concentration, both the high relative volatility of ethanol over water and the significant energy requirement associated with latent heat for the pervaporation process favor distillation over membrane separation. At intermediate ethanol concentration, it is found that hydrophobic zeolite membranes have potential for energy savings but a 2-fold improvement in selectivity is required to meet distillation purity. Hydrophilic zeolite membranes can achieve higher purity than distillation but consume almost similar energy as that required for distillation. Thus, a combination of hydrophobic and hydrophilic membrane separation is considered which can achieve the required purity with 15 % energy savings over distillation. The techno-economic analysis suggests that ~ 10-fold improvements in permeation or equivalent cost reductions are required for economic viability of this scheme.

Chapter 5: Debottlenecking heat-integrated propylene-propane distillation separation using membranes

5.1 Introduction

Olefins, such as ethylene and propylene, are one of the largest feedstocks of chemical industry, and precursors to several important polymers and organic chemicals including polyethylene, polypropylene, ethylene oxide, isopropyl alcohol, etc. This is also recognized from their (ethylene and propylene) combined global annual production capacity which exceeds 200 million tonnes, and is expected to increase at a growth rate of ~4% [262,263]. Most of these olefins are obtained by cracking from light hydrocarbons including ethane and propane [264]. As a part of their production process, olefin/paraffin separation is required and is traditionally accomplished using distillation. Due to similar boiling points (or low relative volatility), distillation results in a capital and energy intensive separation. The separation is performed under high pressure (> 10 bar) and requires cryogenic conditions (-30 °C) for ethane/ethylene separation (C2 splitter) [265], and over 200 trays for propylene/propane separation (C3 splitter) [266].

Membrane separation is one of the several alternate processes [267–271] proposed for this separation. As replacement of distillation column is not feasible at the current membrane separation performance, hybrid membrane-distillation has been proposed for near-future application, and has been extensively studied for olefin/paraffin separation in the literature [262,272]. A selectivity of ~20 is considered effective for both ethane/ethylene [265,273] and propylene/propane separation [274–277], and has been shown to achieve 20-30% energy or total cost savings. It is also expected that the

improvement in separation performance of membranes over time can eventually lead to the replacement of C2 and C3 splitter [262,272].

In all of above mentioned hybrid membrane-distillation studies, a conventional distillation column is selected as the base case. On the other hand, heat-integrated columns have also been evaluated for energy savings in separation using distillation [8,278,279]. Both external and internal heat integrated columns have been considered. In external heat integration, the vapor from the top tray is compressed to an extent such that the increase in temperature allows heat-exchange with the condenser before entering as a reflux stream. In internal heat integrated columns, similar heat exchange can also take place between the trays in stripping and rectification section of the column. It has been shown that an external heat integrated consumes ~6-fold lesser energy when compared to conventional column for propylene/propane separation [8,278]. Further, an internal heat integrated column only achieves marginal or no energy savings over an external heat integrated column for propylene/propane separation. Nonetheless, the heat integration offers potential savings [279].

Although membranes have shown potential in hybrid configuration with conventional distillation column, no studies exist to evaluate their performance compared to heat-integrated distillation column. In this research, the scope of membranes for propylene/propane separation is evaluated, and compared to both the conventional and heat-integrated columns. Further, their application for propylene recovery from reactor purge stream in the synthesis of products, such as polymers, cumene, isopropyl alcohol etc. is also considered [272,280]. These purge streams are usually lost or flared which is inefficient from both the energy and the environmental considerations. Although these streams are small for distillation to be economical, implementation of membrane separation proposes savings over a few million USD annually [272,280].

5.2 Separation using distillation

5.2.1 Conventional distillation column

A distillation column (**Figure 5.1a**) for obtaining 99.7 mol % pure propylene (polymer-grade propylene) at an annual production of 250,000 tonnes was simulated using RadFrac model in Aspen Plus. A feed of 70 mol % propylene is considered, and the column is simulated to obtain 99 mol % propane as bottoms. The number of trays was fixed at 247, and a uniform pressure of 15 bar (top temperature of 35 °C) is considered which allows cooling water to be used as the cooling duty. Redlick-Kwong-Soave model was selected as the property method. A temperature-independent heat of vaporization of 18.5 kJ/mol was used for both the components as obtained from the database on NIST website [281,282]. The heat of vaporization obtained from Aspen properties declines with temperature, and is thus overridden for energy calculation. The energy consumption and other results are shown in **Table 5.1**, and are in agreement with the results obtained in the literature [266,274]. As shown, > 50 MW of reboiler and condenser duties are required reflecting an energy-intensive process.

Table 5.1. Feed conditions and separation performance of C3 splitter

Feed pressure	15 bar
Feed vapor fraction	0
Feed flowrate	295.53 mol/s
Feed propylene mol %	70.0 mol %
Column pressure	15
Total stages	247
Feed stage	192
Trays	247
Propylene in distillate	99.7 mol %
Propane in bottoms	99.0 mol %
Reboiler duty	56.49 MW
Condenser duty	56.34 MW

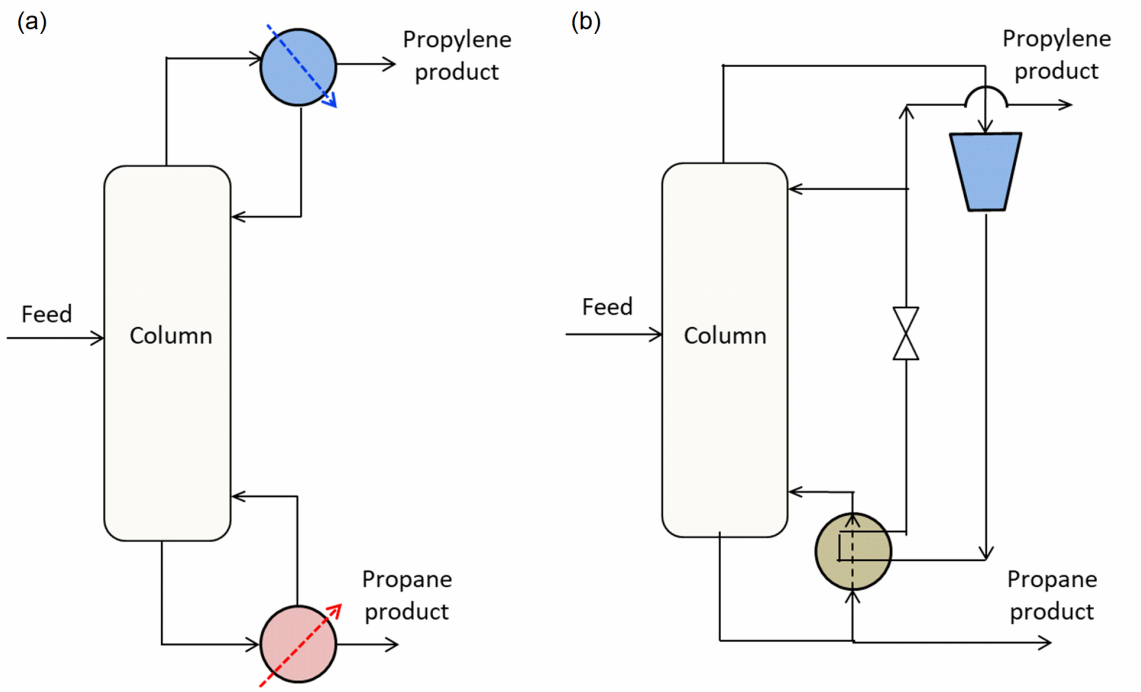

Figure 5.1: Schematic of **(a)** a conventional distillation column, and **(b)** a heat-integrated vapor recompression distillation column for propane-propylene separation (C3 splitter).

5.2.2 Heat integrated distillation column

A heat integrated column was also modeled. The heat integration can be broadly performed in two ways: (i) in an external heat integration, the vapor from the top tray is compressed to an extent such that the increase in temperature allows heat-exchange with the condenser before entering as a reflux stream, and (ii) in an internal heat integrated columns, additional heat exchange can also take place between the trays in stripping and rectification section of the column [283]. It has been shown that an external heat integrated consumes ~6-fold lesser energy when compared to conventional column for propylene/propane separation [8,278]. Further, an internal heat integrated column only achieves marginal or no energy savings over an external heat integrated column for propylene/propane separation, and adds more design complexities [8,279]. Thus, an external heat-integrated column, also known as vapor recompression column, is selected

in this study (**Figure 5.1b**). In a conventional distillation column, the condenser temperature is lower than the reboiler temperature and prohibits heat integration. In a vapor recompression column, the vapor stream is compressed so that its temperature rises above the bottom stream temperature, and enables heat integration between condenser and reboiler. It should be noted that the lesser the difference in the boiling points of the components, the lesser is the energy required for compression to enable heat-integration. The energy requirement of a vapor recompression column operating at pressures of 12 and 15 bar with temperature difference (corresponding saturation temperature at higher pressure – reboiler temperature) of 5 °C and 10 °C are calculated. The heat integrated column under these conditions requires 2-3 MW of compressor energy as opposed to ~ 50 MW of thermal energy required for conventional column. The discrepancy between energy consumption (20-fold lesser energy as opposed to 6-fold lesser energy in the literature [8,278]) is due to our approach for using heat of vaporization values from NIST website as opposed to using inherent values from Aspen database. Further, as compression work has high exergy than thermal energy (fuel-equivalent energy for electricity is ~3-fold than that for steam [200]), heat-integration achieves 85-90 % of energy savings.

5.2.3 Remarks on operation of conventional and heat-integrated columns

Distillation without heat integration is usually operated at high pressure (~15 bar) so that cooling water can be utilized for condenser, and this configuration is commonly known as high-pressure system [284]. The column design with heat integration is usually operated at lower pressure (~ 12 bar) as relative volatility is improved at lower pressure, and results in lower energy consumption. This external heat integrated configuration is commonly known as heat pump system [284]. While heat-integration through heat-pump achieves significant energy savings, such designs are challenging to operate and control due to reduction in available degrees of freedom [9,285], and, thus, are not routinely implemented

in industry. Further, low-grade heat (such as, quench water) is usually readily available as waste heat. Thus, high-pressure designs are more commonly used, and are usually heat-integrated with other parts of the plant for providing reboiler heating duty [284]. Although such designs may not be as energy-efficient as heat pump, they still result in energy savings without the additional control and operating challenges.

5.3 Separation using membranes

Several membrane materials have been studied for olefin/paraffin separation. While polymer membranes have been unable to achieve high selectivity [286–288], facilitated transport membranes [289], carbon molecular sieves [290,291], and zeolites and metal-organic framework membranes [292] have shown promising results.

5.3.1 Literature review

Facilitated transport membranes improve the olefin/paraffin selectivity by utilizing carriers, usually silver ions, which act as complexing agent and reversibly react with olefin molecules to improve their permeation over paraffin molecules [289]. These membranes can be broadly classified into liquid membranes and membrane electrolytes. However, liquid membranes suffers from the physical loss of facilitation carriers and thus cannot sustain high pressure operations. Further, both the feed and sweep streams need to be humidified with subsequent dehydration of product stream. Thus, dense membrane electrolyte are preferred over liquid membranes. Major work on polymer electrolyte membranes have been carried out by Sridhar and co-workers [293,294], Pinnau and co-workers [295,296], and Kang and co-workers [297–300]. Although permeance > 10 GPU and mixture selectivity > 100 has been achieved, Merkel et al. [301] have shown that exposure to light and presence of common mixture impurities, such as acetylene, hydrogen and hydrogen sulphide affects the carrier stability (reduces silver ion to silver particles)

and can reduce the selectivity by more than 10-fold within a period of 1 week. Although treatment with hydrogen perodixde/ tetrafluoroboric acid was suggested for restoration of these membranes, the process took a long time (~ 60 hours) for regeneration after hydrogen reduction and was ineffective against hydrogen sulphide poisoning.

Carbon membranes or carbon molecular sieves (CMS) are prepared by pyrolysis of polymer membranes at high temperature. Koros and co-workers [291,302,303] have extensively studied CMS membranes for olefin/paraffin separation. While both Matrimid and 6FDA/BPDA-DAM CMS membranes exhibited pure-gas selectivity (C_3H_6/C_3H_8) of > 20, polypropylene permeance of 18 GPU were obtained for 6FDA/BPDA-DAM CMS membranes as compared to 1 GPU for Matrimid CMS membranes. In other studies, Swaidan et al. [304] used polymer of intrinsic microposoristy, PIM-6FDA-OH, as a precursor for CMS membranes, which exhibited a mixed gas C_3H_6/C_3H_8 selectivity of 24 at 2 bar. However, the selectivity dropped to 17 as the feed pressure was raised to 5 bar. Ma et al. [290] studied the effect of substrates on the performance of CMS membranes and found that the membranes prepared on gamma-alumina substrate performed better than the ones prepared on alpha-alumina. They obtained a mixed gas-selectivity of 36 and polypropylene permeance of 9 GPU for 6FDA-based CMS membranes on gamma-alumina support. Researchers from Dow Chemicals [305] have used CMS as adsorbents for Pressure Swing Adsorption (PSA) process and achieved 90 mol% propylene from a 25 mol% propylene feed exhibiting a separation factor of 27.

Recently, Ma et al. have prepared ZIF-8 membranes using a novel ligand-induced permselectivation which shows promising and stable performance with high mixture separation factor for propylene over propane, and the highest propylene flux reported (larger than 45 and 10^{-2} mol m^{-2} s^{-1}, respectively, at room temperature and 7 atm equimolar

feed). In this research, propane-propylene separation is analyzed at a process-scale considering the performance achieved by these ZIF-8 membranes.

5.3.2 Membrane modeling

A counter-current membrane model with a constant permeance and selectivity, and a plug flow for both the retentate and the permeate side is considered. A uniform pressure was assumed on both the sides. The governing flow equations for each component are as follows:

$$-\frac{dF_{\mathrm{i}}}{dx} = \pm 2\pi r J_{\mathrm{i}} \tag{5.1}$$

where the +ve sign refers to the retentate side while the -sign refers to the permeate side, F is the flow rate along the membrane, J is the flux through the membrane, and r is the radius of the tube. The flux through the membrane is given by:

$$\begin{aligned} J_{\mathrm{i}} &= \Pi_i \left(p_{i,ret} - p_{i,perm} \right); \\ Sel_{i,j} &= \Pi_i / \Pi_j \end{aligned} \tag{5.2}$$

where Π refers to the permeance, p refers to the partial pressure, and *sel* refers to the selectivity, while 'ret' and 'perm' denote the retentate and permeate side, respectively.

The transport through these membranes is an adsorption-diffusion phenomenon and the selectivity values mentioned above for several kind of membranes are obtained at a feed pressure of 2-5 bar and a permeate pressure of < 1 bar. Since adsorption isotherm achieves saturation at high pressure, the driving force does not increase for feed pressure over the saturation pressure. Further, the driving force becomes negligible if permeate pressure is close to or higher than saturation, and the membrane becomes non-selective. In most of the membrane modeling studies in the literature, a permeate pressure of 3-5 bar is considered. Although this helps in reducing the energy enquired for permeate recompression to feed

pressure (~15 bar), it is impractical as the membranes will show negligible selectivity under such conditions.

5.3.3 Membrane permeation

In this study, the total permeate pressure is maintained at 1 bar in the model. Further, as the driving force saturates with pressure, the area was calculated considering a maximum total pressure of 5 bar on the feed side, i.e., the flux is considered constant for pressure over 5 bar on the feed side. Propylene purity against recovery obtained using a single-stage membrane model at several selectivity values for a feed specified in **Table 5.1** are shown in **Figure 5.2a**.

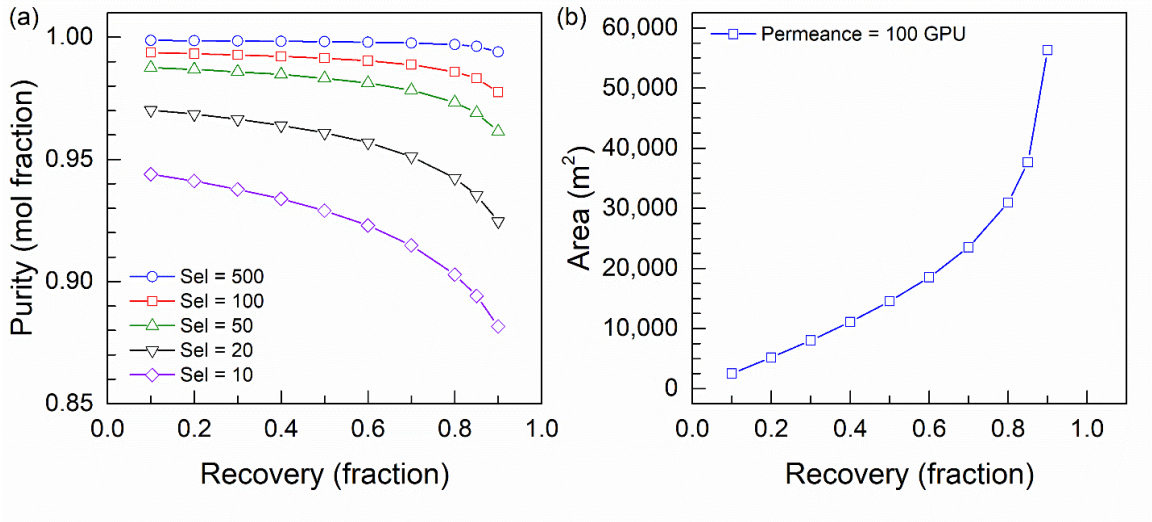

Figure 5.2: (a) Propylene purity obtained, and **(b)** membrane area required for increasing recovery obtained using a single-stage membrane model for 70.0 mol % propylene feed.

As shown, a maximum recovery of only 0.9 is feasible as driving force for propylene permeation becomes zero for recovery > 0.9. For a selectivity as high as 500 and propylene recovery of 0.9, propylene purity obtained from the single-stage membrane is 99.4 mol %. Although this is similar to polymer grade propylene (99.7 mol %) achieved in distillation process, the corresponding propane purity is only 81 mol % as opposed to 99 mol % obtained via distillation. Thus, high selectivity (> 500) membranes are required for

complete replacement of the column. Further, the area required for the process is determined to be > 55,000 m^2 (**Figure 5.2b**) for a permeance of 100 GPU. For recovery > 0.8, the driving force for propylene permeation becomes extremely small and leads to an abrupt increase in the membrane area; almost similar area is required to recover the last 10 % of propylene (from 80 to 90 %) as required to recover the first 80 %. For membrane area of 50,000 m^2 and an installed cost of \$500/m^2, the capital expenditure will exceed 25 million USD. Thus, even with a ~5-fold improvement in permeance or similar cost reduction that will breakeven with distillation capital cost, membrane separation results in lower recovery of propylene (or lower purity of propane). Since membrane shows good separation for intermediate recovery values even with reasonable selectivity of ~50, a hybrid membrane-distillation process is evaluated next.

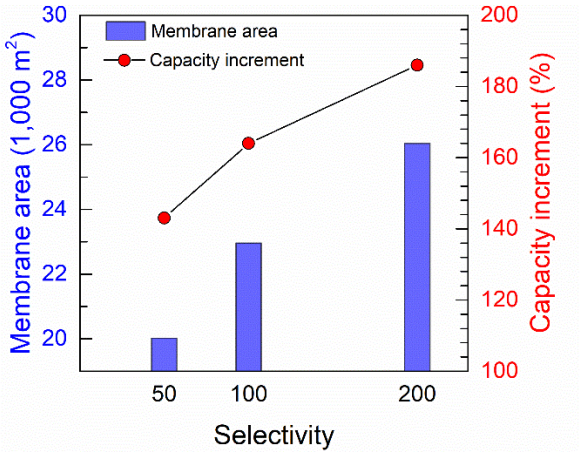

Figure 5.3: Membrane area required and capacity increment for propylene-propane separation obtained by membrane-distillation hybrid over distillation column shown for several membrane selectivity values.

5.4 Separation using hybrid membrane-distillation

A series configuration for hybrid membrane/distillation is considered [239]. A membrane stage-cut of 0.5 and selectivity values of 50, 100 and 200 are considered. The membrane stage cut is defined as the ratio of propylene (preferentially permeating

component) flow rate in the permeate stream to that in the feed, and is equal to the recovery. As membranes perform a part of the separation, the separation load on distillation is decreased leading to reduction in reflux and boilup ratio. To maintain the same vapor and liquid flowrate within the column, i.e., to use the same diameter column, the capacity of the existing column would be increased by implementing hybrid membrane-distillation. The increase in capacity for different selectivity values are shown in **Figure 5.3** which suggests a 1.5 to 2-fold increment for selectivity of 50 to 200.

The operational and capital expenses are also analyzed. While the reduction in reboiler duty reduces the energy requirement, the permeate compression results in additional operating expenses. However, the hybrid configuration results in net energy savings even for columns with up to 80% heat integration (i.e. 80% of reboiler duty is provided by heat-integration). The operating and capital expenses and savings varying with increment in heat-integration are shown in **Figure 5.4** for selectivity of 50, 100 and 200. Even for 50% heat-integrated column (50% of reboiler duty provided by heat-integration), membranes with selectivity of 50 can achieve > 30% savings in energy requirement over heat-integrated distillation. This corresponds to a savings of 0.38 cents/kg of propylene. For reference, the operational cost of a 50% heat-integrated column is 1.5 cents/kg and the cost of propylene is 65 cents/kg [306]. Although the savings are < 1% of the current price, considering the current annual production of propylene at 50 million tonnes [262,307], it can save ~ 200 million USD annually if implemented throughout the industry.

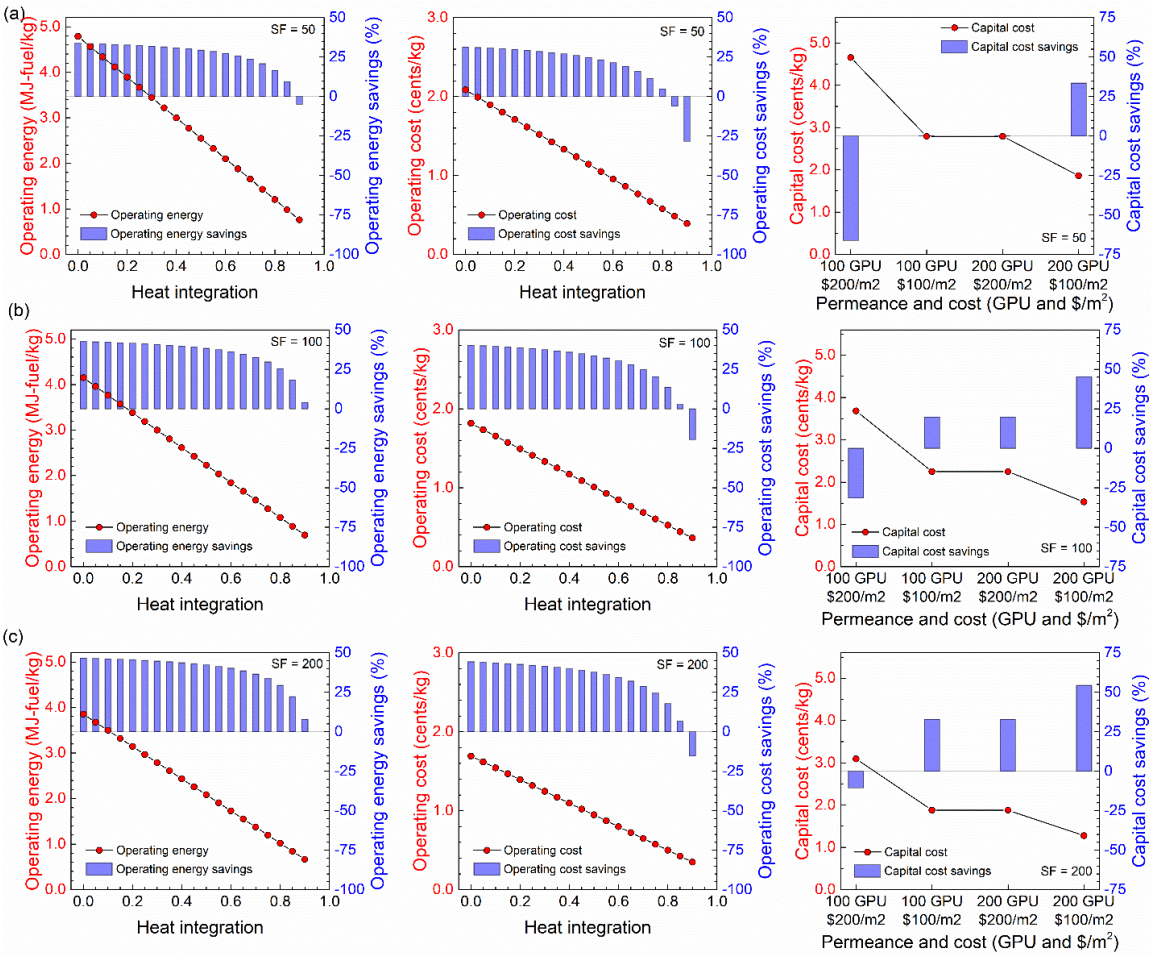

Figure 5.4: Operational and capital expenses and savings for propylene-propane separation by membrane-distillation hybrid over heat-integrated distillation column for a membrane exhibiting a selectivity of (a) 50, (b) 100 and (b) 200. Results are shown against the heat-integrated fraction which represents the amount of energy provided by heat-integration.

The additional capital cost (comprises of the membrane cost and the compressor) for capacity increment is also calculated and compared to the capital expenses for base-case distillation. The capital cost of base case distillation achieving an annual production of 250,000 tons of propylene is 7 million USD (2.80 cents/kg). For membranes exhibiting a selectivity of 50, the area required for a permeance of 100 GPU is calculated to be ~20,000 m^2 for a plant producing 250,000 tonnes/year of propylene (**Figure 5.3**), and a breakeven in capital cost can be achieved at a membrane cost of \$100/m^2. Even more favorable results

(savings of 37% in operational cost and 54% in capital cost) can be achieved at improved membrane performance with a selectivity of 200 and a permeance of 200 GPU.

5.5 Recovery from reactor purge

Another attractive potential use of the propylene selective membranes, is the recovery of propylene that is lost in the purging process in polymerization plants. In such applications, a stream of 70-90 mol % propylene (shown as separator recycle in **Figure 5.5a**) is normally recycled back to the reactor [272,280,308].

To prevent build-up of propane, a part of this is purged (shown as separator purge) and results in propylene losses. Although separator purge is a small fraction of the feed (and/or separator recycle stream), it contains substantial amount of propylene (~5 million lb per polymerization plant annually) and can lead to considerable profits if recovered even up to 90 %. considering the polypropylene production of > 50 million tonnes/year [309], the lost propylene is worth > 200 million USD annually. The membrane separation has been proposed as a potential solution to recover this propylene and recycle it back to the reactor. Although the feed to the reactor is polymer-grade (~ 99.7 mol %), 80-95 mol % permeate recycle has been found to be adequate [280,308]. This is because the separator recycle stream is 70-90 mol % and thus the overall composition in reactor is lower than the polymer grade feed. Further, the permeate recycle is only a small fraction of the total feed (fresh feed + separator recycle + permeate recycle) and only has a marginal effect on the total composition.

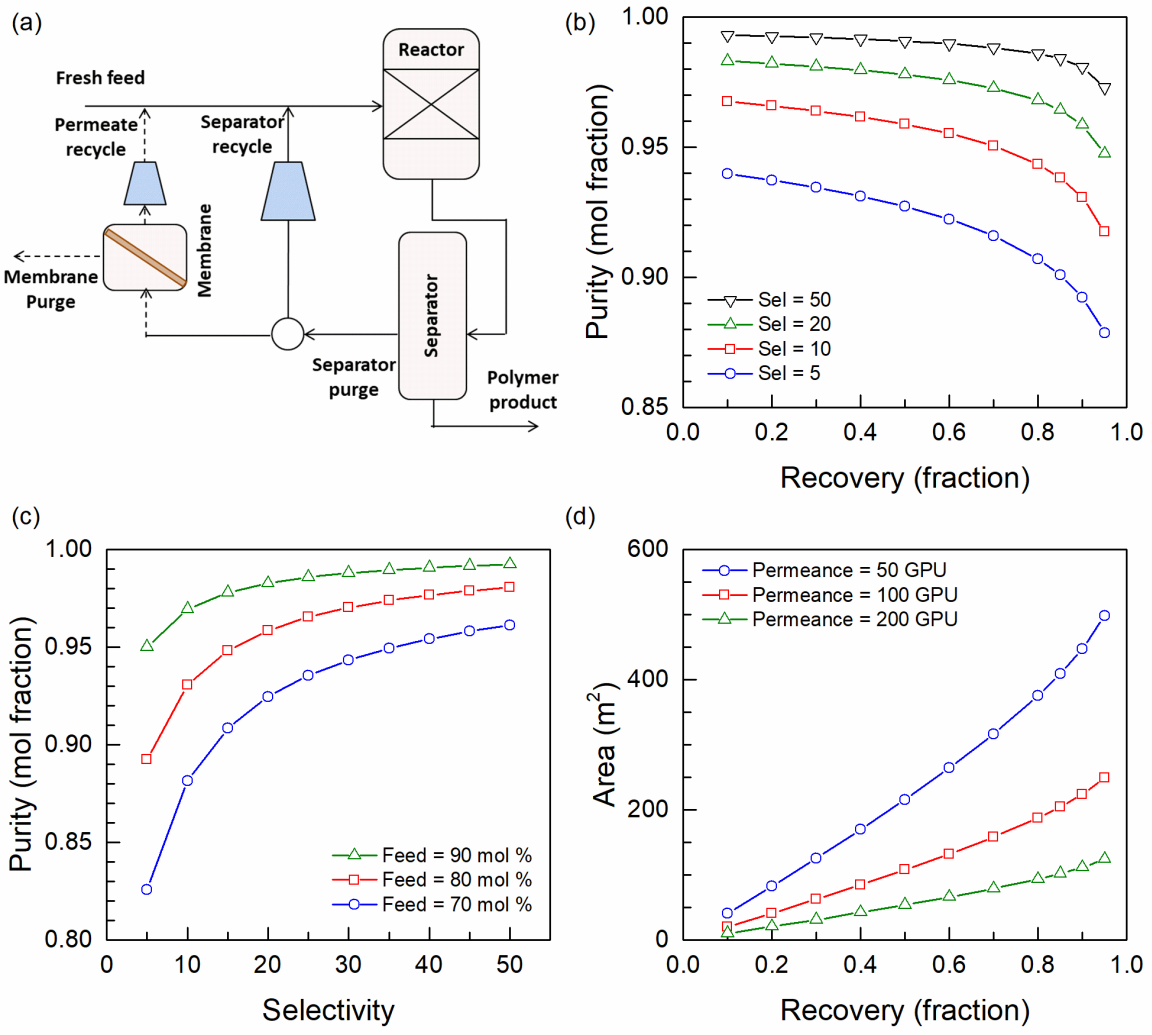

Figure 5.5: (a) Schematic of membrane retrofitting in a reactor purge stream. The original reactor configuration is shown with solid lines and the membrane retrofitting part is shown with dashed lines. **(b)** Propylene purity against recovery obtained using a single-stage membrane model for 80.0 mol % propylene feed at several values of selectivity. **(c)** Propylene purity against selectivity obtained using a single-stage membrane model for 90.0 % recovery shown for several feed compositions. **(d)** Membrane area required for 80 mol % propylene feed at a total flowrate of 2.6 mol/s. For a recovery of 90 %, this would correspond to 5 million lb propylene annually.

As moderate purity is adequate for this application, separation by membranes can be performed in a single-stage at reasonable selectivity. The results obtained for propylene purity against recovery for several values of selectivity, and propylene purity against selectivity for several values of feed composition are shown in **Figure 5.5b** and **5.5c**, respectively. As shown, even for a 70 mol % feed, 90 % propylene can be recovered at >

80 mol % purity for selectivity as low as 5. The membrane area required for 80 mol % propylene feed at 2.6 mol/s (equivalent to 5 million lb propylene annually at a recovery of 90 %) is shown in **Figure 5.5d**. As shown, for a permeance of 100 GPU, membrane area of ~250 m^2 will be required for a typical propylene polymerization reactor.

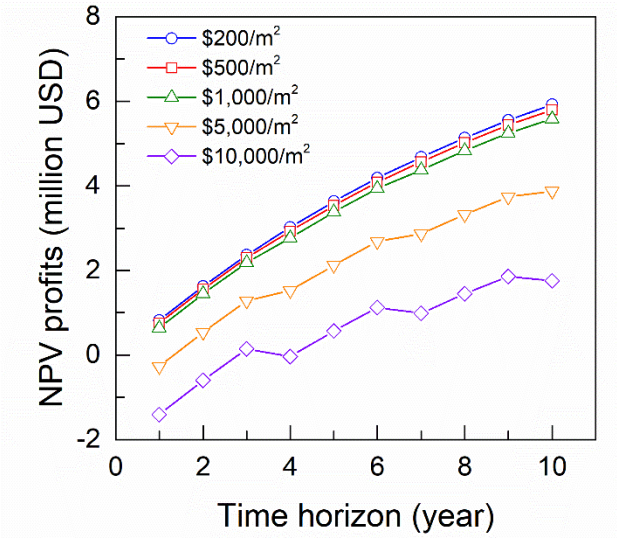

Figure 5.6: Net present value of profits for 90 % propylene recovery from a reactor purge stream considering reactor pressure of 30 bar, annual propylene recovery of 5 million lb, and membrane permeance and selectivity of 100 GPU and 5, respectively.

An economic analysis is also carried out to evaluate the profits associated with purge stream recovery. As the reactor is operated at high pressure (5 – 30 bar) [310–312], compression of the permeate stream will constitute majority of the operational cost. The major capital cost will comprise the cost of the compressor and the membrane. This cost, then, shall be compared to the value of recovered olefin to evaluate the scope of membranes for this application. Considering a price of 20 cents/lb for propylene [306], the total annual revenue for a recovery of 5 million lb propylene per year amounts to $ 1 million. Correspondingly, three compressors of < 10 kW each are required for permeate compression to 30 bar. Considering a cost of 7 cents/kWh of electrical energy [200], this amounts to $17,000 in operational costs which is < 2% of the total revenue. The corresponding total capital cost for compressor and membrane amounts to $30,000 and

$125,000 (considering installed membrane cost of $500/m^2), respectively. This results in a payback of < 1 year with > 5-fold return in the first year itself. A net present value analysis (NPV) is also performed and the NPV profits are calculated at a discount rate of 10%. Furthermore, the membrane was assumed to have a lifetime of 3 years and to cost 50 % of the initial investment when replaced. NPV profits over a period of 10 years are shown in **Figure 5.6**, which suggests significant benefits of using membranes for reactor purge application.

5.6 Conclusion

The application of membranes for propylene/propane separation is evaluated considering both stand-alone and hybrid membrane-distillation configurations. We found that high membrane selectivity of > 500, and implementation of multi-stage cascade design is required for stand-alone membrane system. These conclusions are also in agreement to the other studies in the literature. While distillation is difficult to be replaced using membranes, a hybrid membrane-distillation combination is attractive for debottlenecking of existing distillation columns. Another attractive potential use of the propylene selective membranes, is the recovery of propylene that is lost in the purging process in polymerization plants, which is estimated in excess of 5,000,000 lb with a corresponding value of $1 million, per year, per polymerization plant [272,280,308]. A payback period of < 3 years and annual savings of ~1 million USD can be achieved for a typical polymerization plant with a permeance of 100 GPU and a selectivity of 5. Compared to C3 splitter, the reactor purge application employs smaller area (100-fold lesser) and can correspondingly incur higher cost. Thus, membranes for reactor purge application can be industrialized at current membrane performance, while improved membrane performance or corresponding cost reduction is required for implementing C3 splitter application.

Chapter 6: Concluding remarks

The aim of this thesis is to develop a detailed mathematical model of a zeolite membrane separation process and use this to perform conceptual process design studies and techno-economic evaluation for several applications of interest, including butane isomer separation, bioethanol enrichment, and propylene-propane separation. A comprehensive model has been developed that not only predicts the separation performance under wide range of operating conditions, but also determines the scope of improvement in the current state-of-the-art membranes. In this model, permeation through the zeolite membrane is described using molecular-level adsorption-diffusion properties including resistances from external resistances. This is integrated with a process-level model which results in complete description of membrane operation, both at the microscopic and macroscopic level. This first-of-its-kind modeling approach can be used as a template to rigorously design and optimize zeolite membrane systems, as illustrated using several applications. The conclusion realized by applying the model for these applications are discussed next.

For butane isomer application, a hybrid membrane-distillation process is found to be energy efficient and economically attractive over stand-alone membrane separation. A 10-fold improvement in diffusivity ($Đ = Đ_0/5$) can be achieved by reducing pore blockages in the intergrown membranes or, equivalently, its effect on performance can be achieved by reducing the membrane thickness from the currently achieved ~500 nm to 50 nm or less. With this 10-fold improvement in permeance as compared to that in current state-of-the-art ceramic supported MFI membranes, payback period of 3 years can be achieved with installed membrane cost of up to \$5,000/m^2. Alternatively, the same payback period can be achieved by the current technology if manufacturing improvements bring the membrane cost down to \$500/m^2.

For bioethanol enrichment, both hydrophilic and hydrophobic zeolite membranes have been considered. It is found that hydrophobic zeolite membranes have potential for significant energy savings but a 2-fold improvement in selectivity over that exhibited by defect-free membranes is required to meet distillation purity. Hydrophilic zeolite membranes can achieve higher purity than distillation but consume almost similar energy as that required for distillation. Thus, a configuration that uses hydrophobic membranes followed by hydrophilic membranes is considered which can achieve the required purity with 10 % energy savings over distillation. The techno-economic analysis suggests that defect-free membranes and ~ 10-fold improvements in permeation or equivalent cost reductions are required for economic viability of this scheme. Considering these intensive requirements, zeolite membranes offer only a marginal amount of savings and, thus, is not a promising application for bioethanol enrichment.

ZEF-8 (Zeolitic Imidazolate Framework) membranes have been considered for propylene-propane application. While distillation is difficult to be replaced using membranes, a hybrid membrane-distillation is attractive for debottlenecking of existing distillation columns. This can result in operational savings of ~ 200 million USD annually if implemented throughout the industry but a cost of \$100/m^2 along with a membrane area of 20,000 m^2 is required to achieve a breakeven in the capital cost. Another attractive potential use of the propylene selective membranes, is the recovery of propylene that is lost in the purging process in polymerization plants. Compared to C3 splitter, the reactor purge application employs smaller area (100-fold lesser) and can correspondingly incur higher cost (up to \$10,000/m^2). Thus, membranes for reactor purge application can be industrialized at current membrane performance, while improved membrane performance or corresponding cost reduction is required for implementing C3 splitter application.

Bibliography

[1] Distillation Column Modeling Tools, Office of Industrial Technologies, Energy Efficiency and Renewable Energy, U.S. Department of Energy, 2001.

[2] N. Rangnekar, N. Mittal, B. Elyassi, J. Caro, M. Tsapatsis, Zeolite membranes – a review and comparison with MOFs, Chem. Soc. Rev. 44 (2015) 7128–7154. doi:10.1039/C5CS00292C.

[3] Hybrid Separations/Distillation Technology Industrial Technologies Program, Office of Energy Efficiency and Renewable Energy, U.S. Department of Energy, 2005.

[4] R. Krishna, L.J.P. van den Broeke, The Maxwell-Stefan description of mass transport across zeolite membranes, Chem. Eng. J. Biochem. Eng. J. 57 (1995) 155–162. doi:10.1016/0923-0467(94)02951-2.

[5] F. Kapteijn, J.A. Moulijn, R. Krishna, The generalized Maxwell-Stefan model for diffusion in zeolites: Sorbate molecules with different saturation loadings, Chem. Eng. Sci. 55 (2000) 2923–2930. doi:10.1016/S0009-2509(99)00564-3.

[6] Butanes Market - Global Industry Size, Market Share, Trends, Analysis, and Forecasts 2010 – 2018, Transparency Market Research, 2011.

[7] J. Kärger, D.M. Ruthven, D.N. Theodorou, Diffusion in nanoporous materials, John Wiley & Sons, 2012.

[8] Ž. Olujić, L. Sun, A. de Rijke, P.J. Jansens, Conceptual design of an internally heat integrated propylene-propane splitter, Energy. 31 (2006) 3083–3096. doi:10.1016/j.energy.2006.03.030.

[9] S.S. Jogwar, P. Daoutidis, Dynamics and control of vapor recompression distillation, J. Process Control. 19 (2009) 1737–1750. doi:10.1016/j.jprocont.2009.07.001.

[10] J. Caro, M. Noack, P. Kölsch, R. Schäfer, Zeolite membranes - state of their development and perspective, Microporous Mesoporous Mater. 38 (2000) 3–24. doi:10.1016/S1387-1811(99)00295-4.

[11] J. Caro, M. Noack, Zeolite membranes - Recent developments and progress, Microporous Mesoporous Mater. 115 (2008) 215–233. doi:10.1016/j.micromeso.2008.03.008.

[12] M. Tsapatsis, Toward high-throughput zeolite membranes, Science. 334 (2011) 767–768. doi:10.1126/science.1205957.

[13] J. Gascon, F. Kapteijn, B. Zornoza, V. Sebastián, C. Casado, J. Coronas, Practical approach to zeolitic membranes and coatings: State of the art, opportunities, barriers, and future perspectives, Chem. Mater. 24 (2012) 2829–2844. doi:10.1021/cm301435j.

[14] S.-L. Wee, C.-T. Tye, S. Bhatia, Membrane separation process—Pervaporation through zeolite membrane, Sep. Purif. Technol. 63 (2008) 500–516. doi:10.1016/J.SEPPUR.2008.07.010.

[15] Z. Lai, G. Bonilla, I. Diaz, J.G. Nery, K. Sujaoti, M.A. Amat, E. Kokkoli, O. Terasaki, R.W. Thompson, M. Tsapatsis, D.G. Vlachos, Microstructural optimization of a zeolite membrane for organic vapor separation, Science. 300 (2003) 456–460. doi:10.1126/science.1082169.

[16] M. Yu, R.D. Noble, J.L. Falconer, Zeolite membranes: Microstructure characterization and permeation mechanisms, Acc. Chem. Res. 44 (2011) 1196–1206. doi:10.1021/ar200083e.

[17] J.A. Stoeger, J. Choi, M. Tsapatsis, Rapid thermal processing and separation performance of columnar MFI membranes on porous stainless steel tubes, Energy Environ. Sci. View. 4 (2011) 3479–3486. doi:10.1039/c1ee01700d.

[18] Y. Peng, H. Lu, Z. Wang, Y. Yan, Microstructural optimization of MFI-type zeolite membranes for ethanol–water separation, J. Mater. Chem. A Mater. Energy Sustain. 2 (2014) 16093–16100. doi:10.1039/C4TA02837F.

[19] K. Varoon, X. Zhang, B. Elyassi, D.D. Brewer, M. Gettel, S. Kumar, J.A. Lee, S. Maheshwari, A. Mittal, C.Y. Sung, M. Cococcioni, L.F. Francis, A. V. McCormick, K.A. Mkhoyan, M. Tsapatsis, Dispersible exfoliated zeolite nanosheets and their application as a selective membrane, Science. 334 (2011) 72–75. doi:10.1126/science.1208891.

[20] T.C.T. Pham, T.H. Nguyen, K.B. Yoon, Gel-free secondary growth of uniformly oriented silica MFI zeolite films and application for xylene separation, Angew. Chemie - Int. Ed. 52 (2013) 8693–8698. doi:10.1002/anie.201301766.

[21] Y. Li, W. Yang, Microwave synthesis of zeolite membranes: A review, J. Memb. Sci. 316 (2008) 3–17. doi:10.1016/J.MEMSCI.2007.08.054.

[22] N. Kosinov, J. Gascon, F. Kapteijn, E.J.M. Hensen, Recent developments in zeolite membranes for gas separation, J. Memb. Sci. 499 (2016) 65–79. doi:10.1016/J.MEMSCI.2015.10.049.

[23] T.C. Bowen, R.D. Noble, J.L. Falconer, Fundamentals and applications of pervaporation through zeolite membranes, J. Memb. Sci. 245 (2004) 1–33. doi:10.1016/j.memsci.2004.06.059.

[24] D. Korelskiy, T. Lepp, H. Zhou, M. Grahn, J. Tanskanen, J. Hedlund, High flux MFI membranes for pervaporation, J. Memb. Sci. 427 (2013) 381–389. doi:10.1016/j.memsci.2012.10.016.

[25] B. Huang, Q. Liu, J. Caro, A. Huang, Iso-butanol dehydration by pervaporation using zeolite LTA membranes prepared on 3-aminopropyltriethoxysilane-modified alumina tubes, J. Memb. Sci. 455 (2014) 200–206. doi:10.1016/j.memsci.2013.12.075.

[26] B. Elyassi, M.Y. Jeon, M. Tsapatsis, K. Narasimharao, N.M.N. Sulaiman, S. Al-Thabaiti, Ethanol/Water Mixture Pervaporation Performance of b-Oriented Silicalite-1 Membranes Made by Gel-Free Secondary Growth Bahman, AIChE J. 62 (2016) 556. doi:10.1002/aic.

[27] R.D. Noble, J.L. Falconer, Separations of C4 and C6 Isomers in ZSM-5 Tubular Membranes, Ind. Eng. Chem. Res. 37 (1998) 166–176. doi:10.1021/ie970462u.

[28] T. Matsufuji, N. Nishiyama, M. Matsukata, K. Ueyama, Separation of butane and xylene isomers with MFI-type zeolitic membrane synthesized by a vapor-phase transport method, J. Memb. Sci. 178 (2000) 25–34. doi:10.1016/S0376-7388(00)00462-2.

[29] S. Nair, Z. Lai, V. Nikolakis, G. Xomeritakis, G. Bonilla, M. Tsapatsis, Separation of close-boiling hydrocarbon mixtures by MFI and FAU membranes made by secondary growth, Microporous Mesoporous Mater. 48 (2001) 219-228. doi:10.1016/S1387-1811(01)00356-0.

[30] T. Lee, J. Choi, M. Tsapatsis, On the performance of c-oriented MFI zeolite Membranes treated by rapid thermal processing, J. Memb. Sci. 436 (2013) 79–89. doi:10.1016/j.memsci.2013.02.028.

[31] K.V. Agrawal, B. Topuz, T.C.T. Pham, T.H. Nguyen, N. Sauer, N. Rangnekar, H. Zhang, K. Narasimharao, S.N. Basahel, L.F. Francis, C.W. Macosko, S. Al-Thabaiti, M. Tsapatsis,

K.B. Yoon, Oriented MFI membranes by gel-less secondary growth of sub-100 nm MFI-nanosheet seed layers, Adv. Mater. 27 (2015) 3243–3249. doi:10.1002/adma.201405893.

[32] M.A. Carreon, S. Li, J.L. Falconer, R.D. Noble, Alumina-Supported SAPO-34 Membranes for CO_2/CH_4 Separation, J. Am. Chem. Soc. 130 (2008) 5412–5413. doi:10.1021/ja801294f.

[33] J.C. White, P.K. Dutta, K. Shqau, H. Verweij, Synthesis of Ultrathin Zeolite Y Membranes and their Application for Separation of Carbon Dioxide and Nitrogen Gases, Langmuir. 26 (2010) 10287–10293. doi:10.1021/la100463j.

[34] T. Tomita, K. Nakayama, H. Sakai, Gas separation characteristics of DDR type zeolite membrane, Microporous Mesoporous Mater. 68 (2004) 71–75. doi:10.1016/J.MICROMESO.2003.11.016.

[35] H. Zhou, D. Korelskiy, E. Sjöberg, J. Hedlund, Ultrathin hydrophobic MFI membranes, Microporous Mesoporous Mater. 192 (2014) 76–81. doi:10.1016/J.MICROMESO.2013.09.017.

[36] R. Krishna, Describing the diffusion of guest molecules inside porous structures, J. Phys. Chem. C. 113 (2009) 19756–19781. doi:10.1021/jp906879d.

[37] R. Krishna, Diffusion in porous crystalline materials, Chem. Soc. Rev. 41 (2012) 3099. doi:10.1039/c2cs15284c.

[38] J. Xiao, J. Wei, Diffusion mechanism of hydrocarbons in zeolites—I. Theory, Chem. Eng. Sci. 47 (1992) 1123–1141. doi:10.1016/0009-2509(92)80236-6.

[39] J. Xiao, J. Wei, Diffusion mechanism of hydrocarbons in zeolites—II. Analysis of experimental observations, Chem. Eng. Sci. 47 (1992) 1143–1159. doi:10.1016/0009-2509(92)80237-7.

[40] J. Coronas, J. Santamaría, Separations Using Zeolite Membranes, Sep. Purif. Methods. 28 (1999) 127–177. doi:10.1080/03602549909351646.

[41] D.S. Sholl, Understanding Macroscopic Diffusion of Adsorbed Molecules in Crystalline Nanoporous Materials via Atomistic Simulations, (2006). doi:10.1021/AR0402199.

[42] J.M. Van De Graaf, F. Kapteijn, J.A. Moulijn, Modeling permeation of binary mixtures through zeolite membranes, AIChE J. 45 (1999) 497–511. doi:10.1002/aic.690450307.

[43] A.I. Skoulidas, D.S. Sholl, R. Krishna, Correlation Effects in Diffusion of CH 4 /CF 4 Mixtures in MFI Zeolite. A Study Linking MD Simulations with the Maxwell−Stefan Formulation, Langmuir. 19 (2003) 7977–7988. doi:10.1021/la034759a.

[44] T.Q. Gardner, J.L. Falconer, R.D. Noble, Transient permeation of butanes through ZSM-5 and ZSM-11 zeolite membranes, AIChE J. 50 (2004) 2816–2834. doi:10.1002/aic.10217.

[45] R. Krishna, J.M. van Baten, A simplified procedure for estimation of mixture permeances from unary permeation data, J. Memb. Sci. 367 (2011) 204–210. doi:10.1016/j.memsci.2010.10.055.

[46] Y.F. Yeong, A.Z. Abdullah, A.L. Ahmad, S. Bhatia, Process optimization studies of p-xylene separation from binary xylene mixture over silicalite-1 membrane using response surface methodology, J. Memb. Sci. 341 (2009) 96–108. doi:10.1016/j.memsci.2009.05.042.

[47] T. Leppäjärvi, I. Malinen, D. Korelskiy, J. Hedlund, J. Tanskanen, Maxwell-stefan modeling of ethanol and water unary pervaporation through a high-silica MFI zeolite membrane, Ind. Eng. Chem. Res. 53 (2014) 323–332. doi:10.1021/ie400814z.

[48] A.M. Tarditi, E.A. Lombardo, A.M. Avila, Xylene permeation transport through composite Ba-ZSM-5/SS tubular membranes: Modeling the steady-state permeation, Ind. Eng. Chem. Res. 47 (2008) 2377–2385. doi:10.1021/ie071296l.

[49] R. Krishna, J.M. van Baten, Highlighting pitfalls in the Maxwell-Stefan modeling of water-alcohol mixture permeation across pervaporation membranes, J. Memb. Sci. 360 (2010) 476–482. doi:10.1016/j.memsci.2010.05.049.

[50] R. Krishna, J.M. Van Baten, Hydrogen bonding effects in adsorption of water-alcohol mixtures in zeolites and the consequences for the characteristics of the Maxwell-Stefan diffusivities, Langmuir. 26 (2010) 10854–10867. doi:10.1021/la100737c.

[51] R. Krishna, J.M. van Baten, Maxwell-Stefan modeling of slowing-down effects in mixed gas permeation across porous membranes, J. Memb. Sci. 383 (2011) 289–300. doi:10.1016/j.memsci.2011.08.067.

[52] P. Bai, M. Tsapatsis, J.I. Siepmann, Multicomponent adsorption of alcohols onto silicalite-1 from aqueous solution: Isotherms, structural analysis, and assessment of ideal adsorbed solution theory, Langmuir. 28 (2012) 15566–15576. doi:10.1021/la303247c.

[53] L. Lu, Y. Zhu, X. Wu, S. Wang, W. Cao, X. Lu, Adsorption of N-Butane/I-Butane in Zeolites: Simulation and Theory Study, Sep. Sci. Technol. 49 (2014) 1215–1226. doi:10.1080/01496395.2013.878848.

[54] S. Brandani, M. Jama, D.M. Ruthven, Counterdiffusion of p-Xylene/Benzene and p-Xylene/o-Xylene in Silicalite Studied by the Zero-Length Column Technique, (2000). doi:10.1021/IE990691B.

[55] R. Krishna, J.A. Wesselingh, The Maxwell-Stefan approach to mass transfer, Chem. Eng. Sci. 52 (1997) 861–911.

[56] R. Krishna, R. Baur, Modelling issues in zeolite based separation processes, Sep. Purif. Technol. 33 (2003) 213–254. doi:10.1016/S1383-5866(03)00008-X.

[57] R. Krishna, The Maxwell-Stefan description of mixture diffusion in nanoporous crystalline materials, Microporous Mesoporous Mater. 185 (2014) 30–50. doi:10.1016/j.micromeso.2013.10.026.

[58] F.J. Keil, R. Krishna, M.O. Coppens, Modeling of Diffusion in Zeolites, Rev. Chem. Eng. 16 (2000). doi:10.1515/REVCE.2000.16.2.71.

[59] A.I. Skoulidas, D.S. Sholl, Multiscale models of sweep gas and porous support effects on zeolite membranes, AIChE J. 51 (2005) 867–877. doi:10.1002/aic.10335.

[60] T.J.H. Vlugt, R. Krishna, B. Smit, Molecular Simulations of Adsorption Isotherms for Linear and Branched Alkanes and Their Mixtures in Silicalite, J. Phys. Chem. B. 103 (1999) 1102–1118. doi:10.1021/jp982736c.

[61] P.F. Lito, A.S. Santiago, S.P. Cardoso, B.R. Figueiredo, C.M. Silva, New expressions for single and binary permeation through zeolite membranes for different isotherm models, J. Memb. Sci. 367 (2011) 21–32. doi:10.1016/j.memsci.2010.10.034.

[62] R. Krishna, D. Paschek, Permeation of Hexane Isomeres Across ZSM--5 Zeolite Membranes, Ind. Eng. Chem. Res. 39 (2000) 2618–2622.

[63] A.L. Myers, J.M. Prausnltz, Thermodynamics of mixed-gas adsorption, AIChE J. 11 (1965) 121–127. doi:10.1002/aic.690110125.

[64] R. Krishna, D. Paschek, Separation of hydrocarbon mixtures using zeolite membranes: a

modelling approach combining molecular simulations with the Maxwell-Stefan theory, Sep. Purif. Technol. 21 (2000) 111–136. doi:10.1016/S1383-5866(00)00196-9.

[65] D.P. Valenzuela, A.L. Myers, O. Talu, I. Zwiebel, Adsorption of gas mixtures: Effect of energetic heterogeneity, AIChE J. 34 (1988) 397–402. doi:10.1002/aic.690340306.

[66] O. Talu, I. Zwiebel, Spreading pressure dependent equation for adsorbate phase activity coefficients, React. Polym. Ion Exch. Sorbents. 5 (1987) 81–91. doi:10.1016/0167-6989(87)90168-1.

[67] E. Costa, J.L. Sotelo, G. Calleja, C. Marrón, Adsorption of binary and ternary hydrocarbon gas mixtures on activated carbon: Experimental determination and theoretical prediction of the ternary equilibrium data, AIChE J. 27 (1981) 5–12. doi:10.1002/aic.690270103.

[68] E. Costa, G. Calleja, C. Marron, A. Jimenez, J. Pau, Equilibrium Adsorption of Methane, Ethane, Ethylene, and Propylene and Their Mixtures on Activated Carbon, J. Chem. Eng. Data. 34 (1989) 156–160. doi:Doi 10.1021/Je00056a003.

[69] S. Sochard, N. Fernandes, J.-M. Reneaume, Modeling of Adsorption Isotherm of a Binary Mixture with Real Adsorbed Solution Theory and Nonrandom Two-Liquid Model Sabine, AIChE J. 56 (2010) 3109. doi:10.1002/aic.

[70] A. Erto, A. Lancia, D. Musmarra, A Real Adsorbed Solution Theory model for competitive multicomponent liquid adsorption onto granular activated carbon, Microporous Mesoporous Mater. 154 (2012) 45–50. doi:10.1016/j.micromeso.2011.10.041.

[71] M. Mofarahi, F. Gholipour, Gas adsorption separation of CO2/CH4 system using zeolite 5A, Microporous Mesoporous Mater. 200 (2014) 1–10. doi:10.1016/j.micromeso.2014.08.022.

[72] R. Krishna, J.M. Van Baten, S. Calero, C. De Utrera, Incorporating the Loading Dependence of the Maxwell - Stefan Diffusivity in the Modeling of CH4 and CO2 Permeation Across Zeolite Membranes, Ind. Eng. Chem. Res. (2007) 2974–2986.

[73] R. Krishna, J.M. van Baten, Insights into diffusion of gases in zeolites gained from molecular dynamics simulations, Microporous Mesoporous Mater. 109 (2008) 91–108. doi:10.1016/j.micromeso.2007.04.036.

[74] R. Krishna, J.M. Van Baten, Linking the loading dependence of the Maxwell-Stefan diffusivity of linear alkanes in zeolites with the thermodynamic correction factor, Chem. Phys. Lett. 420 (2006) 545–549. doi:10.1016/j.cplett.2006.01.039.

[75] C. Chmelik, L. Heinke, J. Kärger, W. Schmidt, D.B. Shah, J.M. van Baten, R. Krishna, Inflection in the loading dependence of the Maxwell-Stefan diffusivity of iso-butane in MFI zeolite, Chem. Phys. Lett. 459 (2008) 141–145. doi:10.1016/j.cplett.2008.05.023.

[76] R. Krishna, J.M. van Baten, Influence of adsorption thermodynamics on guest diffusivities in nanoporous crystalline materials, Phys. Chem. Chem. Phys. 15 (2013) 7994. doi:10.1039/c3cp50449b.

[77] D.P. and, R. Krishna, Diffusion of Binary Mixtures in Zeolites: Kinetic Monte Carlo versus Molecular Dynamics Simulations, (2000). doi:10.1021/LA000695H.

[78] R. Krishna, J.M. van Baten, Unified Maxwell-Stefan description of binary mixture diffusion in micro- and meso-porous materials, Chem. Eng. Sci. 64 (2009) 3159–3178. doi:10.1016/j.ces.2009.03.047.

[79] D.M. Ruthven, M. Eic, E. Richard, Diffusion of C8 aromatic hydrocarbons in silicalite, Zeolites. 11 (1991) 647–653. doi:10.1016/S0144-2449(05)80166-6.

[80] S. Brandani, M. Jama, D. Ruthven, Diffusion, self-diffusion and counter-diffusion of benzene and p-xylene in silicalite, Microporous Mesoporous Mater. 35–36 (2000) 283–300. doi:10.1016/S1387-1811(99)00228-0.

[81] G. Xomeritakis, S. Nair, M. Tsapatsis, Transport properties of alumina-supported MFI membranes made by secondary (seeded) growth, Microporous Mesoporous Mater. 38 (2000) 61–73. doi:10.1016/S1387-1811(99)00300-5.

[82] J.B. Lee, H.H. Funke, R.D. Noble, J.L. Falconer, Adsorption-induced expansion of defects in MFI membranes, J. Memb. Sci. 341 (2009) 238–245. doi:10.1016/j.memsci.2009.06.011.

[83] R. Krishna, J.M. van Baten, Diffusion of hydrocarbon mixtures in MFI zeolite: Influence of intersection blocking, Chem. Eng. J. 140 (2008) 614–620. doi:10.1016/j.cej.2007.11.026.

[84] K. Zhang, R.P. Lively, M.E. Dose, L. Li, W.J. Koros, D.M. Ruthven, B.A. McCool, R.R. Chance, Diffusion of water and ethanol in silicalite crystals synthesized in fluoride media, Microporous Mesoporous Mater. 170 (2013) 259–265. doi:10.1016/j.micromeso.2012.12.015.

[85] K. Zhang, R.P. Lively, C. Zhang, W.J. Koros, R.R. Chance, Investigating the Intrinsic Ethanol / Water Separation Capability of ZIF-8 : An Adsorption and Di ff usion Study, J. Phys. Chem. C. 117 (2013) 7214–7225.

[86] K. Zhang, R.P. Lively, M.E. Dose, A.J. Brown, C. Zhang, J. Chung, S. Nair, W.J. Koros, R.R. Chance, Alcohol and water adsorption in zeolitic imidazolate frameworks, Chem. Commun. 49 (2013) 3245. doi:10.1039/c3cc39116g.

[87] S.K. Wirawan, D. Creaser, J. Lindmark, J. Hedlund, I.M. Bendiyasa, W.B. Sediawan, H2/CO2permeation through a silicalite-1 composite membrane, J. Memb. Sci. 375 (2011) 313–322. doi:10.1016/j.memsci.2011.03.061.

[88] J. Shao, Z. Zhan, J. Li, Z. Wang, K. Li, Y. Yan, Zeolite NaA membranes supported on alumina hollow fibers: Effect of support resistances on pervaporation performance, J. Memb. Sci. 451 (2014) 10–17. doi:10.1016/j.memsci.2013.09.049.

[89] J.M. Van De Graaf, F. Kapteijn, J.A. Moulijn, Methodological and operational aspects of permeation measurements on silicalite-1 membranes, J. Memb. Sci. 144 (1998) 87–104. doi:10.1016/S0376-7388(98)00032-5.

[90] J.M. Van De Graaf, E. Van Der Bijl, A. Stol, F. Kapteijn, J.A. Moulijn, Effect of operating conditions and membrane quality on the separation performance of composite silicalite-1 membranes, Ind. Eng. Chem. Res. 37 (1998) 4071–4083. doi:10.1021/ie980250c.

[91] H. Li, U. Schygulla, J. Hoffmann, P. Niehoff, K. Haas-Santo, R. Dittmeyer, Experimental and modeling study of gas transport through composite ceramic membranes, Chem. Eng. Sci. 108 (2014) 94–102. doi:10.1016/j.ces.2013.12.030.

[92] A.M. Avila, H.H. Funke, Y. Zhang, J.L. Falconer, R.D. Noble, Concentration polarization in SAPO-34 membranes at high pressures, J. Memb. Sci. 335 (2009) 32–36. doi:10.1016/j.memsci.2009.02.028.

[93] M. Grahn, J. Hedlund, Maxwell-Stefan modeling of high flux tubular silicalite-1 membranes for CO2removal from CO2/H2gas mixtures, J. Memb. Sci. 471 (2014) 328–337. doi:10.1016/j.memsci.2014.08.034.

[94] S. Farooq, I.A. Karimi, Modeling support resistance in zeolite membranes, J. Memb. Sci. 186 (2001) 109–121. doi:10.1016/S0376-7388(00)00671-2.

[95] J.G. Martinek, T.Q. Gardner, R.D. Noble, J.L. Falconer, Modeling transient permeation of

binary mixtures through zeolite membranes, Ind. Eng. Chem. Res. 45 (2006) 6032–6043. doi:10.1021/ie060166u.

[96] E.N. Fuller, P.D. Schettler, J.C. Giddings, A new method for prediction of binary gas-phase diffusion coefficients, Ind. Eng. Chem. 58 (1966) 18–27. doi:10.1021/ie50677a007.

[97] F. Kapteijn, W.J.W. Bakker, J. van de Graaf, G. Zheng, J. Poppe, J.A. Moulijn, Permeation and separation behaviour of a silicalite-1 membrane, Catal. Today. 25 (1995) 213–218. doi:10.1016/0920-5861(95)00078-T.

[98] S. Bhattacharya, S.-T. Hwang, Concentration polarization, separation factor, and Peclet number in membrane process, J. Memb. Sci. (1997) 73–90.

[99] G. He, Y. Mi, P.L. Yue, G. Chen, Theoretical study on concentration polarization in gas separation membrane processes., J. Membr. Sci. 153 (1999) 243–258.

[100] B. Raghunath, S.T. Hwang, Effect of boundary layer mass transfer resistance in the pervaporation of dilute organics, J. Memb. Sci. 65 (1992) 147–161. doi:10.1016/0376-7388(92)87061-2.

[101] G. Ji, G. Wang, K. Hooman, S. Bhatia, J.C. Diniz da Costa, Simulation of binary gas separation through multi-tube molecular sieving membranes at high temperatures, Chem. Eng. J. 218 (2013) 394–404. doi:10.1016/j.cej.2012.12.063.

[102] G. Ji, G. Wang, K. Hooman, S. Bhatia, J.C. Diniz da Costa, The fluid dynamic effect on the driving force for a cobalt oxide silica membrane module at high temperatures, Chem. Eng. Sci. 111 (2014) 142–152. doi:10.1016/j.ces.2014.02.006.

[103] X. Feng, R.Y.M. Huang, Concentration polarization in pervaporation separation processes, J. Memb. Sci. 92 (1994) 201–208. doi:10.1016/0376-7388(94)00056-5.

[104] W.M. (William M. Deen, Analysis of transport phenomena, n.d.

[105] S. (Sadık) Kakaç, R.K. Shah, W. Aung, Handbook of single-phase convective heat transfer, Wiley, 1987.

[106] E. Kim, J. Choi, M. Tsapatsis, On defects in highly a-oriented MFI membranes, Microporous Mesoporous Mater. 170 (2013) 1–8. doi:10.1016/j.micromeso.2012.11.023.

[107] J. Hedlund, D. Korelskiy, L. Sandström, J. Lindmark, Permporometry analysis of zeolite membranes, J. Memb. Sci. 345 (2009) 276–287. doi:10.1016/j.memsci.2009.09.012.

[108] E.E. Mallon, M.Y. Jeon, M. Navarro, A. Bhan, M. Tsapatsis, Probing the relationship between silicalite-1 defects and polyol adsorption properties, Langmuir. 29 (2013) 6546–6555. doi:10.1021/la4001494.

[109] M.E. Dose, K. Zhang, J.A. Thompson, J. Leisen, R.R. Chance, W.J. Koros, B.A. McCool, R.P. Lively, Effect of crystal size on framework defects and water uptake in fluoride mediated silicalite-1, Chem. Mater. 26 (2014) 4368–4376. doi:10.1021/cm500914b.

[110] P.H. Nelson, M. Tsapatsis, S.M. Auerbach, Modeling permeation through anisotropic zeolite membranes with nanoscopic defects, J. Memb. Sci. 184 (2001) 245–255. doi:10.1016/S0376-7388(00)00641-4.

[111] J. Kangas, L. Sandström, I. Malinen, J. Hedlund, J. Tanskanen, Maxwell-Stefan modeling of the separation of H2and CO2at high pressure in an MFI membrane, J. Memb. Sci. 435 (2013) 186–206. doi:10.1016/j.memsci.2013.02.026.

[112] W. Ding, H. Li, P. Pfeifer, R. Dittmeyer, Crystallite-pore network model of transport and reaction of multicomponent gas mixtures in polycrystalline microporous media, Chem. Eng.

J. 254 (2014) 545–558. doi:10.1016/j.cej.2014.05.081.

[113] G. Soave, Equilibrium constants from a modified Redlich-Kwong equation of state, Chem. Eng. Sci. 27 (1972) 1197–1203. doi:10.1016/0009-2509(72)80096-4.

[114] J.F. Ely, H.J.M. Hanley, Prediction of transport properties. 1. Viscosity of fluids and mixtures, Ind. Eng. Chem. Fundam. 20 (1981) 323–332. doi:10.1021/i100004a004.

[115] Process Systems Enterprise, gPROMS, www.psenterprise.com/gproms, 1997-2018, (n.d.).

[116] S. Moganti, R.D. Noble, C.A. Kovalb, Analysis of a membrane / distillation column hybrid process, J. Memb. Sci. 93 (1994).

[117] W. Stephan, R.D. Noble, C.A. Koval, Design methodology for a membrane / distillation column hybrid process, J. Memb. Sci. 99 (1995) 259–272.

[118] T. Pettersen, K.M. Lien, Design of hybrid distillation and vapor permeation processes, J. Memb. Sci. 102 (1995) 21–30. doi:10.1016/0376-7388(94)00216-L.

[119] T.G. Pressly, K.M. Ng, A Break-Even Analysis of Distillation-Membrane Hybrids, AIChE J. 44 (1998) 93–105.

[120] T. Titze, C. Chmelik, J. Kärger, J.M. van Baten, R. Krishna, Uncommon Synergy between Adsorption and Diffusion of Hexane Isomer Mixtures in MFI Zeolite Induced by Configurational Entropy Effects, J. Phys. Chem. C. 118 (2014) 2660–2665. doi:10.1021/jp412526t.

[121] H. Stach, U. Lohse, H. Thamm, W. Schirmer, Adsorption equilibria of hydrocarbons on highly dealuminated zeolites, Zeolites. 6 (1986) 74–90. doi:10.1016/S0144-2449(86)80001-X.

[122] R.E. Richards, L.V.C. Rees, Sorption and Packing of n-Alkane Molecules in ZSM-5, Langmuir. 3 (1987) 335–340. doi:10.1021/la00075a009.

[123] M.S. Sun, D.B. Shah, H.H. Xu, O. Talu, Adsorption Equilibria of C1 to C4 Alkanes, CO2 , and SF6 on Silicalite, J. Phys. Chem. B. 102 (1998) 1466–1473. doi:10.1021/jp9730196.

[124] W. Zhu, J.M. Van De Graaf, L.J.P. Van Den Broeke, F. Kapteijn, J.A. Moulijn, TEOM: a unique technique for measuring adsorption properties. Light alkanes in silicalite-1, Ind. Eng. Chem. Res. 37 (1998) 1934–1942. doi:10.1021/ie970739q.

[125] W. Zhu, F. Kapteijn, J.A. Moulijn, Adsorption of light alkanes on silicalite-1 : Reconciliation of experimental data and molecular simulations, Phys. Chem. Chem. Phys. (2000) 1989–1995.

[126] H.B. Abdul-Rehman, M.A. Hasanain, K.F. Loughlin, Quaternary , Ternary , Binary , and Pure Component Sorption on Zeolites . Pressures, Ind. Eng. Chem. Res. 29 (1990) 1525–1535.

[127] R.L. June, A.T. Bell, D.N. Theodorou, Prediction of Low Occupamy Sorption of Alkanes in, J. Phys. Chem. (1990) 1508–1516.

[128] B. Smit, J.I. Siepmann, Computer simulations of the energetics and siting of n-alkanes in zeolites, J. Phys. Chem. 98 (1994) 8442–8452. doi:10.1021/j100085a027.

[129] E.J. Maginn, A.T. Bell, D.N. Theodorou, Sorption thermodynamics, siting, and conformation of long n-alkanes in silicalite as predicted by configurational-bias Monte Carlo integration, J. Phys. Chem. 99 (1995) 2057–2079. doi:10.1021/j100007a042.

[130] H. Thamm, Adsorption site heterogeneity in silicalite: a calorimetric study, Zeolites. 7 (1987) 341–346. doi:10.1016/0144-2449(87)90037-6.

[131] H. Thamm, Calorimetric study on the state of C1-C4 alcohols sorbed on silicalite, J. Chem. Soc. Faraday Trans. 1. 85 (1989) 1. doi:10.1039/f19898500001.

[132] T.J.H. Vlugt, W. Zhu, F. Kapteijn, J.A. Moulijn, R. Krishna, B. Smit, Adsorption Isotherms of Linear and Branched Alkanes in the Zeolite Silicalite-I, J. Am. Chem. Soc. 120 (1998) 5599–5600. doi:10.1021/ja974336t.

[133] R. Krishna, D. Paschek, Separation of hydrocarbon mixtures using zeolite membranes: A modelling approach combining molecular simulations with the Maxwell-Stefan theory, Sep. Purif. Technol. 21 (2000) 111–136. doi:10.1016/S1383-5866(00)00196-9.

[134] C. Chmelik, L. Heinke, J.M. van Baten, R. Krishna, Diffusion of n-butane/iso-butane mixtures in silicalite-1 investigated using infrared (IR) microscopy, Microporous Mesoporous Mater. 125 (2009) 11–16. doi:10.1016/j.micromeso.2009.02.015.

[135] K.P. Datema, C.J.J. Denouden, W.D. Ylstra, H.P.C.E. Kuipers, M.F.M. Post, J. Kärger, Fourier-Transform Pulsed-Field-Gradient H-1 Nuclear-Magnetic- Resonance Investigation of the Diffusion of Light Normal-Alkanes in Zeolite ZSM-5, J. Chem. Soc. Faraday Trans. 87 (1991) 1935–1943.

[136] W. Heink, J. Karger, H. Pfeifer, K.P. Datema, A.K. Nowak, High-temperature Pulsed Field Gradient Nuclear Magnetic Resonance Self-diff, J. Chem. Soc., Faraday. Trans. 88 (1992) 3505–3509.

[137] A. Pampel, M. Fernandez, D. Freude, J. Kärger, New options for measuring molecular diffusion in zeolites by MAS PFG NMR, Chem. Phys. Lett. 407 (2005) 53–57. doi:10.1016/j.cplett.2005.03.062.

[138] S. Brandani, J. Caro, H. Jobic, J. Kärger, C. Krause, R. Staudt, Diffusion of n-alkanes in zeolites: the benefit of observation over different length scales, Elsevier B.V., 2007. doi:10.1016/S0167-2991(07)80949-9.

[139] M. Fernandez, J. Kärger, D. Freude, A. Pampel, J.M. van Baten, R. Krishna, Mixture diffusion in zeolites studied by MAS PFG NMR and molecular simulation, Microporous Mesoporous Mater. 105 (2007) 124–131. doi:10.1016/j.micromeso.2007.05.042.

[140] K. Banas, F. Brandani, D.M. Ruthven, F. Stallmach, J. Kärger, Combining macroscopic and microscopic diffusion studies in zeolites using NMR techniques, Magn. Reson. Imaging. 23 (2005) 227–232. doi:10.1016/j.mri.2004.11.015.

[141] H. Jobic, Diffusion of linear and branched alkanes in ZSM-5. A quasi-elastic neutron scattering study, J. Mol. Catal. A Chem. 158 (2000) 135–142. doi:10.1016/S1381-1169(00)00057-1.

[142] B. Millot, A. Méthivier, H. Jobic, H. Moueddeb, M. Bée, Diffusion of Isobutane in ZSM-5 Zeolite: A Comparison of Quasi-Elastic Neutron Scattering and Supported Membrane Results, J. Phys. Chem. B. 103 (1999) 1096–1101. doi:10.1021/jp982897g.

[143] A.S. Chiang, A.G. Dixon, Y.H. Ma, The determination of zeolite crystal diffusivity by gas chromatography-II. Experimental, Chem. Eng. Sci. 39 (1984) 1461–1468. doi:10.1016/0009-2509(84)80004-4.

[144] J.R. Hufton, R.P. Danner, Chromatographic study of alkanes in silicalite: Equilibrium properties, AIChE J. 39 (1993) 954–961. doi:10.1002/aic.690390605.

[145] T. a Nijhuis, L.J.P. Van Den Broeke, M.J.G. Linders, J.M. Van De Graaf, F. Kapteijn, M. Makkee, J. a Moulijn, Measurement and modeling of the transient adsorption , desorption and diffusion processes in microporous materials, Chem. Eng. Sci. 54 (1999) 4423–4436.

[146] T.A. Nijhuis, L.J.P. van den Broeke, M.J.G. Linders, M. Makkee, F. Kapteijn, J.A. Moulijn, Modeling of the transient sorption and diffusion processes in microporous materials at low pressure, Catal. Today. 53 (1999) 189–205. doi:http://dx.doi.org/10.1016/S0920-5861(99)00116-9.

[147] J.R. Hufton, D.M. Ruthven, Diffusion of Light Alkanes in Silicalite Studied by the Zero Length Column Method, Ind. Eng. Chem. Res. 32 (1993) 2379–2386. doi:10.1021/ie00022a022.

[148] M. Jiang, M. Eic, S. Miachon, J.A. Dalmon, M. Kocirik, Diffusion of n-butane, isobutane and ethane in a MFI-zeolite membrane investigated by gas permeation and ZLC measurements, Sep. Purif. Technol. 25 (2001) 287–295. doi:10.1016/S1383-5866(01)00055-7.

[149] M. Jiang, M. Eić, Transport properties of ethane, butanes and their binary mixtures in MFI-type zeolite and zeolite-membrane samples, Adsorption. 9 (2003) 225–234. doi:10.1023/A:1024797716739.

[150] W. Zhu, A. Malekian, M. Eić, F. Kapteijn, J.A. Moulijn, Concentration-dependent diffusion of isobutane in silicalite-1 studied with ZLC technique, Chem. Eng. Sci. 59 (2004) 3827–3835. doi:10.1016/j.ces.2004.06.007.

[151] A.P. Guimarães, A. Möller, R. Staudt, D.C.S. De Azevedo, S.M.P. Lucena, C.L. Cavalcante, Diffusion of linear paraffins in silicalite studied by the ZLC method in the presence of CO2, Adsorption. 16 (2010) 29–36. doi:10.1007/s10450-010-9205-6.

[152] D.T. Hayhurst, A.R. Paravar, Diffusion of C1 to C5 normal paraffins in silicalite, Zeolites. 8 (1988) 27–29. doi:10.1016/S0144-2449(88)80025-3.

[153] D.B. Shah, S. Chokchai-Acha, D.T. Hayhurst, Measurements of transport rates of C4 hydrocarbons across a single-crystal silicalite membrane, J. Chem. Soc. Faraday Trans. 89 (1993) 3161. doi:10.1039/ft9938903161.

[154] O. Talu, M.S. Sun, D.B. Shah, Diffusivities of n-alkanes in silicalite by steady-state single-crystal membrane technique, AIChE J. 44 (1998) 681–694. doi:10.1002/aic.690440316.

[155] M.S. Sun, O. Talu, D.B. Shah, Diffusion Measurements through Embedded Zeolite Crystals, AIChE J. 42 (1996) 3001–3007. doi:10.1002/aic.690421102.

[156] O. Geier, S. Vasenkov, E. Lehmann, J. Kärger, U. Schemmert, R.A. Rakoczy, J. Weitkamp, Interference microscopy investigation of the influence of regular intergrowth effects in MFI-type zeolites on molecular uptake, J. Phys. Chem. B. 105 (2001) 10217–10222. doi:10.1021/jp010777u.

[157] P. Kortunov, S. Vasenkov, C. Chmelik, J. Kärger, D.M. Ruthven, J. Wloch, Influence of defects on the external crystal surface on molecular uptake into MFI-type zeolites, Chem. Mater. 16 (2004) 3552–3558. doi:10.1021/cm0401645.

[158] C. Chmelik, P. Kortunov, S. Vasenkov, J. Kärger, Internal transport resistances and their influence on diffusion in zeolites as traced by microscopic measuring techniques, Adsorption. 11 (2005) 455–460. doi:10.1007/s10450-005-5967-7.

[159] C. Chmelik, A. Varma, L. Heinke, D.B. Shah, J. Kärger, F. Kremer, U. Wilczok, W. Schmidt, Effect of surface modification on uptake rates of isobutane in MFI crystals: An infrared microscopy study, Chem. Mater. 19 (2007) 6012–6019. doi:10.1021/cm071632o.

[160] L.V.C. Rees, P.C. Laboratories, Adsorption and diffusion 2-butyne in silicalite-I, Zeolites. 11 (1991) 684–689.

[161] A. Möller, A. Pessoa Guimaraes, R. Gläser, R. Staudt, Uptake-curves for the determination of diffusion coefficients and sorption equilibria for n-alkanes on zeolites, Microporous Mesoporous Mater. 125 (2009) 23–29. doi:10.1016/j.micromeso.2009.04.029.

[162] R.L. June, A.T. Bell, D.N. Theodorou, Molecular Dynamics Studies of Butane and Hexane in Siiicalite, J. Phys. Chem. 96 (1992) 1051–1060. doi:10.1021/j100182a009.

[163] H. Jobic, D.N. Theodorou, Diffusion of long n-alkanes in silicalite. A comparison between neutron scattering experiments and hierarchical simulation results, J. Phys. Chem. B. 110 (2006) 1964–1967. doi:10.1021/jp056924w.

[164] R.C. Runnebaum, E.J. Maginn, Molecular Dynamics Simulations of Alkanes in the Zeolite Silicalite: Evidence for Resonant Diffusion Effects, J. Phys. Chem. 101 (1997) 6394–6408. doi:10.1021/jp970774a.

[165] A. Bouyermaouen, A. Bellemans, Molecular dynamics simulation of the diffusion of n-butane and i-butane in silicalite, J. Chem. Phys. 108 (1998) 2170–2172. doi:10.1063/1.475596.

[166] L.N. Gergidis, D.N. Theodorou, Molecular Dynamics Simulation of n-Butane-Methane Mixtures in Silicalite, J. Phys. Chem. B. 103 (1999) 3380–3390. doi:10.1021/jp983680p.

[167] D. Paschek, R. Krishna, Monte Carlo simulations of sorption and di€ usion of isobutane in silicalite, 342 (2001) 148–154.

[168] D. Shen, L.V.C. Rees, J. Caro, M. Bulow, B. Zibrowius, Diffusion of C4 Hydrocarbons in Silicalite-1, J Chem. Soc. Faraday Trans. 86 (1990) 3943–3948.

[169] S. Goodbody, K. Watanabe, D. MacGowan, J.P. Walton, N. Quirke, Molecular Simulation of Methane and Butane in Silicalite, J Chem. Soc. Faraday Trans. 87 (2007) 1951–1958. doi:10.1080/08927029008022415.

[170] A.J. O'Malley, C.R.A. Catlow, M. Monkenbusch, H. Jobic, Diffusion of Isobutane in Silicalite: A Neutron Spin-Echo and Molecular Dynamics Simulation Study, J. Phys. Chem. C. 119 (2015) 26999–27006. doi:10.1021/acs.jpcc.5b08048.

[171] H. Jobic, A. Méthivier, G. Ehlers, B. Farago, W. Haeussler, Accelerated Diffusion of Long-Chain Alkanes between Nanosized Cavities, Angew. Chemie - Int. Ed. 43 (2004) 364–366. doi:10.1002/anie.200352691.

[172] H. Jobic, H. Ramanan, S.M. Auerbach, M. Tsapatsis, P. Fouquet, Probing cooperative jump-diffusion in zeolites: Neutron spin-echo measurements and molecular dynamics simulations of benzene in NaX, Microporous Mesoporous Mater. 90 (2006) 307–313. doi:10.1016/j.micromeso.2005.11.006.

[173] V. Sebastian, R. Mallada, J. Coronas, A. Julbe, R.A. Terpstra, R.W.J. Dirrix, Microwave-assisted hydrothermal rapid synthesis of capillary MFI-type zeolite – ceramic membranes for pervaporation application, J. Memb. Sci. 355 (2010) 28–35. doi:10.1016/j.memsci.2010.02.073.

[174] F. Kapteijn, W.J.W. Bakker, G. Zheng, J.A. Moulijn, Temperature- and occupancy-dependent diffusion of n-butane through a silicalite-1 membrane, Microporous Mater. 3 (1994) 227–234. doi:10.1016/0927-6513(94)00035-2.

[175] W.J.W. Bakker, L.J.P. Van Den Broeke, F. Kapteijn, J.A. Moulijn, Temperature Dependence of One-Component Permeation through a Silicalite-I Membrane, AIChE J. 43 (1997) 2203–2214.

[176] J.M. Van De Graaf, F. Kapteijn, J.A. Moulijn, Diffusivities of light alkanes in a silicalite-1

membrane layer, Microporous Mesoporous Mater. 35–36 (2000) 267–281. doi:10.1016/S1387-1811(99)00227-9.

[177] F. Kapteijn, J. Poppe, J.A. Moulijn, Permeation characteristics of a metal-supported silicalite-1 zeolite membrane, J. Memb. Sci. 117 (1996) 57–78.

[178] Z.A.E.P. Vroon, K. Keizer, M.J. Gilde, H. Verweij, A.J. Burggraaf, Transport properties of alkanes through ceramic thin zeolite MFI membranes, J. Memb. Sci. 113 (1996) 293–300. doi:10.1016/0376-7388(95)00128-X.

[179] A.J. Burggraaf, Z.A.E.P. Vroon, K. Keizer, H. Verweij, Permeation of single gases in thin zeolite MFI membranes, J. Memb. Sci. 144 (1998) 77–86. doi:10.1016/S0376-7388(98)00036-2.

[180] A.J. Burggraaf, Single gas permeation of thin zeolite (MFI) membranes: Theory and analysis of experimental observations, J. Memb. Sci. 155 (1999) 45–65. doi:10.1016/S0376-7388(98)00295-6.

[181] T.Q. Gardner, J.B. Lee, R.D. Noble, J.L. Falconer, Adsorption and Diffusion Properties of Butanes in ZSM-5 Zeolite Membranes, Ind. Eng. Chem. Res. 41 (2002) 4094–4105. doi:10.1021/ie020144h.

[182] T.Q. Gardner, J.L. Falconer, R.D. Noble, Adsorption and diffusion properties of zeolite membranes by transient permeation, Desalination. 149 (2002) 435–440. doi:10.1016/S0011-9164(02)00772-5.

[183] V.A. Tuan, J.L. Falconer, R.D. Noble, Alkali-free ZSM-5 membranes: Preparation conditions and separation performance, Ind. Eng. Chem. Res. 38 (1999) 3635–3646. doi:10.1021/ie980808g.

[184] H.K. Jeong, Z. Lai, M. Tsapatsis, J.C. Hanson, Strain of MFI crystals in membranes: An in situ synchrotron X-ray study, Microporous Mesoporous Mater. 84 (2005) 332–337. doi:10.1016/j.micromeso.2005.05.043.

[185] N. Rangnekar, M. Shete, K.V. Agrawal, B. Topuz, P. Kumar, Q. Guo, I. Ismail, A. Alyoubi, S. Basahel, K. Narasimharao, C.W. Macosko, K.A. Mkhoyan, S. Al-Thabaiti, B. Stottrup, M. Tsapatsis, 2D zeolite coatings: Langmuir-Schaefer deposition of 3 nm thick MFI zeolite nanosheets, Angew. Chemie - Int. Ed. 54 (2015) 6571–6575. doi:10.1002/anie.201411791.

[186] J.N. Ghogomu, C. Guigui, J.C. Rouch, M.J. Clifton, P. Aptel, Hollow-fibre membrane module design: Comparison of different curved geometries with Dean vortices, J. Memb. Sci. 181 (2001) 71–80. doi:10.1016/S0376-7388(00)00364-1.

[187] H.B. Winzeler, G. Belfort, Enhanced performance for pressure-driven membrane processes: the argument for fluid instabilities, J. Memb. Sci. 80 (1993) 35–47. doi:10.1016/0376-7388(93)85130-O.

[188] K.T. Klemola, J.K. Ilme, Distillation efficiencies of an industrial-scale i-butane/n-butane fractionator, Ind. Eng. Chem. Res. 35 (1996) 4579–4586. doi:10.1021/ie960390r.

[189] J.M. (James M. Douglas, Conceptual design of chemical processes, McGraw-Hill, 1988.

[190] R. Turton, Analysis, synthesis, and design of chemical processes, Prentice Hall, 2012.

[191] M. Morales, J. Quintero, R. Conejeros, G. Aroca, Life cycle assessment of lignocellulosic bioethanol: Environmental impacts and energy balance, Renew. Sustain. Energy Rev. 42 (2015) 1349–1361. doi:10.1016/j.rser.2014.10.097.

[192] S.K. Thangavelu, A.S. Ahmed, F.N. Ani, Review on bioethanol as alternative fuel for spark

ignition engines, Renew. Sustain. Energy Rev. 56 (2016) 820–835. doi:10.1016/j.rser.2015.11.089.

[193] B. Daylan, N. Ciliz, Life cycle assessment and environmental life cycle costing analysis of lignocellulosic bioethanol as an alternative transportation fuel, Renew. Energy. 89 (2016) 578–587. doi:10.1016/J.RENENE.2015.11.059.

[194] M. Galbe, G. Zacchi, A review of the production of ethanol from softwood, Appl. Microbiol. Biotechnol. 59 (2002) 618–628. doi:10.1007/s00253-002-1058-9.

[195] H. Chen, X. Fu, Industrial technologies for bioethanol production from lignocellulosic biomass, Renew. Sustain. Energy Rev. 57 (2016) 468–478. doi:10.1016/j.rser.2015.12.069.

[196] A.J. Ragauskas, C.K. Williams, B.H. Davison, G. Britovsek, J. Cairney, C.A. Eckert, W.J. Frederick Jr., J.P. Hallett, D.J. Leak, C.L. Liotta, J.R. Mielenz, R. Murphy, R. Templer, T. Tschaplinski, The Path Forward for Biofuels and Biomaterials\r10.1126/science.1114736, Science (80-.). 311 (2006) 484–489. doi:10.1126/science.1114736.

[197] J.B. Haelssig, A.Y. Tremblay, J. Thibault, X.M. Huang, Membrane Dephlegmation: A hybrid membrane separation process for efficient ethanol recovery, J. Memb. Sci. 381 (2011) 226–236. doi:10.1016/j.memsci.2011.07.035.

[198] C.A. Cardona Alzate, O.J. Sánchez Toro, Energy consumption analysis of integrated flowsheets for production of fuel ethanol from lignocellulosic biomass, Energy. 31 (2006) 2111–2123. doi:10.1016/j.energy.2005.10.020.

[199] H.J. Huang, S. Ramaswamy, U.W. Tschirner, B. V. Ramarao, A review of separation technologies in current and future biorefineries, Sep. Purif. Technol. 62 (2008) 1–21. doi:10.1016/j.seppur.2007.12.011.

[200] N. Mittal, P. Bai, J.I. Siepmann, P. Daoutidis, M. Tsapatsis, Bioethanol enrichment using zeolite membranes: Molecular modeling, conceptual process design and techno-economic analysis, J. Memb. Sci. 540 (2017) 464–476. doi:10.1016/j.memsci.2017.06.075.

[201] L.M. Vane, Separation technologies for the recovery and dehydration of alcohols from fermentation broths, Biofuels, Bioprod. Biorefining. 2 (2008) 553–588. doi:10.1002/bbb.108.

[202] P. Taylor, P. Peng, B. Shi, Y. Lan, P. Peng, B. Shi, Y. Lan, Separation Science and Technology A Review of Membrane Materials for Ethanol Recovery by Pervaporation A Review of Membrane Materials for Ethanol Recovery by Pervaporation, Sep. Sci. Technol. (2013) 37–41. doi:10.1080/01496395.2010.504681.

[203] L.M. Vane, A review of pervaporation for product recovery from biomass fermentation processes †, J. Chem. Technol. Biotechnol. 629 (2005) 603–629. doi:10.1002/jctb.1265.

[204] V. Van Hoof, C. Dotremont, A. Buekenhoudt, Performance of Mitsui NaA type zeolite membranes for the dehydration of organic solvents in comparison with commercial polymeric pervaporation membranes, Sep. Purif. Technol. 48 (2006) 304–309. doi:10.1016/J.SEPPUR.2005.06.019.

[205] Y. Morigami, M. Kondo, J. Abe, H. Kita, K. Okamoto, The first large-scale pervaporation plant using tubular-type module with zeolite NaA membrane, Sep. Purif. Technol. 25 (2001) 251–260. doi:10.1016/S1383-5866(01)00109-5.

[206] J. Caro, M. Noack, P. Kölsch, Zeolite membranes: From the laboratory scale to technical applications, Adsorption. 11 (2005) 215–227. doi:10.1007/s10450-005-5394-9.

[207] M. Weyd, H. Richter, P. Puhlf, I. Voigt, C. Hamel, A. Seidel-morgenstern, Transport of

binary water – ethanol mixtures through a multilayer hydrophobic zeolite membrane, J. Memb. Sci. 307 (2008) 239–248. doi:10.1016/j.memsci.2007.09.032.

[208] P. Bai, M.Y. Jeon, L. Ren, C. Knight, M.W. Deem, M. Tsapatsis, J.I. Siepmann, Discovery of optimal zeolites for challenging separations and chemical transformations using predictive materials modeling, Nat. Commun. 6 (2015) 1–9. doi:10.1038/ncomms6912.

[209] M. Trzpit, M. Soulard, J. Patarin, N. Desbiens, F. Cailliez, A. Boutin, I. Demachy, A.H. Fuchs, The effect of local defects on water adsorption in silicalite-1 zeolite: A joint experimental and molecular simulation study, Langmuir. 23 (2007) 10131–10139. doi:10.1021/la7011205.

[210] K. Sato, T. Nakane, A high reproducible fabrication method for industrial production of high flux NaA zeolite membrane, J. Memb. Sci. 301 (2007) 151–161. doi:10.1016/j.memsci.2007.06.010.

[211] M. Pera-Titus, C. Fité, V. Sebastián, E. Lorente, J. Llorens, F. Cunill, Modeling pervaporation of ethanol/water mixtures within "real" zeolite NaA membranes, Ind. Eng. Chem. Res. 47 (2008) 3213–3224. doi:10.1021/ie071645b.

[212] K. Sato, K. Aoki, K. Sugimoto, K. Izumi, S. Inoue, J. Saito, S. Ikeda, T. Nakane, Dehydrating performance of commercial LTA zeolite membranes and application to fuel grade bio-ethanol production by hybrid distillation/vapor permeation process, Microporous Mesoporous Mater. 115 (2008) 184–188. doi:10.1016/J.MICROMESO.2007.10.053.

[213] Bin Chen, and Jeffrey J. Potoff, J.I. Siepmann, Monte Carlo Calculations for Alcohols and Their Mixtures with Alkanes. Transferable Potentials for Phase Equilibria. 5. United-Atom Description of Primary, Secondary, and Tertiary Alcohols, (2001). doi:10.1021/JP003882X.

[214] W.L. Jorgensen, J. Chandrasekhar, J.D. Madura, R.W. Impey, M.L. Klein, Comparison of simple potential functions for simulating liquid water, J. Chem. Phys. 79 (1983) 926–935. doi:10.1063/1.445869.

[215] P. Bai, M. Tsapatsis, J.I. Siepmann, TraPPE-zeo: Transferable potentials for phase equilibria force field for all-silica zeolites, J. Phys. Chem. C. 117 (2013) 24375–24387. doi:10.1021/jp4074224.

[216] J.I. Siepmann, D. Frenkel, Configurational bias Monte Carlo: a new sampling scheme for flexible chains, Mol. Phys. 75 (1992) 59–70. doi:10.1080/00268979200100061.

[217] M.G.M. and, J.I. Siepmann, Novel Configurational-Bias Monte Carlo Method for Branched Molecules. Transferable Potentials for Phase Equilibria. 2. United-Atom Description of Branched Alkanes, (1999). doi:10.1021/JP984742E.

[218] P. Bai, J.I. Siepmann, Assessment and Optimization of Configurational-Bias Monte Carlo Particle Swap Strategies for Simulations of Water in the Gibbs Ensemble, J. Chem. Theory Comput. 13 (2017) 431–440. doi:10.1021/acs.jctc.6b00973.

[219] A.Z. Panagiotopoulos, N. Quirke, M. Stapleton, D.J. Tildesley, Phase equilibria by simulation in the Gibbs ensemble, Mol. Phys. 63 (1988) 527–545. doi:10.1080/00268978800100361.

[220] Hoover, Canonical dynamics: Equilibrium phase-space distributions., Phys. Rev. A, Gen. Phys. 31 (1985) 1695–1697. http://www.ncbi.nlm.nih.gov/pubmed/9895674 (accessed February 25, 2018).

[221] W.C. Swope, H.C. Andersen, P.H. Berens, K.R. Wilson, A computer simulation method for

the calculation of equilibrium constants for the formation of physical clusters of molecules: Application to small water clusters, J. Chem. Phys. 76 (1982) 637–649. doi:10.1063/1.442716.

[222] M.P. Allen, D.J. Tildesley, Computer simulation of liquids, Clarendon Press, 1989.

[223] F. Cailliez, M. Trzpit, M. Soulard, I. Demachy, A. Boutin, J. Patarin, A.H. Fuchs, Thermodynamics of water intrusion in nanoporous hydrophobic solids, Phys. Chem. Chem. Phys. 10 (2008) 4817. doi:10.1039/b807471b.

[224] Y. Oumi, A. Miyajima, J. Miyamoto, T. Sano, Binary mixture adsorption of water and ethanol on silicalite, Stud. Surf. Sci. Catal. 142 (2002) 1595–1602. doi:10.1016/S0167-2991(02)80329-9.

[225] D.H. Olson, W.O. Haag, W.S. Borghard, Use of water as a probe of zeolitic properties: Interaction of water with HZSM-5, Microporous Mesoporous Mater. 35–36 (2000) 435–446. doi:10.1016/S1387-1811(99)00240-1.

[226] J. Caro, S. Hŏcevar, J. Kärger, L. Riekert, Intracrystalline self-diffusion of H2O and CH4 in ZSM-5 zeolites, Zeolites. 6 (1986) 213–216. doi:10.1016/0144-2449(86)90051-5.

[227] V.R. Choudhary, V.S. Nayak, T. V Choudhary, Single-Component Sorption / Diffusion of Cyclic Compounds from Their Bulk Liquid Phase in H-ZSM-5 Zeolite, Society. (1997) 1812–1818.

[228] J.Z. Yang, Q.L. Liu, H.T. Wang, Analyzing adsorption and diffusion behaviors of ethanol / water through silicalite membranes by molecular simulation, J. Memb. Sci. 291 (2007) 1–9. doi:10.1016/j.memsci.2006.12.025.

[229] A. Özgür Yazaydin, R.W. Thompson, Molecular simulation of water adsorption in silicalite: Effect of silanol groups and different cations, Microporous Mesoporous Mater. 123 (2009) 169–176. doi:10.1016/j.micromeso.2009.03.045.

[230] X. Zou, P. Bazin, F. Zhang, G. Zhu, V. Valtchev, Ethanol Recovery from Water Using Silicalite-1 Membrane : An Operando Infrared Spectroscopic Study, Chem Plus Chem. 130012 (2012) 437–444. doi:10.1002/cplu.201200048.

[231] V.S. Nayak, J.B. Moffat, Sorption and diffusion of alcohols in heteropoly oxometalates and ZSM-5 zeolite, J. Phys. Chem. 92 (1988) 7097–7102. doi:10.1021/j100336a014.

[232] Y.S. Lin, Y. Hua Ma, Liquid Diffusion and Adsorption of Aqueous Ethanol, Propanols, and Butanols in Silicalite by HPLC, in: 1988: pp. 452–466. doi:10.1021/bk-1988-0368.ch028.

[233] F.A. Farhadpour, A. Bono, Sorptive separation of ethanol-water mixtures with a bi-dispersed hydrophobic molecular sieve, silicalite: determination of the controlling mass transfer mechanism, Chem. Eng. Process. Process Intensif. 35 (1996) 141–155. doi:10.1016/0255-2701(95)04138-9.

[234] C. Bussai, S. Vasenkov, H. Liu, W. Böhlmann, S. Fritzsche, S. Hannongbua, R. Haberlandt, J. Kärger, On the diffusion of water in silicalite-1: MD simulations using ab initio fitted potential and PFG NMR measurements, Appl. Catal. A Gen. 232 (2002) 59–66. doi:10.1016/S0926-860X(02)00066-2.

[235] M.U. Arı, M.G. Ahunbay, M. Yurtsever, A. Erdem-Şenatalar, Molecular Dynamics Simulation of Water Diffusion in MFI-Type Zeolites, J. Phys. Chem. B. 113 (2009) 8073–8079. doi:10.1021/jp901986s.

[236] M.G. Ahunbay, Monte Carlo Simulation of Water Adsorption in Hydrophobic MFI Zeolites with Hydrophilic Sites (vol 27, pg 4986, 2011), Langmuir. 27 (2011) 14703. doi:

10.1021/La2039174.

[237] R. Krishna, Diffusion of binary mixtures in zeolites: molecular dynamics simulations versus Maxwell–Stefan theory, Chem. Phys. Lett. 326 (2000) 477–484. doi:10.1016/S0009-2614(00)00846-0.

[238] R.W. Baker, J.G. Wijmans, Y. Huang, Permeability, permeance and selectivity: A preferred way of reporting pervaporation performance data, J. Memb. Sci. 348 (2010) 346–352. doi:10.1016/j.memsci.2009.11.022.

[239] N. Mittal, P. Bai, A. Kelloway, J.I. Siepmann, P. Daoutidis, M. Tsapatsis, A mathematical model for zeolite membrane module performance and its use for techno-economic evaluation of improved energy efficiency hybrid membrane-distillation processes for butane isomer separations, J. Memb. Sci. 520 (2016) 434–449. doi:10.1016/j.memsci.2016.06.041.

[240] M. Nomura, T. Yamaguchi, S. Nakao, Ethanol / water transport through silicalite membranes, J. Memb. Sci. 144 (1998) 161–171.

[241] T. Sano, H. Yanagishitab, K. Harayab, F. Mizukamib, K. Haraya, Separation of ethanol/water mixture by silicalite membrane on pervaporation, J. Memb. Sci. 95 (1994) 221–228.

[242] X. Zhang, M. Zhu, R. Zhou, X. Chen, H. Kita, Synthesis of a Silicalite Zeolite Membrane in Ultradilute Solution and Its Highly Selective Separation of Organic / Water Mixtures, Ind. Eng. Chem. Res. 51 (2012) 11499–11508.

[243] X. Lin, H. Kita, K. Okamoto, Silicalite Membrane Preparation, Characterization, and Separation Performance, Ind. Eng. Chem. Res. 40 (2001) 4069–4078. doi:10.1021/ie0101947.

[244] H. Matsuda, H. Yanagishita, H. Negishi, D. Kitamoto, T. Ikegami, K. Haraya, T. Nakane, Y. Idemoto, N. Koura, T. Sano, Improvement of ethanol selectivity of silicalite membrane in pervaporation by silicone rubber coating, J. Memb. Sci. 210 (2002) 433–437.

[245] H. Chen, Y. Li, W. Yang, Preparation of silicalite-1 membrane by solution-filling method and its alcohol extraction properties, J. Memb. Sci. 296 (2007) 122–130. doi:10.1016/j.memsci.2007.03.021.

[246] J. Kuhn, S. Sutanto, J. Gascon, J. Gross, F. Kapteijn, Performance and stability of multi-channel MFI zeolite membranes detemplated by calcination and ozonication in ethanol / water pervaporation, J. Memb. Sci. 339 (2009) 261–274. doi:10.1016/j.memsci.2009.05.006.

[247] B. Soydaş, Ö. Dede, A. Çulfaz, H. Kalipçilar, Separation of gas and organic/water mixtures by MFI type zeolite membranes synthesized in a flow system, Microporous Mesoporous Mater. 127 (2010) 96–103. doi:10.1016/j.micromeso.2009.07.004.

[248] D.J.O. Brien, L.H. Roth, A.J. Mcaloon, Ethanol production by continuous fermentation – pervaporation : a preliminary economic analysis, J. Memb. Sci. 166 (2000) 105–111.

[249] N. Arifeen, R. Wang, I. Kookos, C. Webb, A. Koutinas, Process Design and Optimization of Novel Wheat-Based Continuous Bioethanol Production System., Biotechnol Prog. 23 (2007) 1394–1403. doi:10.1021/bp0701517.

[250] J.A. Quintero, M.I. Montoya, O.J. Sánchez, O.H. Giraldo, C.A. Cardona, Fuel ethanol production from sugarcane and corn: Comparative analysis for a Colombian case, Energy. 33 (2008) 385–399. doi:10.1016/j.energy.2007.10.001.

[251] F. Lipnizki, R.W. Field, P.-K. Ten, Pervaporation-based hybrid process: a review of process

design, applications and economics, J. Memb. Sci. 153 (1999) 183–210. doi:10.1016/S0376-7388(98)00253-1.

[252] E. Nagy, P. Mizsey, J.Å. Hancsók, S. Boldyryev, P. Varbanov, Analysis of energy saving by combination of distillation and pervaporation for biofuel production, Chem. Eng. Process. Process Intensif. 98 (2015) 86–94.

[253] Y. Huang, R.W. Baker, L.M. Vane, Low-Energy Distillation-Membrane Separation Process, Ind. Eng. Chem. Res. 49 (2010) 3760–3768.

[254] Y. Huang, J. Ly, D. Nguyen, R.W. Baker, Ethanol Dehydration Using Hydrophobic and Hydrophilic Polymer Membranes, Ind Eng Chem Res. 49 (2010) 12067–12073.

[255] H. Nguyen, R.F. DeJaco, N. Mittal, J.I. Siepmann, M. Tsapatsis, M.A. Snyder, W. Fan, B. Saha, D.G. Vlachos, A Review of Biorefinery Separations for Bioproduct Production via Thermocatalytic Processing, Annu. Rev. Chem. Biomol. Eng. 8 (2017) 115–137. doi:10.1146/annurev-chembioeng-060816-101303.

[256] D. Humbird, R. Davis, L. Tao, C. Kinchin, D. Hsu, A. Aden, Process Design and Economics for Biochemical Conversion of Lignocellulosic Biomass to Ethanol: Dilute-Acid Pretreatment and Enzymatic Hydrolysis of Corn Stover | Department of Energy, 2011. https://energy.gov/eere/bioenergy/downloads/process-design-and-economics-biochemical-conversion-lignocellulosic-biomass (accessed February 25, 2018).

[257] R. Power, Steam jet ejectors for the process industries, 1994.

[258] K. Sato, K. Sugimoto, T. Nakane, Preparation of higher flux NaA zeolite membrane on asymmetric porous support and permeation behavior at higher temperatures up to 145 °C in vapor permeation, J. Memb. Sci. 307 (2008) 181–195. doi:10.1016/j.memsci.2007.09.017.

[259] X. Shu, X. Wang, Q. Kong, X. Gu, N. Xu, High-Flux MFI Zeolite Membrane Supported on YSZ Hollow Fiber for Separation of Ethanol / Water, Ind. Eng. Chem. Res. (2012).

[260] S. Xia, Y. Peng, Z. Wang, Microstructure manipulation of MFI-type zeolite membranes on hollow fi bers for ethanol – water separation, J. Memb. Sci. 498 (2016) 324–335. doi:10.1016/j.memsci.2015.10.024.

[261] H. Zhang, Q. Xiao, X. Guo, N. Li, P. Kumar, N. Rangnekar, M.Y. Jeon, S. Al-Thabaiti, K. Narasimharao, S.N. Basahel, B. Topuz, F.J. Onorato, C.W. Macosko, K.A. Mkhoyan, M. Tsapatsis, Open-Pore Two-Dimensional MFI Zeolite Nanosheets for the Fabrication of Hydrocarbon-Isomer-Selective Membranes on Porous Polymer Supports, Angew. Chemie - Int. Ed. 55 (2016) 7184–7187. doi:10.1002/anie.201601135.

[262] D.S. Sholl, R.P. Lively, Seven chemical separations to change the world, Nature. 532 (2016) 435–437. doi:10.1038/532435a.

[263] M. Eramo, Changing fundamentals and shattered paradigms, in: 32nd World Petrochemical Conf., IHS Markit, 2017. http://cdn.ihs.com/www/Events/WPC2017/Presentations/IHSM-Eramo-Touroftheworldglobal-March21.pdf (accessed January 19, 2018).

[264] M.S. Peters, K.D. Timmerhaus, R.E. (Ronald E. West, Plant design and economics for chemical engineers., McGraw-Hill, 2003. https://www.amazon.com/Plant-Design-Economics-Chemical-Engineers/dp/0072392665 (accessed January 19, 2018).

[265] J.A. Caballero, I.E. Grossmann, M. Keyvani, E.S. Lenz, N. Square, V. Pennsyl, Design of Hybrid Distillation - Vapor Membrane Separation Systems, Ind. Eng. Chem. Res. 48 (2009) 9151–9162. doi:10.1021/ie900499y.

[266] V. Gokhale, S. Hurowitz, J.B. Riggs, A Comparison of Advanced Distillation Control

Techniques for a Propylene/Propane Splitter, Ind. Eng. Chem. Res. 34 (1995) 4413–4419. doi:10.1021/ie00039a033.

[267] M. Azhin, T. Kaghazchi, M. Rahmani, A review on olefin/paraffin separation using reversible chemical complexation technology, J. Ind. Eng. Chem. 14 (2008) 622–638. doi:10.1016/J.JIEC.2008.04.014.

[268] R.B. Eldridge, Olefin/Paraffin Separation Technology: A Review, Ind. Eng. Chem. Res. 32 (1993) 2208–2212. doi:10.1021/ie00022a002.

[269] D.J. Safarik, R.B. Eldridge, Olefin/Paraffin Separations by Reactive Absorption: A Review, Ind. Eng. Chem. Res. 37 (1998) 2571–2581. doi:10.1021/ie970897h.

[270] C.A. Grande, A.E. Rodrigues, Propane/propylene separation by Pressure Swing Adsorption using zeolite 4A, Ind. Eng. Chem. Res. 44 (2005) 8815–8829. doi:10.1021/ie050671b.

[271] S.U. Rege, J. Padin, R.T. Yang, Olefin/Paraffin Separations by Adsorption: π-Complexation vs. Kinetic Separation, AIChE J. 44 (1998) 799–809. doi:10.1002/aic.690440405.

[272] M. Galizia, W.S. Chi, Z.P. Smith, T.C. Merkel, R.W. Baker, B.D. Freeman, 50th Anniversary Perspective: Polymers and Mixed Matrix Membranes for Gas and Vapor Separation: A Review and Prospective Opportunities, Macromolecules. 50 (2017) 7809–7843. doi:10.1021/acs.macromol.7b01718.

[273] A. Motelica, O.S.L. Bruinsma, R. Kreiter, M. Den Exter, J.F. Vente, Membrane retrofit option for paraffin/olefin separation-a technoeconomic evaluation, Ind. Eng. Chem. Res. 51 (2012) 6977–6986. doi:10.1021/ie300587u.

[274] I.K. Kookos, Optimal Design of Membrane/Distillation Column Hybrid Processes, Ind. Eng. Chem. Res. 42 (2003) 1731–1738. doi:10.1021/ie020616s.

[275] Y. Naidu, R.K. Malik, A generalized methodology for optimal configurations of hybrid distillation-pervaporation processes, Chem. Eng. Res. Des. 89 (2011) 1348–1361. doi:10.1016/j.cherd.2011.02.025.

[276] J. Park, K. Kim, J.W. Shin, K. Tak, Y.K. Park, Performance Study of multistage membrane and hybrid distillation processes for propylene/propane separation, Can. J. Chem. Eng. 95 (2017) 2390–2397. doi:10.1002/cjce.22914.

[277] H.-J. Salgado-Gordon, G. Valbuena-Moreno, Technical and economic evaluation of the separation of light olefins (ethylene and propylene) by using π-complexation with silver salts, Ciencia, Tecnol. Y Futur. 4 (2011) 73–88.

[278] J.R. Alcántara-Avila, F.I. Gómez-Castro, J.G. Segovia-Hernández, K.I. Sotowa, T. Horikawa, Optimal design of cryogenic distillation columns with side heat pumps for the propylene/propane separation, Chem. Eng. Process. Process Intensif. 82 (2014) 112–122. doi:10.1016/j.cep.2014.06.006.

[279] A.A. Shenvi, D.M. Herron, R. Agrawal, Energy efficiency limitations of the conventional heat integrated distillation column (HIDiC) configuration for binary distillation, Ind. Eng. Chem. Res. 50 (2011) 119–130. doi:10.1021/ie101698f.

[280] R.W. Baker, A.R. Da Costa, R. Daniels, I. Pinnau, Z. He, Membrane-augmented polypropylene manufacturing, US 6,271,319 B1, 2000. https://www.google.com/patents/US6271319 (accessed January 20, 2018).

[281] NIST, Propane - phase change data,. http://webbook.nist.gov/cgi/cbook.cgi?ID=C74986&Mask=4#Thermo-Phase.

[282] NIST, Propene - phase change data,. http://webbook.nist.gov/cgi/cbook.cgi?ID=C115071&Mask=4#Thermo-Phase.

[283] A.A. Kiss, S.J. Flores Landaeta, C.A.I. Ferreira, Towards energy efficient distillation technologies e Making the right choice, Energy. 47 (2012) 531–542. doi:10.1016/j.energy.2012.09.038.

[284] T.M. Zygula, K. Kolmetz, Design Considerations for Propylene Splitters, in: AIChE Spring Meet. Glob. Congr. Process Saf., Chicago, 2011: p. 96f. https://www.aiche.org/conferences/aiche-spring-meeting-and-global-congress-on-process-safety/2011/proceeding/paper/96f-design-considerations-propylene-splitters-0 (accessed January 19, 2018).

[285] D.F. Schneider, Heat integration complicates heat pump troubleshooting, Strat. Eng. Inc. (2001) 1–13.

[286] R.L. Burns, W.J. Koros, Defining the challenges for C3H6/C3H8 separation using polymeric membranes, J. Memb. Sci. 211 (2003) 299–309. doi:10.1016/S0376-7388(02)00430-1.

[287] M. Rungta, C. Zhang, J.W. Koros, L. Xu, Membrane-Based Ethylene/Ethane Separation: The Upper Bound and Beyond, AIChE J. 59 (2013) 3475–3489.

[288] R. Faiz, K. Li, Polymeric membranes for light olefin/paraffin separation, Desalination. 287 (2012) 82–97. doi:10.1016/j.desal.2011.11.019.

[289] R. Faiz, K. Li, Olefin/paraffin separation using membrane based facilitated transport/chemical absorption techniques, Chem. Eng. Sci. 73 (2012) 261–284. doi:10.1016/j.ces.2012.01.037.

[290] X. Ma, Y.S. Lin, X. Wei, J. Kniep, Ultrathin carbon molecular sieve membrane for propylene/propane separation, AIChE J. 62 (2016) 491–499. doi:10.1002/aic.15005.

[291] L. Xu, M. Rungta, M.K. Brayden, M. V. Martinez, B.A. Stears, G.A. Barbay, W.J. Koros, Olefins-selective asymmetric carbon molecular sieve hollow fiber membranes for hybrid membrane-distillation processes for olefin/paraffin separations, J. Memb. Sci. 423–424 (2012) 314–323. doi:10.1016/j.memsci.2012.08.028.

[292] X. Ma, P. Kumar, N. Mittal, A. Khlyustova, P. Daoutidis, K.A. Mkhoyan, M. Tsapatsis, Zeolitic imidazolate framework membranes made by ligand-induced permselectivation, Submitted Manuscript.

[293] R. Surya Murali, K. Yamuna Rani, T. Sankarshana, A.F. Ismail, S. Sridhar, Separation of Binary Mixtures of Propylene and Propane by Facilitated Transport through Silver Incorporated Poly(Ether-Block-Amide) Membranes, Oil Gas Sci. Technol. – Rev. d'IFP Energies Nouv. 70 (2015) 381–390. doi:10.2516/ogst/2013190.

[294] S. Bai, S. Sridhar, A.A. Khan, Recovery of propylene from refinery off-gas using metal incorporated ethylcellulose membranes, J. Memb. Sci. 174 (2000) 67–79. doi:10.1016/S0376-7388(00)00376-8.

[295] S. Sunderrajan, B.D. Freeman, C.K. Hall, I. Pinnau, Propane and propylene sorption in solid polymer electrolytes based on poly (ethylene oxide) and silver salts, J. Memb. Sci. 182 (2001) 1–12.

[296] I. Pinnau, L.G. Toy, Solid polymer electrolyte composite membranes for olefin / paraffin separation, J. Memb. Sci. 184 (2001) 39–48.

[297] Y.S. Park, J. Won, Y.S. Kang, Facilitated transport of olefin through solid PAAm and

PAAm-graft composite membranes with silver ions, J. Memb. Sci. 183 (2001) 163–170. doi:10.1016/S0376-7388(00)00589-5.

[298] J.H. Kim, B.R. Min, J. Won, S.H. Joo, H.S. Kim, Y.S. Kang, Role of polymer matrix in polymer/silver complexes for structure, interactions, and facilitated olefin transport, Macromolecules. 36 (2003) 6183–6188. doi:10.1021/ma034314t.

[299] J.H. Kim, J. Won, Y.S. Kang, Olefin-induced dissolution of silver salts physically dispersed in inert polymers and their application to olefin/paraffin separation, J. Memb. Sci. 241 (2004) 403–407. doi:10.1016/j.memsci.2004.05.027.

[300] J.H. Kim, B.R. Min, Y.W. Kim, S.W. Kang, J. Won, Y.S. Kang, Novel composite membranes comprising silver salts physically dispersed in poly(ethylene-co-propylene) for the separation of propylene/propane, Macromol. Res. 15 (2007) 343–347.

[301] T.C. Merkel, R. Blanc, I. Ciobanu, B. Firat, A. Suwarlim, J. Zeid, Silver salt facilitated transport membranes for olefin/paraffin separations: Carrier instability and a novel regeneration method, J. Memb. Sci. 447 (2013) 177–189. doi:10.1016/j.memsci.2013.07.010.

[302] M. Rungta, L. Xu, W.J. Koros, Carbon molecular sieve dense film membranes derived from Matrimid for ethylene/ethane separation, Carbon N. Y. 50 (2012) 1488–1502. doi:10.1016/j.carbon.2011.11.019.

[303] L. Xu, M. Rungta, W.J. Koros, Matrimid derived carbon molecular sieve hollow fiber membranes for ethylene/ethane separation, J. Memb. Sci. 380 (2011) 138–147. doi:10.1016/j.memsci.2011.06.037.

[304] R.J. Swaidan, X. Ma, I. Pinnau, Spirobisindane-based polyimide as efficient precursor of thermally-rearranged and carbon molecular sieve membranes for enhanced propylene/propane separation, J. Memb. Sci. 520 (2016) 983–989. doi:10.1016/j.memsci.2016.08.057.

[305] J. Liu, Y. Liu, D. Kayrak Talay, E. Calverley, M. Brayden, M. Martinez, A new carbon molecular sieve for propylene/propane separations, Carbon N. Y. 85 (2015) 201–211. doi:10.1016/j.carbon.2014.12.089.

[306] ICIS, Americas Chemicals Outlook 2017.

[307] W.J. Koros, R.P. Lively, Water and Beyond: Expanding the Spectrum of Large-Scale Energy Efficient Separation Processes, AIChE J. 58 (2012) 2624–2633. doi:10.1002/aic.

[308] M.T. Castoldi, J.C. Pinto, P.A. Melo, Modeling of the separation of propene/propane mixtures by permeation through membranes in a polymerization system, Ind. Eng. Chem. Res. 46 (2007) 1259–1269. doi:10.1021/ie060333q.

[309] Global Polypropylene (PP) Market Report 2017: $100+ Billion Market Size, Demand Forecasts, Industry Trends and Updates 2017-2021, 2017.

[310] D. Kim, S. Lee, C. Engineering, C. Techno, Numerical simulation of fixed-bed catalytic reactor for isopropyl alcohol synthesis, Korean J. Chem. Eng. 6 (1989) 99–104.

[311] Y. Xu, K.T. Chuang, A.R. Sanger, Design of a Process for production of isopropyl alcohol by hydration of propylene in a catalytic distillation column, Chem. Eng. Res. Des. 80 (2002) 686–694. doi:10.1205/026387602760312908.

[312] A. Shamiri, M.A. Hussain, F.S. Mjalli, M.S. Shafeeyan, N. Mostoufi, Experimental and Modeling Analysis of Propylene Polymerization in a Pilot-Scale Fluidized Bed Reactor, Ind. Eng. Chem. Res. 53 (2014) 8694–8705. doi:10.1021/ie501155h.